IMPACT OF CASCADIA SUBDUCTION ZONE EARTHQUAKE ON THE EVALUATION CRITERIA OF BRIDGES

TECHNICAL REPORT

SPR 770

Oregon Department of Transportation

IMPACT OF CASCADIA SUBDUCTION ZONE EARTHQUAKE ON THE EVALUATION CRITERIA OF BRIDGES

Technical Report

SPR 770

by
Peter Dusicka
Associate Professor

Alvaro Lopez
Graduate Research Assistant

Portland State University

for

Oregon Department of Transportation
Research Section
555 13th Street NE, Suite 1
Salem OR 97301

and

Federal Highway Administration
400 Seventh Street, SW
Washington, DC 20590-0003

December 2016

Technical Report Documentation Page

1. Report No.

FHWA-OR-RD-17-04

2. Government Accession No.

3. Recipient's Catalog No.

4. Title and Subtitle

Impact of Cascadia Subduction Zone Earthquake on the Seismic Evaluation Criteria of Bridges

5. Report Date

-December 2016-

6. Performing Organization Code

7. Author(s)

Peter Dusicka, PhD, PC, Associate Professor and Alvaro Lopez, Graduate Research Assistant

8. Performing Organization Report No.

9. Performing Organization Name and Address

Department of Civil and Environmental Engineering
Portland State University
1930 SW 4th Avenue, Suite 200
Portland, OR 97201

10. Work Unit No. (TRAIS)

11. Contract or Grant No.

12. Sponsoring Agency Name and Address

Oregon Dept. of Transportation
Research Section
555 13th Street NE, Suite 1
Salem, OR 97301

and

Federal Highway Admin.
400 Seventh Street, SW
Washington, DC 20590-0003

13. Type of Report and Period Covered

Technical Report

14. Sponsoring Agency Code

15. Supplementary Notes

16. Abstract: A large magnitude long duration subduction earthquake is impending in the Pacific Northwest, which lies near the Cascadia Subduction Zone (CSZ). Great subduction zone earthquakes are the largest earthquakes in the world and are the sole source zones that can produce earthquakes greater than M8.5. For this reason, structures such as reinforced concrete bridges are facing high seismic hazards and risk. The seismic risk used for the bridge design and retrofit is defined by hazard maps of ground acceleration values. The maps combine multiple regional sources of ground shaking using a Probabilistic Seismic Hazard Analysis (PSHA). Each source has a different intensity, probability of occurrence, and distance to a specific location. One key source of ground shaking in PSHA in Oregon is from the Cascadia Subduction Zone; however, a CSZ has several potential scenarios (M8.3 and M9.0) that can have significantly different ground motion estimates as a standalone event than what is captured in the values derived from PSHA. In this study, a computer model called CSZ14 was developed to obtain the acceleration values expected from a full rupture CSZ event. These values were also compared to previous CSZ models as well as to uniform hazard of various return periods from USGS hazard adopted in 2002, which continues to be used for the current design of bridges. Also, the increased duration of a CSZ earthquake may result in more structural damage than expected. Recent long duration subduction earthquakes occurred in Maule, Chile (M_w 8.8, 2010) and Tohoku, Japan (M_w 9.0, 2011) are a reminder of the importance of the effect ground motion duration on structural performance. As part of the research on the potential impacts, the dynamic performance of circular reinforced concrete bridge columns was experimentally evaluated using shake table tests by comparing the column response from crustal and subduction ground motions. Three continuous reinforced columns and three laps-spliced columns were tested using records from 1989 Loma Prieta, 2010 Maule and 2011 Tohoku. The results demonstrated that duration of the motion can affect the imposed damage and the displacement capacity of the bridge column.

17. Key Words

Subduction zone earthquakes, seismic hazard analysis, reinforced concrete bridge columns, shake table test, Performance-based seismic design.

18. Distribution Statement

Copies available from NTIS, and online at http://www.oregon.gov/ODOT/TD/TP_RES/

19. Security Classification (of this report)

Unclassified

20. Security Classification (of this page)

Unclassified

21. No. of Pages

163

22. Price

Technical Report Form DOT F 1700.7 (8-72) Reproduction of completed page authorized Printed on recycled paper

SI* (MODERN METRIC) CONVERSION FACTORS

APPROXIMATE CONVERSIONS TO SI UNITS					**APPROXIMATE CONVERSIONS FROM SI UNITS**				
Symbol	When You Know	Multiply By	To Find	Symbol	Symbol	When You Know	Multiply By	To Find	Symbol
		LENGTH					**LENGTH**		
in	inches	25.4	millimeters	mm	mm	millimeters	0.039	inches	in
ft	feet	0.305	meters	m	m	meters	3.28	feet	ft
yd	yards	0.914	meters	m	m	meters	1.09	yards	yd
mi	miles	1.61	kilometers	km	km	kilometers	0.621	miles	mi
		AREA					**AREA**		
in^2	square inches	645.2	millimeters squared	mm^2	mm^2	millimeters squared	0.0016	square inches	in^2
ft^2	square feet	0.093	meters squared	m^2	m^2	meters squared	10.764	square feet	ft^2
yd^2	square yards	0.836	meters squared	m^2	m^2	meters squared	1.196	square yards	yd^2
ac	acres	0.405	hectares	ha	ha	hectares	2.47	acres	ac
mi^2	square miles	2.59	kilometers squared	km^2	km^2	kilometers squared	0.386	square miles	mi^2
		VOLUME					**VOLUME**		
fl oz	fluid ounces	29.57	milliliters	ml	ml	milliliters	0.034	fluid ounces	fl oz
gal	gallons	3.785	liters	L	L	liters	0.264	gallons	gal
ft^3	cubic feet	0.028	meters cubed	m^3	m^3	meters cubed	35.315	cubic feet	ft^3
yd^3	cubic yards	0.765	meters cubed	m^3	m^3	meters cubed	1.308	cubic yards	yd^3
NOTE: Volumes greater than 1000 L shall be shown in m^3.									
		MASS					**MASS**		
oz	ounces	28.35	grams	g	g	grams	0.035	ounces	oz
lb	pounds	0.454	kilograms	kg	kg	kilograms	2.205	pounds	lb
T	short tons (2000 lb)	0.907	megagrams	Mg	Mg	megagrams	1.102	short tons (2000 lb)	T
		TEMPERATURE (exact)					**TEMPERATURE (exact)**		
°F	Fahrenheit	(F-32)/1.8	Celsius	°C	°C	Celsius	1.8C+32	Fahrenheit	°F

*SI is the symbol for the International System of Measurement

ACKNOWLEDGEMENTS

The author would like to thank the members of ODOT's Technical Advisory Committee as well as the Research Section for their advice and assistance during the project and preparation of this report. The authors would also like to thank the undergraduate research assistants Benjamin Herdrich and Zakary Hoyt who contributed their time and effort to significantly contribute and help complete this research.

DISCLAIMER

TABLE OF CONTENTS

LIST OF TABLES

LIST OF FIGURES

1.0 INTRODUCTION

1.1 GENERAL

The Cascadia Subduction Zone (CSZ) ‘megathrust” fault is a convergent plate boundary extending over ~ 1000 km from the northern California to southwestern British Columbia. Great subduction zone earthquakes are the largest earthquakes in the world and are the sole source zones that can produce earthquakes greater than M8.5. For this reason and the high likelihood of occurrence of a strong earthquake in the future, structures in the Pacific Northwest are facing high seismic hazards and risk. An example of these structures are reinforced concrete bridges, which are vital components of transportation system, and that have exposed their vulnerabilities to moderate and large ground excitations. The seismic risk used for the bridge design and retrofit is defined by hazard maps of ground acceleration values. The maps combine multiple regional sources of ground shaking using a Probabilistic Seismic Hazard Analysis (PSHA). Each source has a different intensity, probability of occurrence, and distance to a specific location. One key source of ground shaking in PSHA in Oregon is from the Cascadia Subduction Zone; however, a CSZ has several potential scenarios (M8.3 and M9.0) that can have significantly different ground motion estimates as a standalone event than what is captured in the values derived from PSHA.

For seismic evaluation of bridges in Oregon, two cases are considered: ‘no collapse’ for large earthquake shaking and ‘serviceability’ for more frequent smaller earthquake shaking. ‘No collapse’ is expected to result in severe damage without complete collapse; ‘serviceability’ requires little or no damage so the bridge remains functional. The ground acceleration used in design for the ‘no collapse’ and ‘serviceability’ cases at a specific location would have two different values derived from PSHA hazard maps.

For ‘no collapse’, the CSZ earthquake dominates calculated PSHA acceleration values along the coast, but has a diminishing contribution further inland. Consequently, actual ground acceleration inland from a CSZ event may exceed the PSHA values, which means designers, following current seismic design code, may be under-designing for collapse prevention in certain parts of the state. For ‘serviceability’, the less frequent CSZ would have little contribution when considering low level earthquakes. For this reason, ODOT adopted higher hazard than recommended in the FHWA Seismic Retrofit Manual *(FHWA 2006)*(FHWA 2006)*(FHWA 2006)* in an effort to recognize a more reasonable CSZ influence for serviceability. Doing this also raised the contributions from other earthquake sources across the state within the PSHA calculation. Consequently, designers following the current ODOT guidelines for serviceability could be over-designing to meet ‘serviceability’ performance.

For cases where acceleration values from a singular CSZ event are similar to those derived from the PSHA maps, the increased duration of a CSZ earthquake may result in more damage than expected. Recent long duration ground motions occurred in Maule, Chile (Mw8.8, 2010) and Tohoku, Japan (Mw 9.0, 2011) are a reminder of the importance of the effect ground motion duration on structural performance. Particularly, reinforced concrete columns are often the most susceptible component to damage. Numerical simulations using data from these recent subduction earthquakes have shown that more damage occurs from the increased duration of shaking as compared to non-subduction earthquakes of the same peak acceleration. However, this result needs to be experimentally verified given the possibility of the occurrence of another megathrust earthquake in the Cascadia subduction zone.

1.2 OBJECTIVE AND SCOPE

The goal of this project is to provide a rational estimate of ground acceleration values for designing new and retrofitting existing bridges. The two main objectives of the research effort were to:

- evaluate the hazard by contrasting the acceleration values from individual CSZ events to PSHA values
- provide experimental evidence of damage difference under longer duration shaking expected from CSZ event

A computer model for calculating PGA and spectral acceleration values for 0.2 sec and 1.0 sec was developed for a full rupture CSZ event. The outcomes of this model were compared to previous CSZ models as well as to uniform hazard of various return periods from 2002, including Serviceability and Life Safety recurrence rates.

The experimental study consisted of six typical circular RC bridge columns; the columns were detailed to represent conditions that occurred in old bridge construction in Oregon. The columns were tested under shaking loading using crustal and subduction zone earthquakes.

Finally, preliminary results of limit stated for the performance-based seismic design were presented. The investigation focused on defining and quantifying structural performance and corresponding limit stated. The two performance levels required by ODOT were studied, such as Operational and Life Safety. Results from previous and current experiments were used to assess each limit state in terms of strains observed during experiments.

1.3 REPORT CONTENTS

Chapter 2 and Chapter 3 outline different approaches to calculating acceleration values that are expected to result from a megathrust earthquake originating on the Cascadia subduction Zone (CSZ). The initial estimation of the accelerations were made using a de-aggregation process of the hazard from USGS 2002 and 2008 and ultimately lead to calculating the accelerations based on USGS 2014 approach based on a full-rupture model. Chapter 4.0 summarizes the experimental program of typical scaled circular reinforced concrete bridge columns subjected to shake table loading. Additionally, test results and their analyses were also presented. Chapter 5.0 presents an assessment of the limit states for the performance-based seismic design adopted by the dual design criteria based on strains.

2.0 SEISMIC ACCELERATION VALUES FOR CSZ BY DEAGGREGATION OF USGS 2002 AND 2008 HAZARD

2.1 GENERAL

This chapter describe the comparisons made between the acceleration values that ODOT uses for bridge design, which follow the USGS's 2002 Uniform Hazard Maps, to the acceleration values that are expected to result from a megathrust earthquake originating on the Cascadia Subduction Zone (CSZ). The Cascadia Subduction Zone accelerations were obtained using different methods, from initially de-aggregating the hazard to ultimately implementing a methodology for representing full rupture earthquake.

For the initial de-aggragation effort, the following comparisons were made:

I) 2002 Deaggregated Deterministic Seismic Hazard Analysis (D-DSHA) versus 2002 Uniform Hazard Spectra (UHS)

II) 2002 Deaggregated Deterministic Seismic Hazard Analysis (D-DSHA) versus 2002 USGS Scenario Deterministic Seismic Hazard Analysis (S-DSHA)

III) 2002 USGS Scenario Deterministic Seismic Hazard Analysis (S-DSHA) versus 2008 USGS Scenario Deterministic Seismic Hazard Analysis (S-DSHA'08)

For each comparison, a graphical representation of the ratio is made between the ground motion expected from the Cascadia Subduction Zone earthquake and the uniform seismic hazard maps for Western Oregon. This process is performed for the return periods of 108, 475, 975, and 2475 years, and the spectral accelerations of PGA, 0.2 seconds, and 1.0 seconds.

When comparing the Deaggregated Deterministic Seismic Hazard Analysis to Uniform Hazard Spectra design values, the Cascadia subduction zone values exceed Uniform hazard spectral acceleration in different areas of the state, the extent of which depends on the return period of Uniform hazard spectrum. The largest area being for the 475 return period used for serviceability, but also is significant for the 1000 year return period for no-collapse. In general, the Deaggregated deterministic seismic hazard analysis were higher than the Scenario deterministic seismic hazard analysis using the 2002 as well as 2008 attenuation.

2.2 THE UNIFORM SEISMIC HAZARD MAPS

The uniform seismic hazard maps were generated by the United States Geological Survey, and form the basis for the seismic design and analysis of most modern structures. These maps depict the ground motion, in the form of spectral acceleration, which is predicted to occur at locations throughout the United States as a function of a certain return period. These intervals typically consist of 475 and 2475 year return periods, which correspond to probabilities of exceedance of 10% and 2% in 50 years, respectively. Further, these maps are also generated for various spectral accelerations, which represent the pseudo-acceleration experienced by a structure as a function of that structure's natural period. The peak ground acceleration (PGA) and spectral accelerations (SA) of 0.2 seconds and 1.0 seconds are frequently of interest to structural engineers as they are used to construct the design spectra.

The first manifestation of the uniform hazard maps in Oregon were as a result of a 1995 report for the Oregon Department of Transportation (ODOT), prepared by Geomatrix Consultants *(Dickenson 2005).* The maps have since undergone periodic updates in 1996, 2002, 2008, and 2014, with each successive update incorporating new knowledge regarding the seismic sources and attenuations.

2.3 BRIEF COMPARISON BETWEEN THE 2002 AND 2008 UNIFORM HAZARD MAPS

The most recent design codes, such as *(ASCE/SEI 2010)* for buildings, are based on the 2008 edition of the uniform hazard maps. However, ODOT continues to base the design of new structures on the Pacific Northwest region of the 2002 USGS National Seismic Hazard maps *(ODOT 2013).* There are a number of differences between the 2002 and 2008 Uniform Seismic Hazard Maps. In the Pacific Northwest, these changes include the addition of a new recurrence distribution for the Cascadia Subduction Zone, which accounted for a wider range of magnitudes, the consideration of deep earthquakes in the Portland area and along the coast, and changes in the attenuation equations *(Petersen et al. 2008).*

As a result, there are variations in the ground motion values depicted in the Pacific Northwest between the different editions of the hazard maps. These variations can be visualized with the aid of maps published on the USGS website, as depicted in Figure 2.1, which illustrate the ratio of the ground accelerations for 2475 return period. In general, for the shorter spectral accelerations, as shown on the map, the ground acceleration values were typically within about 10% of each other. For longer spectral accelerations however, the ground acceleration values in the 2008 Uniform Hazard Maps are up to 30% lower when compared to the 2002 maps. The exception to this trend is along the western coast, where the ground acceleration values are slightly higher due to the new attenuation equations.

2.4 PROBABILISTIC AND DETERMINISTIC SEISMIC HAZARD ANALYSIS

The uniform hazard maps were generated following a procedure known as probabilistic seismic hazard analysis (PSHA). This method involves incorporating various uncertainties about the source of ground acceleration, such as the magnitude of the earthquake, the recurrence relationship, the distance from the site to the source, and the accuracy of the attenuation equations used. Additionally, this allows the USGS to depict the seismic hazard at a point due to the contributions of multiple seismic sources, such as surface faults, deep intraplate earthquakes, and interplate subduction-type events.

Some of the data that is used to create the uniform hazard maps is available to the public and scientific community through the Interactive Deaggregation Application on the USGS website. When using this application, one can enter the latitude or longitude of a location, the return period, period, and site shear wave velocity of interest. A text file is then produced from the application, which depicts the distance, magnitude, and relative contribution of all of the seismic hazards at that site.

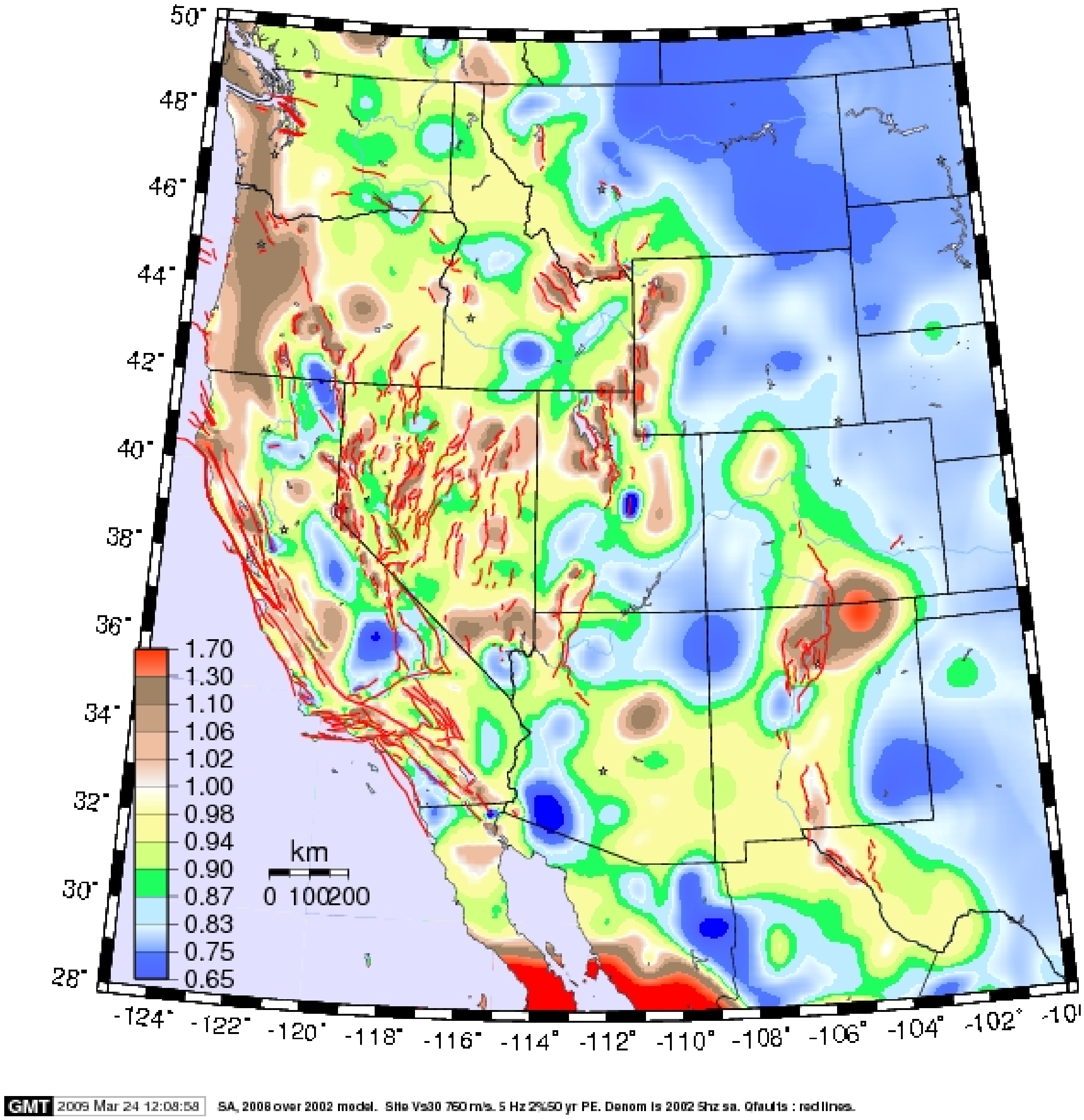

Figure 2.1: Map of ground accelerations from the 2008 Uniform Seismic Hazard Maps divided by those from the 2002 maps, for a 0.2 second SA and a 2475 year return period. Figure from USGS Earthquake Hazards website

However, it is not possible to use this data to determine the ground acceleration values of a Cascadia event through the use of PHSA. This is because the Interactive Deaggregation website does not provide the recurrence rate, rupture zone geometry, and weighting data used to create the hazard maps. Further, the calculations used to determine the ground motion are complex, due to numerous models, attenuation equations, and methods of depicting the rupture *(A. Frankel 2014)*.

Instead, the deaggregation method was used along with deterministic analysis to obtain the seismic hazard due to CSZ. Using the magnitude and distance values determined from the Interactive Deaggregation application, various attenuation equations were used to determine the ground acceleration values that would result. This method is simpler than PSHA, because it does not incorporate the various uncertainties associated with the ground motion. Rather, it calculates the median ground acceleration that results from a seismic event of known distance and magnitude.

2.5 ATTENUATION EQUATIONS

In order to perform a meaningful comparison with the USGS Uniform Hazard Maps, it is important to use the same attenuation equations that were used in the creation of the maps *(Dickenson 2005)*. Accordingly, in order to calculate the ground acceleration that is expected to result from a CSZ earthquake, two attenuation equations were used, as noted in Table 2.1. These two attenuation equations were used in the calculation of the 2002 Uniform Hazard Maps *(Frankel et al. 2002)*.

Further, a weighting system was adopted which was identical to the weighting system used by USGS, as depicted in Table 2.2. The weight that was applied to each attenuation equation is a function of the magnitude of the earthquake (i.e. M8.3 or M9.0) and the source-to-site distance. For the magnitude 8.3 earthquakes, equal weight was applied to both the Youngs and Sadigh attenuation equations for distances greater than 55 kilometers. For distances greater than 85 kilometers, 100% weight was applied to the Youngs attenuation equation. In the 2002 documentation of the seismic hazard maps, it is stated that the USGS applied "the change in weighting with a 30 km wide taper centered on [70 km]" *(Frankel et. al. 2002)*. This was interpreted by the authors as a gradual transition between the two weighting schemes, and accordingly, a linear interpolation was performed between the distances of 55 and 85 kilometers.

Likewise, a similar system was applied for the M9.0 earthquakes, with equal weight being applied to the two attenuation equations for distances less than 45 kilometers, and full weight being applied to Youngs for distances greater than 75 kilometers. As in the M8.3 events, linear interpolation was used to taper the transition between the two weighting systems.

Table 2.1:Attenuation equations used to calculate ground motion from Cascadia Subduction Zone earthquakes *(Frankel et. al. 2002)*:

Attenuation Equations	Weight	Damping
Youngs et al. 1997	Varies as a function of distance from source	5%
Sadigh et al. 1997[1]		5%

[1] For magnitude greater than M8.5, a magnitude value of 8.5 is used in the equation.

Table 2.2: Weighting system used by USGS for CSZ earthquakes, as a function of magnitude and distance:

Magnitude	Distance (km)	Weight applied to equation	
		Younghs et al. 1997	Sadigh et al. 1997
8.3	R ≤ 55	50%	50%
	55 < R < 85	Linearly interpolated	
	R ≥ 85	100%	0%
9.0	R ≤ 45	50%	50%
	45 < R < 75	Linearly interpolated	
	R ≥ 75	100%	0%

The attenuation equation by Youngs has been derived in order to predict the peak ground motion acceleration for subduction zone interface and intraslab earthquakes of magnitudes greater than M5+, and for source-to-site distances from 10 to 500 kilometers *(Youngs et al. 1997)*. As depicted in the following equation, Youngs related the horizontal acceleration as a function of the moment magnitude, the source-to-site distance, the depth of the hypocenter, the source type, and a number of constants. These constants, in turn, are functions of the spectral acceleration of interest.

When this attenuation equation was used in this study, a number of assumptions were made, which are worth noting. First and foremost, this equation is valid for two types of faults; shallow interface and deep intraslab. When this equation was used for this study, the shallow interface source was assumed, and accordingly, the "Z_T" term of the equation was set to zero. The intraslab source type is used for earthquakes with a focal depth greater than 35 kilometers, which are not of interest in this study. Further, it was also assumed that for the "H" term of the equation, the depth of the hypocenter was 20 kilometers, in keeping with the assumptions and methodology utilized in the seismic hazard maps *(Frankel et al. 2002)*.

$$\ln(y) = 0.2418 + 1.414 \cdot M + C_1 + C_2 \cdot (10 - M)^3 + C_3 \cdot \ln\left(r_{rup} + 1.7818 \cdot e^{0.554 \cdot M}\right) + 0.00607 \cdot H + 0.3846 \cdot Z_T \qquad \textbf{(2.1)}$$

Where,

y = horizontal spectral acceleration in g
M = moment magnitude
r_{rup} = closest distance to rupture (km)
H = depth of hypocenter (km)
Z_T = source type, 0 for interface, 1 for intraslab

Additionally, the equation from *(Sadigh et al. 1997)* was also used, as depicted below. It was determined in the initial stages of this study that the attenuation equation listed in the original publication of Sadigh et al. may contain an error, and this incorrect equation is denoted as such below. The third term of this equation states that the magnitude of the earthquake should be multiplied by 8.5. This error results in the ground motion for the 0.2 and 1.0 second SA becoming equal to zero, although it does not affect the PGA values. An alternative version of this equation is denoted below, and this third term has been corrected to "8.5-M" *(Douglas 2001)*.

Additionally, this equation is limited to direct use for magnitudes of earthquakes of less than M8.5; this is because a magnitude greater than 8.5 would result in a negative value in the third term, which is then raised to the power of 2.5. This results in a non-real result. However, this equation is still used in the 2002 Seismic Hazard Maps, as it was believed that Youngs may under predict the ground motion that results from subduction zone earthquakes. Instead, for all magnitudes greater than 8.5, a moment magnitude of 8.5 is used in the equation, which eliminates the non-real result that would otherwise occur.

Lastly, the Sadigh et al. equation can be used to determine the ground acceleration that results from either strike-slip faults, or for reverse/thrust faults. For the purposes of this study, Sadigh was used for the reverse/thrust fault acceleration values, and accordingly, the equation was multiplied by 1.2, as recommended by the authors of the equation. However, the 2002 documentation does not explicitly state which source type is assumed to be associated with the CSZ. Nonetheless, it was noted in the documentation of the 1996 National Uniform Hazard Maps that Sadigh and others *(Sadigh et al. 1993)* was modified for crustal thrust earthquakes to calculate the acceleration from the CSZ event *(Frankel et al. 1996)*. As such, this was determined to be sufficient justification to use the equation for the reverse/thrust fault type, rather than the strike-slip.

Incorrect equation:

$$\ln(y) = C_1 + C_2 \cdot M + C_3 \cdot \left(8.5M\right)^{2.5} + C_4 \cdot \ln\left(r_{rup} + e^{C_5 + C_6 \cdot M}\right) + C_7 \cdot \ln\left(r_{rup} + 2\right) \qquad \mathbf{(2.2)}$$

Corrected equation (Douglas 2001):

$$\ln(y) = C_1 + C_2 \cdot M + C_3 \cdot \left(8.5 - M\right)^{2.5} + C_4 \cdot \ln\left(r_{rup} + e^{C_5 + C_6 \cdot M}\right) + C_7 \cdot \ln\left(r_{rup} + 2\right) \qquad \mathbf{(2.3)}$$

Where:

y = horizontal spectral acceleration in g
M = moment magnitude
r_{rup} = minimum distance to the rupture surface (km)
Equation is for strike-slip fault
Multiply strike-slip values by 1.2 to obtain reverse/thrust fault acceleration

Lastly, a number of other attenuation equations were used in the hazard maps to determine the ground motion that resulted from other types of faults. For the Western United States, these equations and their associated weights are included for completeness, although these faults are not of interest in this study. For the shallow crustal earthquakes, up to five attenuation equations were used with equal weight, as depicted in Table 2.3. Further, the calculation of ground motion from deep intraslab earthquakes (depth greater than 35 kilometers) was performed using three attenuation equations, with the respective weights denoted in Table 2.4.

Table 2.3: Attenuation equations used to calculate ground motion from shallow crustal plates outside of extensional area[1] for 2002 Uniform Hazard Maps:

Attenuation Equations	Weight
Abrahamson and Silva 1997	25%
Boore et. al. 1997	25%
Campbell and Bozorgnial 2003	25%
Sadigh et. al. 1997	25%

[1] The extensional area is approximately bounded on the western edge by the Willamette Valley. Within the extensional area, include Spudich et. al. 1999, and assign 20% weight to all attenuation equations.

Table 2.4: Attenuation equations used to calculate ground motion from deep intraslab earthquakes, defined as having a depth greater than 35 km:

Attenuation Equations	Weight
Younghs et. al. 1997, deep intraslab	50%
Atkinson and Boore 2002, global relation	25%
Atkinson and Boore 2002, Cascadia region relation	25%

2.6 2002 AND 2008 USGS SCENARIO DSHA USED IN PARTS II AND III

USGS ran a Deterministic seismic hazard analysis of a scenario M9.0 event on the Cascadia subduction zone, and provided the results to ODOT. These acceleration values are denoted by latitude and longitude, for PGA, 0.2 second, and 1.0 second spectral accelerations. The data was obtained by performing a Deterministic seismic hazard analysis of a scenario earthquake, which consisted of a full rupture M9.0 subduction zone earthquake on the Cascadia subduction zone. This analysis was performed using the 2002 attenuation equations, and again with the 2008 attenuation equations, and both sets of data were provided to ODOT by (Frankel 2013).

Both sets of raw data were then provided to the authors of this study by ODOT, and this data is utilized in two different ways. In Section 2.8.2, the values that were predicted by USGS with the 2002 attenuation equations were compared to the ground accelerations predicted by the authors of this study, who also used the 2002 equations. A series of maps were created, as in Section 2.8.1, to allow for the spatial comparison between accelerations for PGA, 0.2 second, and the 1.0 second spectral acceleration.

Further, Section 2.8.3 compares the two different sets of raw data provided to ODOT; the 2002 and 2008 attenuated data. Accordingly, for each of the grid points contained within this data, the value of the acceleration from the 2002 attenuation equations is divided by the data from the 2008 attenuation equations, to determine the ratio of the values. This ratio was used to generate maps for each of the spectral accelerations.

2.7 METHODOLOGY

2.7.1 2002 Deaggregated DSHA versus 2002 Uniform Hazard

2.7.1.1 Determine Return Periods and Spectral Accelerations of Interest

The first step in this process was determining the return periods and spectral accelerations that were of interest for this study. The return periods that were of particular interest were 475 years and 975 years, corresponding to probability of exceedance of 10% and 5% in 50 years, respectively. These values correspond to the "500-year Serviceability Criteria" and "1000-year No-Collapse Criteria" used by ODOT for the design of new bridges and approach structures *(ODOT 2013)*. Additionally, return periods of 108 years and 2475 years (50% in 75 years and 2% in 50 years) were also chosen to provide more insight into how the relative influence of the Cascadia subduction zone changes as a function of the return period.

Further, the spectral accelerations of interest were chosen as the peak ground acceleration, 0.2 second spectral acceleration, and 1.0 second spectral acceleration. These values were selected as they are the primary points used to construct the seismic design spectrum, corresponding to PGA, S_s and S_1, respectively. Accordingly, these values could be used to calculate any other spectral acceleration of interest once the design spectrum was created.

2.7.1.2 Determine Spatial Area of Interest

The geographic area to be analyzed was identified and defined by a grid system. This area was approximated as the Washington border on the north to the California border on the south, and was bounded on the east and west by the Cascade Mountain Range and the Pacific Coast, respectively. This area was then divided into a 7x7 gridded system based on the World Geodetic System of 1984 (WGS84) datum. Accordingly, this area was then defined by the latitudes of 46.0 and 42.0, and the longitudes of -124.6 and -122.0, with the interior gridlines being equally spaced, as depicted in Figure 2.2. The intersections of each of the gridlines were used to establish the location of a point, which was defined by a latitude and longitude.

2.7.1.3 Identify Seismic Hazards

The seismic hazard of interest was defined as being the Cascadia Subduction Zone, and the associated interplate earthquakes, which correspond to magnitude 8.3 and 9.0 earthquakes along the Oregon and Washington coasts. This hazard was selected, because the primary purpose of this study is to determine the relative contribution of the Cascadia subduction zone earthquakes to the uniform hazard maps.

2.7.1.4 Determine Applicable Attenuation Equations

It was determined from the 2002 documentation of the uniform hazard maps that the ground acceleration that originates from the Cascadia subduction zone interplate earthquakes was calculated through the use of Youngs et al. 1997 and Sadigh et al. 1997 *(Frankel et al. 2002)*. These equations were then obtained from the original publications, and the appropriate constants were selected from the associated publications for each of the appropriate spectral accelerations. As noted above, the equation that was originally reported in Sadigh et. al. 1997 was found to contain an error, and accordingly, the corrected version was used for the calculations.

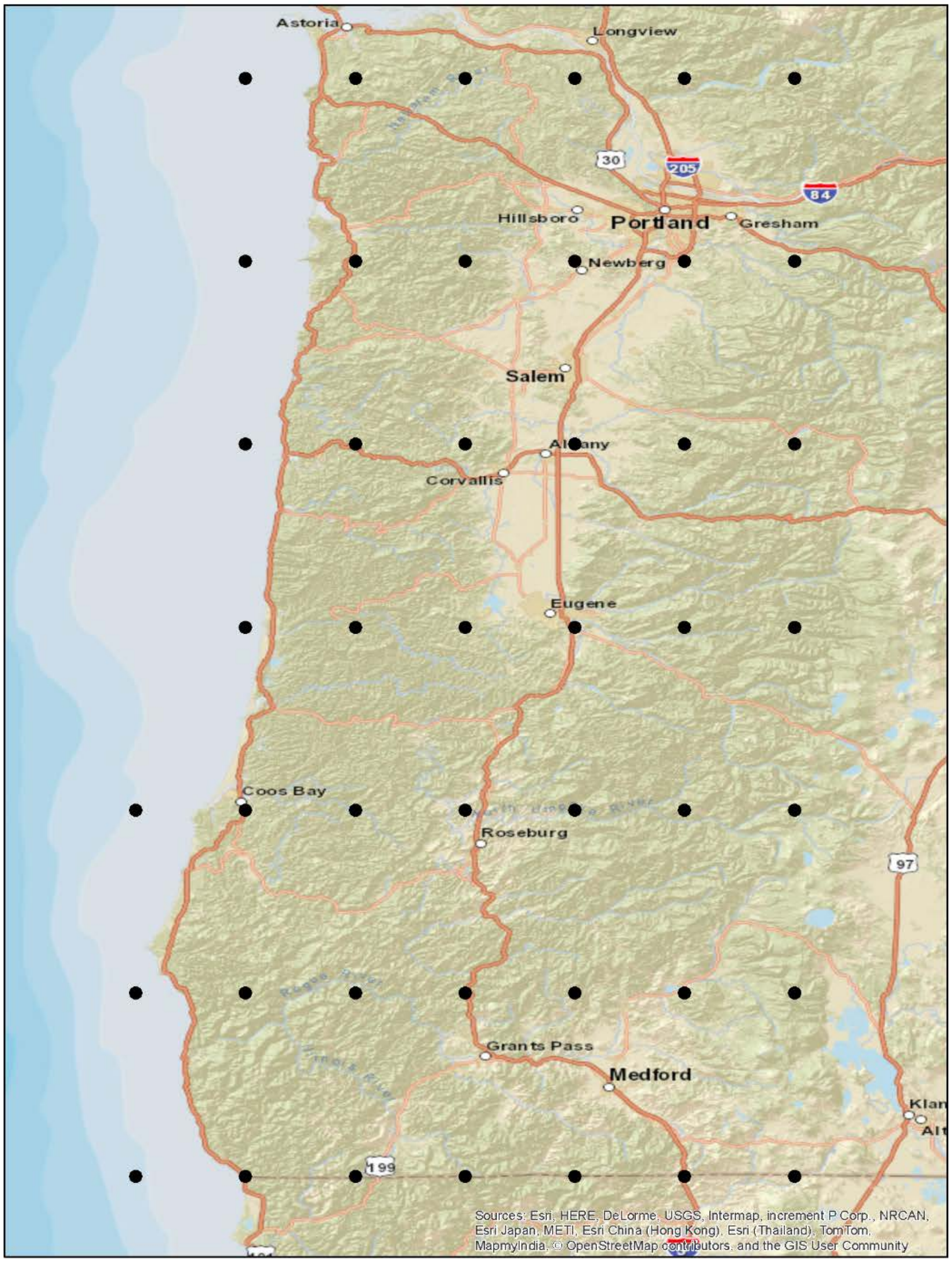

Sources: Esri, HERE, DeLorme, USGS, Intermap, increment P Corp., NRCAN, Esri Japan, METI, Esri China (Hong Kong), Esri (Thailand), TomTom, MapmyIndia, © OpenStreetMap contributors, and the GIS User Community

Figure 2.2: Grid system used to calculate the ground acceleration for the 2002 DSHA

2.7.1.5 Obtain Ground Acceleration Values from 2002 Uniform Hazard Maps

Using the latitude and longitude of each of the points on the grid, the ground acceleration values depicted in the 2002 Uniform Hazard Maps were obtained and tabulated. However, for the 2002 edition, uniform hazard maps were only generated for the return periods of 475 and 2475 years. Accordingly, in order to calculate the ground acceleration values for the other return periods of interest, the Java Ground Motion Parameter Calculator was downloaded from the USGS website. Using the "Probabilistic hazard curves" analysis option, the ground motion values were determined as a function of the latitude, longitude, hazard curve, and return period.

2.7.1.6 Download Deaggregated Data

The distances and magnitudes of the seismic sources that contribute to the ground acceleration at each of the grid points were then determined. This was achieved through the use of the 2002 Interactive Deaggregation application located on the USGS website. Using this application, the latitude and longitude of a map point were entered, as well as a return period of interest, and a spectral acceleration. The resulting output of the Interactive Deaggregation was a text (.txt) file, which contained the PGA, 1.0 sec and 0.2 sec spectral accelerations in three blocks of text. This process was then repeated for all of the data points in the grid, for each of the return periods of interest.

2.7.1.7 Apply Attenuation Equations and Weighting

Once data had been downloaded and imported into Excel for all of the grid points, and for each of the return periods of interest, the appropriate attenuation equations were then applied to each of the Magnitude-Distance (M-R) pairs. These M-R pairs were those associated with the shallow interplate subduction earthquakes generated by the Cascadia Subduction Zone, and were depicted in the data as possessing a magnitude of either 8.3 or 9.0. At each location, the M-R pair with the smallest source-to-site distance was selected. Accordingly, the Youngs and Sadigh equations noted above were applied to each of the Cascadia subduction zone interplate earthquakes. The two equations were then weighted based on the distance from the source to the grid point, following the system noted in Table 2.2.

2.7.1.8 Tabulate all Ground Motion Values

Once the ground motions had been calculated for all of the points in the grid system for a given spectral acceleration and return period, these values were tabulated in Excel, in addition to the latitude and longitude of the data points. This was repeated for all of the spectral accelerations and return periods of interest, which resulted in a total of 12 "grids" of ground acceleration. These ground acceleration values were then compared to the uniform seismic hazard values obtained from the Java Ground Motion Parameter Calculator in 2.7.1.5. In order to compare these accelerations, the ratio between the two values was calculated, and the ratio and the latitude and longitude of each grid point were tabulated.

2.7.1.9 Generate Maps Depicting Ratio of Ground Motion

In order to generate maps that depicted the ratio of ground motion for Western Oregon, ArcGIS was used to interpolate between the data points. First, an appropriate basemap was selected, which depicted the highway system of Oregon. The latitude, longitude, and ratio values for one of the grids was imported into ArcGIS using the “Add XY Data” feature, which plotted each of the data points on the basemap. Using the Spline Interpolation feature of the Arc Toolbox, a plot was generated that depicted the ratio throughout the grid. Further, using the Contour List feature, a single contour was generated that represented a ratio of unity. This process was then repeated for all return periods and spectral accelerations of interest, which resulted in a total of 12 maps, which are depicted in the Appendix (Figure A- 1 through Figure A- 12).

2.7.2 2002 Deaggregated DSHA versus 2002 Scenario DSHA

2.7.2.1 Adopt Grid system and spectral Accelerations from Part I

For this section, the same grid system and Deterministic seismic hazard analysis results that were developed in Section 2.7.1 were used to generate the comparison maps. Likewise, the spectral accelerations of PGA, 0.2 second, and 1.0 second from Section 2.7.1 were also used. However, the return period was not a factor in the comparison, as Deterministic seismic hazard analysis typically does not consider return period in the calculation of ground acceleration.

2.7.2.2 Obtain Acceleration Values from 2002 S-DSHA data

The data files that contained the results from the 2002 and 2008 Scenario Deterministic seismic hazard analysis of Cascadia were obtained from ODOT. The files included the acceleration values for the PGA, 0.2 second, and 1.0 second spectral acceleration, as well as a memo from Art Frankel outlining the methodology of the analysis. The data from these text files was imported into Excel, and the acceleration values for the grid coordinates of interest were extracted. For the grid points that did not correspond with the data files, the values for those points were determined through linear interpolation between adjacent coordinates.

2.7.2.3 Determine Ratio of 2002 D-DSHA versus 2002 S-DSHA

These values were then compared to the Deterministic seismic hazard analysis values obtained by the authors of this study. This was achieved by dividing the Deaggregated Deterministic seismic hazard analysis values by the values that were obtained from the data file, for each of the three spectral accelerations. The return period was not considered.

2.7.2.4 Depict Ratio Graphically

As in Section 2.7.1, a series of maps were created in ArcGIS, which depicted the ratio of the two ground accelerations, for the geographic area of interest, for each of the spectral accelerations.

2.7.3 2002 Scenario DSHA Data versus 2008 Scenario DSHA Data

2.7.3.1 Obtain Raw Data from 2002 and 2008 USGS Scenario DSHA

The two files containing the raw acceleration data for the 2002 and 2008 attenuation equations were obtained, and were differentiated by containing either "odot" or "or" within the file name, respectively *(Frankel 2013)*. These files contained the ground acceleration in "% g" for 0.2 degree increments of latitude and longitude, and included much of Oregon.

2.7.3.2 Truncate Data

The data was contained within a series of text files, and the contents of each of the text files were imported into Excel for each of the spectral accelerations. The data was then truncated for each of the files in order to only depict the grid points to the west of the Cascade Mountains, which was more comparable to the original study area. However, this truncation did not alter the resolution of the data used, and the 0.2-degree spacing used in the data files was maintained.

2.7.3.3 Determine Ratio of Values

The ratio between the ground acceleration from the 2002 and 2008 data was determined by dividing the 2002 values by the 2008 values, for each of the respective return periods and spectral accelerations.

2.7.3.4 Depict Spatially

These ratios were then depicted spatially through the use of ArcGIS, which resulted in a graphical depiction of the ratios for the PGA, 0.2 second, and 1.0 second spectral accelerations.

2.8 SUMMARY OF RESULTS

2.8.1 2002 Deaggregated DSHA versus 2002 Uniform Hazard

2.8.1.1 Explanation of the Comparison Maps

In order to compare the uniform hazard values to the D-DSHA of a M9.0 event from the Cascadia subduction zone, a series of maps were created, an example of which is depicted in Figure 2.3. These maps are presented in the Appendix A of this report. The ground motion comparison maps depict the ratio between the results of the D-DSHA and uniform hazard values, which were calculated using the equation:

$$\frac{2002\ D-DSHA}{2002\ Uniform\ Hazard} \tag{2.4}$$

Accordingly, locations on the map that experience a ratio greater than unity indicate that the ground motions predicted to occur from the Cascadia subduction zone are greater than those from the uniform hazard maps. As noted in the legend, these areas are depicted through the use of warmer colors, such as red and orange. Likewise, a ratio less than unity indicates that the predicted ground acceleration is lower than those depicted in the uniform hazard maps, and these locations are denoted with cooler colors. The gradients have been standardized within return periods to allow for comparison between spectral accelerations. Lastly, areas in which there is a ratio of unity are depicted with a black contour line, which indicates that the acceleration values from the uniform hazard map are the same as the Cascadia subduction zone acceleration values.

2.8.1.2 108 Year Return Period

The maps in the 108 year return period each show a number of similar trends when depicting the ratio between the uniform hazard maps and the Cascadia subduction zone. These figures indicate that the expected ground acceleration values from the 2002 D-DSHA of the Cascadia subduction zone are consistently higher than those depicted on the 2002 Uniform Hazard Maps. The largest ratio tends to occur along the Central Oregon Coast, bounded by Coos Bay on the south to Seaside to the north. The lowest ratio tends to occur near the Portland Metro area, although a low ratio also occurs near Medford.

- The PGA map for the 108 year return period is depicted in Figure A- 1. These values range from a ratio of 11.75 along the Oregon Coast to approximately 1.5 in the Portland Metro area.

- The map for the 0.2 second spectral acceleration is depicted in Figure A.2. From this figure, it appears that the maximum ground acceleration occurs along the Oregon Coast, north of Coos Bay, with a ratio of nearly 13. Further, the smallest ratio of about 1.6 occurs near Portland.

- Lastly, Figure A.3 depicts the comparison for the 1.0 second spectral acceleration. The ratio varies between 16.2 along the Central Oregon Coast to 2.3 southeast of Medford.

2.8.1.3 475 Year Return Period

Further, each of the maps from the 475 year return period also follows a general trend in the ratio between ground acceleration values. Unlike the 108 year return period, there are portions of the 475 year return period maps that have predicted Cascadia subduction zone values that are lower than the uniform hazard values. These areas tend to be centered on the Portland Metro area, and include Hillsboro and Newberg, as well as a portion of the state to the east of Medford. The majority of the study area, however, is denoted with a ratio greater than one, indicating that the Cascadia subduction zone values are greater than the uniform hazard values. The largest ratio occurs in the Oregon Coast Range to the west of Roseburg and Grants Pass, which includes Highways 38, 42, and 199. As one approaches the Coast, the ratio tends to decrease, although they remain greater than one.

- The PGA map for the 475 year return period is depicted in Figure A.4. As noted above, the largest ratio of 2.2 occurs in the Oregon Coast Range between Coos Bay and Grants Pass, and extends roughly north and south. The ratio decreases along the coast, with values ranging from 1.25 near Coos Bay to approximately 1.7 near Tillamook. As one extends further inland, the ratio decreases, and reach a ratio of 0.81 in the downtown Portland area.

- As depicted in Figure A.5, both the overall trend and the values of ratio for the 0.2 second spectral acceleration are nearly identical to the PGA values. According the maximum ratio of 2.1 occurs in the Southern Oregon Coast Range, and the lowest ratio occurs in the Portland Metro Area.

- The map for the 1.0 second spectral acceleration is shown in Figure A.6. Unlike the PGA and 0.2 second spectral acceleration maps, the ratio values are greater than unity for nearly the entire map. The largest values occur in the same general area as noted above, with a maximum ratio of 2.3. In the Portland area, the ratio is approximately 1.1, and a small area with a ratio of less than one occurs south-east of Medford.

2.8.1.4 975 Year Return Period

The 975 year return period maps depict a similar distribution of ground acceleration values. The maximum ratio is located in the Southern Oregon Coast Range between Grants Pass and Coos Bay, while the lowest ratio occurs near Portland. Accordingly, most of the Willamette Valley from Salem northward is expected to experience ground acceleration values lower than those depicted in the uniform hazard maps. However, several cities south of Salem, including Corvallis, Eugene, Roseburg, and Grants Pass are expected to experience acceleration values greater than those from the uniform hazard maps.

- For the PGA map of the 975 year return period, as shown in Figure A.7, the maximum ratio of 1.2 occurs between Grants Pass and Coos Bay. The majority of the Oregon Coast Range also has ratios greater than one, including the southern half of the I-5 corridor. The majority of the Oregon Coast and the Northern Willamette Valley will experience unit or lower ratios between the Cascadia subduction zone and uniform hazard accelerations. The Portland area is denoted as having a ratio of 0.6.

- The 0.2 second spectral acceleration map, depicted in Figure A.8, is nearly identical in the ratio of acceleration values to the PGA map for the 975 year return period.

- Figure A.9, shows the 1.0 second spectral acceleration map. This figure shows that both Roseburg and Grants Pass are predicted to experience Cascadia subduction zone accelerations 1.2 greater than the uniform hazard values. Further, most of the southern half of the I-5 corridor and the northern coast are also depicted as having ratios greater than one. However, the southern coast and the

Northern Willamette Valley are indicated as having lower ratios, with Portland having a value of approximately 0.73.

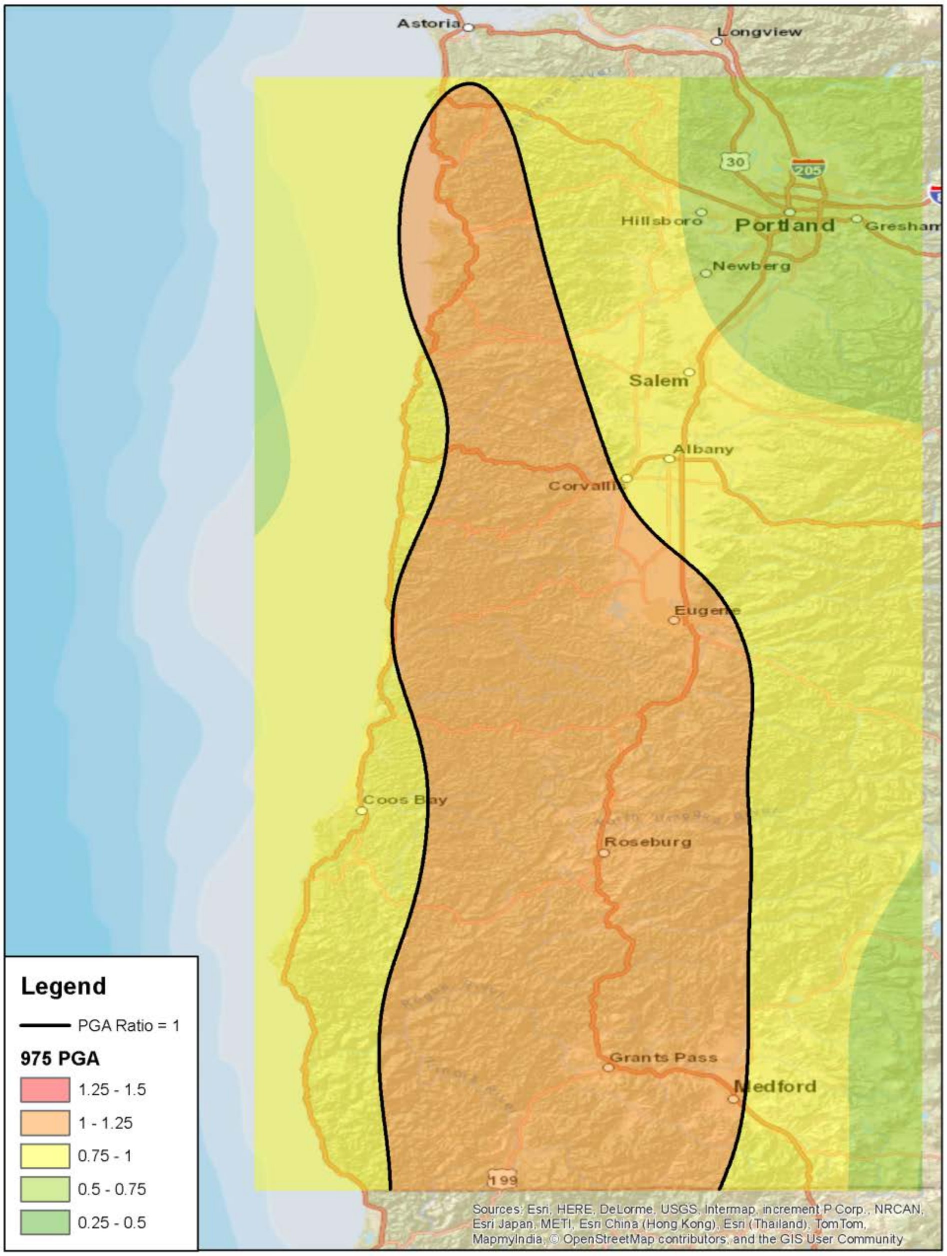

Sources: Esri, HERE, DeLorme, USGS, Intermap, increment P Corp., NRCAN, Esri Japan, METI, Esri China (Hong Kong), Esri (Thailand), TomTom, MapmyIndia, © OpenStreetMap contributors, and the GIS User Community

Figure 2.3: Illustrative sample of comparison between CSZ ground acceleration and uniform hazard acceleration values

2.8.1.5 2475 Year Return Period

The 2475 year return period maps indicate that the ratio throughout the study area are consistently below unity; that is, that the ground acceleration values from Cascadia are reliably lower than the values depicted on the 2002 Uniform Hazard Maps. The acceleration values are most similar in the southern and central Oregon Coast Range, and have the greatest difference in the Northern Willamette Valley.

- Figure A.10 and Figure A.11 depict the PGA and 0.2 second spectral accelerations, respectively. As in the other return periods, the greatest ratio of 0.76 occurs west of Grants Pass, while the lowest ratio of 0.33 occurs to the east of Medford. The Portland area is denoted as having a ratio of 0.41.

- The 1.0 second spectral acceleration values, from Figure A.12 and Figure A.13, experience less variation in the ratio, relative to the PGA and 0.2 second spectral acceleration maps. Accordingly, these values tend to be between 0.78 and 0.41, with the distribution occurring as described above. Portland has a ratio of about 0.5 for this spectral acceleration and return period.

2.8.2 Deaggregated DSHA versus 2002 Scenario DSHA

In order to compare the values obtained from the 2002 D-DSHA to the values from the 2002 S-DSHA, the ratio of the D-DSHA was divided by those from the 2002 USGS data files. The other aspects of the maps, including the coloring scheme and the use of the black contour line to represent a ratio of unity, are the same as in Section 2.8.1.

As depicted in Figure A.13, the PGA ground acceleration values calculated in this study are typically larger than those from the 2002 S-DSHA. The largest discrepancy is in Southwest Oregon, to the west of Roseburg; in this area, the ratio of the values is about 1.6. However, for the remainder of the state, the values are much more comparable. In the Portland Metropolitan Area, the ratio of values is approximately 1.18, which indicates that the two acceleration predictions are relatively close.

This comparison was also performed for the 0.2 second spectral acceleration, as shown in Figure A.14. The ratio between the two values is similar to that of the PGA comparison, with a ratio of approximately 1.6 in the Southern Oregon Coast Range. The ratio is still relatively low in the northwestern part of the state, with a ratio of 1.1 near Portland.

Lastly, the 1.0 second spectral acceleration comparison is shown in Figure A.15. In this figure, one can determine that there is a significant discrepancy between the values calculated in this study with those calculated by USGS. This results in a ratio of 1.65 in the Southern Oregon Coast Range, west of Roseburg. The ratio decreases as one travels either east or west, and reaches a minimum of 1.16 near Portland.

2.8.3 2002 versus 2008 Scenario DSHA Data

Figure A.16, Figure A.17, and Figure A.18, depict the ratio of the 2002 to 2008 attenuation equation values for the PGA, 0.2 second, and 1.0 seconds spectral accelerations, respectively. From Figure A.16, it appears that the 2002 attenuation equations predicts larger acceleration values than the 2008 attenuation equations near the coast, and to the west of Medford. Between these two bounds, the 2008 attenuation equations predict greater values, and this trend is observed in a wide band running north-south along the I-5 Corridor. The greatest difference between the two attenuation equations appears to be about 20% in both cases.

For the 0.2 second spectral acceleration, a similar trend is observed, in that the ratio of the accelerations is largest along the coast, and to the west of the I-5 Corridor, with the ratio nearing 1.25 for both extremes. However, the ratio is consistently above 1 for the entire map, although the values are very close along the Willamette Valley.

Lastly, the 1.0 second spectral acceleration figure shows that the 2002 DSHA results in considerably larger accelerations than the 2008 DHSA, with the ratio nearing 1.4 along the coast, and 1.3 along the Cascades. As with the other spectral accelerations, the ratio is smaller along I-5, although it is still notable.

2.9 INTERPRETATION OF RESULTS

Based on the aforementioned summary of results, one can infer a number of patterns about the relationship between the ground motion from a Cascadia subduction zone event and the uniform hazard spectra.

2.9.1 2002 Deaggregated DSHA versus Uniform Hazard

2.9.1.1 General Trends

One general trend among all four return periods that is worth noting is that there appears to be a relation between magnitude of the ratio and the length of the spectral acceleration period. Namely, the ratio appears to be lowest for the peak ground acceleration, which has a corresponding spectral acceleration of 0 seconds. When compared to the 0.2 seconds spectral acceleration, it appears that the ratio increases slightly for many points on the map, indicating that the gap between the Cascadia subduction zone ground acceleration values and the uniform hazard values grows slightly. However, by comparing the 0.2 seconds spectral acceleration and 1.0 second spectral acceleration, one can see that the ratio has increased dramatically with the increasing spectral acceleration. Accordingly, one can infer that the response spectra for the Cascadia subduction zone and uniform hazard diverge as the spectral acceleration values increase. This trend generally holds for all four return periods, although it is less pronounced for the 2475 year return period. Further, this trend is likely of particular interest to ODOT, as many bridges possess longer periods, and accordingly, will be increasingly under designed as the structures become larger.

2.9.1.2 108 Year Return Period

As noted above, the predicted ground motion from a M9.0 Cascadia subduction zone event is significantly higher than the values denoted by the uniform hazard. This is likely due to the longer recurrence interval of events from the Cascadia subduction zone, which tend to have recurrence interval of 300 to 600 years. Accordingly, the ground accelerations from the 108 year return period map will be dominated by smaller surface faults with much shorter return periods. This assumption is further supported by the observation that the ratio increases dramatically along the coast, where the influence of Cascadia tends to dwarf the smaller crustal faults for the overall region.

2.9.1.3 475 Year Return Period

The 475 year return period was of particular interest for this study, as these acceleration values are used by ODOT for the "500-year Serviceability Criteria". For both the PGA and 0.2 second spectral acceleration maps, much of the western area of the maps are predicted to have ground accelerations that are larger than those depicted in the uniform hazard maps. Accordingly, several highways, such as U.S. Route 199, OR 42, and OR 38 are predicted to experience over twice the ground acceleration as denoted in the uniform hazard maps. Likewise, several other highways such as US Routes 26, 101, 20, and Interstate 5 are expected to experience accelerations that are over 2 times greater. For longer period structures such as bridges, this difference is further amplified as denoted in the 1.0 second spectral acceleration map. From this, one can tentatively infer that many of the structures on major Oregon highways through the coast range, and the southern coast range in particular, are under designed for a Cascadia subduction zone event.

2.9.1.4 975 Year Return Period

Likewise, the 975 year return period was studied because it corresponds with the "1000-year No-Collapse Criteria". As in the 475 year return period, many of the highways through the central and southern coast range are located in areas that experience a discrepancy between acceleration values. However, the magnitude of this difference is much lower than the 475 year return period, typically being less than 20% for all of the spectral accelerations. Nonetheless, this area includes several major highways, including Interstate 5, US 20, and sections of US 26 and US 101. While the ratio is lower than the serviceability criteria, a 20% under prediction of ground acceleration is significant nonetheless. Because these values are the basis for the collapse prevention criteria, underestimating these acceleration values may compromise the ability of transportation infrastructure in the Oregon Coast Range to withstand a M9.0 Cascadia subduction zone event.

2.9.1.5 2475 Year Return Period

Lastly, for the 2475 year return period, the values depicted in the 2002 Uniform Hazard Maps are consistently higher than those expected from a Cascadia subduction zone event. While ODOT does not use this return period for the design of bridges, this return period is used by several codes such as IBC and ASCE.

2.9.2 2002 Deaggregate DSHA versus 2002 Scenario DSHA

As noted above, the values that were obtained by the authors of this study were typically higher than those that were obtained from the 2002 S-DSHA data. In some cases, these values were significantly higher, with a ratio of 1.65 being observed for the 1.0 second spectral acceleration. Theoretically, these values should be comparable, as the same attenuation equations were being used to analyze M-R pairs that originate from similar sources.

A possible explanation for the inconsistency of values is due to the method in which the M-R pairs were obtained in order to generate the acceleration data. For the data produced by the authors of this study, the M-R pair was selected from the deaggregated data that would produce the largest ground acceleration for each point. Accordingly, this selected the "worst case scenario" for each point on the map, without defining a consistent fault line, which created an envelope of all of the possible Cascadia subduction zone rupture paths. Further, as noted before, the depth was assumed to be a constant 20 kilometers to the hypocenter for all points. In contrast, the data that was generated by Frankel and the USGS was based on the geometry used in the Mw 9.0 Shakemap scenario from the USGS website (Frankel 2013). This model utilizes a fault surface, which were defined with a series of coordinates (USGS 2011). Further, this fault surface had a varying depth, ranging from 3.7 kilometers to 55 kilometers in depth to the hypocenter. Accordingly, this discrepancy in fault geometry and hypocenter depth may explain the difference in acceleration values.

It is interesting to note that the values that were produced by the ODOT seismic design spreadsheet, titled "OReSpect_V2014 03", were compared to the raw data from the DSHA performed by the USGS with the 2002 and 2008 attenuation equations. It was found that while the spreadsheet was believed to be based on the 2002 attenuation equations, the values that were produced were actually identical to the data from the 2008 attenuation equations. Further, as denoted in Figure A.16, Figure A.17, and Figure A.18, and discussed in the following section, the 2008 attenuation equations result in lower accelerations than the 2002 equations. Accordingly, ODOT may wish to verify which set of DSHA results should be used as the basis for the design spreadsheet.

2.9.3 2002 versus 2008 Scenario DSHA Data

From Figure A.6 through Figure A.18, one can infer that the 2002 attenuation equations typically predict larger ground accelerations than the 2008 attenuation equations for the same M-R pair. The exception to this is the Willamette Valley for the PGA spectral acceleration. This indicates that the 2008 attenuation equations are more conservative that those used in the 2002 Uniform Hazard Maps. However, one cannot ascertain from these figures which equation set is more indicative of the true ground acceleration that will result from a Cascadia Subduction Zone Event.

Further, one can also ascertain that this conservatism increases proportionately with the spectral acceleration. This indicates that the two response spectra are comparable at low structural periods, and proceed to diverge as the period increases, with the 2002 response spectra being greater. This is likely due to a combination of the nature of the attenuation equations, in that different fault types result in different response spectra, as well as the different weighting that was applied between the two attenuation sets.

Lastly, it is interesting to note that the ratios are relatively large at small site-to-source distances, become smaller with intermediate distances, and then become larger again at large distances. This is also likely due to a combination of the nature of the attenuation equations, as well as the different weighting schemes that were applied. This suggests that the slopes of the acceleration versus distance are not the same for the two equation sets, with the 2002 equation resulting in a greater rate of slope change than the 2008 equations.

2.10 SUMMARY

The purpose of this task was to determine how the ground acceleration values denoted in the 2002 Uniform Hazard Maps compare to the ground accelerations expected from a megathrust subduction earthquake originating from the Cascadia Subduction Zone. In order to calculate the ground acceleration values for the Cascadia subduction zone, a deterministic seismic hazard analysis was performed using the same attenuation equations as the 2002 Uniform Hazard Maps. These values were then compared to the uniform hazard accelerations by computing the ratio, and these values were depicted graphically through the production of a series of maps. From these comparison maps, the difference between the Cascadia subduction zone values and the uniform hazard values increases as a function of the period of the structure.

For the 108 year return period, the uniform hazard values are significantly lower than the Cascadia subduction zone accelerations, as related to the longer return period of the Cascadia subduction zone events. Conversely, for the 2475 year return period, the Cascadia subduction zone values are consistently lower than those that originate from the uniform hazard. However, for the 475 year return period, which corresponds to ODOT's 500-year Serviceability Criteria, the 2002 Uniform Hazard Maps would under predict the ground acceleration for majority of the highways through the Oregon Coast Range with the exception of the Greater Portland Metro area. Even the 975 year return period, which corresponds to ODOT's 1000-year No-Collapse Criteria, shows significant areas between the coast and I-5 where accelerations exceed the 2002 Uniform Hazard Maps.

Additionally, it was found that the values from the 2002 D-DSHA (deaggregated) are typically higher than those that were generated by the 2002 S-DSHA (scenario). This was believed to be because the difference in fault zone geometry. Whereas S-DSHA uses a defined fault surface and varying hypocenter depth, D-DSHA uses the deaggregated data to select the closest possible fault source, and uses a constant 20 km hypocenter depth. Further, the values from the 2002 and 2008 Scenario DSHA were compared, in order to aid ODOT in comparing the two sets of attenuation equations. It was found that the 2002 equations typically predict larger ground accelerations than the 2008 equations.

3.0 SEISMIC ACCELERATION VALUES FOR THE FULL RUPTURE CSZ USING USGS 2014 METHODOLOGY

3.1 GENERAL

The process used to estimate the acceleration values of the CSZ hazard had significantly changed for the 2014 adoption of the USGS hazard. The model developed for this study calculated the peak ground acceleration (PGA) and pseudo accelerations at two spectral periods, 0.2 and 1.0 second (s), for a full rupture M9 CSZ earthquake. The methodology adopted was consistent with the USGS approach and is referred to as 14CSZ. The results from this model were compared to two different models previously produced by the United States Geological Survey (USGS). One model type was a Deterministic Seismic Hazard Analysis, which will be denoted 02CSZ, and the other was a Probabilistic Seismic Hazard Analysis, which will be denoted PSH. There were different PSH models for serviceability and life safety seismic hazards. The serviceability model used a 14% chance in 75 years earthquake, which represented a 500-year return period (497 years). The life safety used a 7% chance in 75 years earthquake, which represented a 1000-year return period (1034 years). The 02CSZ model calculated acceleration values for a M9.0 earthquake caused by the CSZ as based on the 2002 USGS hazard. The acceleration values calculated by all of the USGS models were PGA and pseudo accelerations at 0.2s and 1.0s, which correspond to reference periods used to calculate the response spectrum. The definition of the specific models used in this Chapter are summarized below.

- 14CSZ: a deagragated deterministic model produced by the authors with the 2014 USGS logic tree, fault surface locations, and attenuations.

- 02CSZ: a deterministic model produced by USGS with the 2002 attenuations and fault geometry.

- 02PSH500: a probabilistic model for a 14% chance in 75 years earthquake produced by USGS for the 2002 update to the National Seismic Hazard Maps.

- 02PSH1000: a probabilistic model for a 7% chance in 75 years earthquake produced by USGS for the 2002 update to the National Seismic Hazard Maps.

- 14PSH500: a probabilistic model for a 14% chance in 75 years earthquake produced by USGS for the 2014 update to the National Seismic Hazard Maps.

- 14PSH1000: a probabilistic model for a 7% chance in 75 years earthquake produced by USGS for the 2014 update to the National Seismic Hazard Maps.

All of the models examined in this study calculated the acceleration values for a grid of longitude-latitude points across the state of Oregon. The main outcome of this study was a data set of the acceleration values for each longitude-latitude point produced by the 14CSZ model. This grid of acceleration values was visually represented as a set of color contour maps depicting

PGA, the 0.2s and 1.0s pseudo accelerations across the state of Oregon. Another outcome of the study was the comparison of the 14CSZ model to the alternate models produced by USGS. The 14CSZ model was compared to the other models by calculating a ratio between the acceleration value produced by 14CSZ and the value produced by the alternate model for a given grid point. This process was repeated for the entire grid. To calculate the ratio, the 14CSZ value was always divided by the alternate value. A set of color contour maps was produced that displayed the ratio values for each model comparison. The final outcome of the study was a ratio comparison between the 14PSH and 02PSH models for serviceability and life safety seismic hazards. This comparison was represented by color contour maps as well.

3.2 METHODS

3.2.1 USGS Inputs Used in the 14CSZ

The logic flow for the 14CSZ model, attenuation equations, Cascadia subduction zone fault surface geometry, and moment magnitudes were adapted from the USGS 2014 update to the National Seismic Hazard Maps *(Chen, Frankel and Peterson 2014)*. The 14CSZ model calculated accelerations for a full rupture scenario, and as a result only that branch of the logic tree was used (Figure 3.1). Three different terminuses to the Cascadia subduction zone fault surface were used to capture the different possible extents of the rupture plane. These were the top of the non-volcanic tremor zone (deepest), the 1cm/yr locking contour (middle), and the midpoint of the fully locked zone and 1 cm/yr locking contour (shallowest). Each of these terminuses were located relative to the Cascadia subduction zone fault surface upper boundary described as the up-dip edge. For each of the three fault surface extents, three possible moment magnitude values were given for a full rupture scenario (Table 3.1). The moment magnitude values used for the deepest fault surface were 9.34, 8.85, and 9.01. The values used for the middle surface were 9.12, 8.69, and 8.82. The values used for the shallowest fault surface were 9.01, 8.61, and 8.72. The three different lines that delineated the terminuses to the fault surfaces and the line that identified the upper boundary were defined by sets of points. Each of the points was described by a longitude, latitude, and depth value. These values are shown in Table 3.2.

In order to calculate acceleration values for the entire state of Oregon, a grid of points was developed. Each point in the grid was defined by a latitude and longitude value. The spacing of the grid points was 0.05 degrees latitude and longitude. In total there were 18,511 longitude-latitude points in the rectangular grid. The location of the three fault surfaces and the grid are depicted in Figure 3.2. Some of the models used in the ratio comparisons produced data for grids that were a slightly different size or point spacing. When this was the case the 14CSZ grid was adjusted to match the grid of the other models.

The attenuation equations used were Atkinson and Boore *(Atkinson and Boore 2003)*, Atkinson and Macias *(Atkinson and Macias 2009)*, Zhao et al. *(Zhao et al. 2006)*, and BC Hydro *(Addo et al. 2012)*. The attenuation equations were weighted as follows: Atkinson and Boore 2003 Global - 0.1, Atkinson and Macias 2009 - 0.3, Zhoa et al. 2006 - 0.3, and BC Hydro 2012 - 0.3. For the Atkinson and Boore 2003 Global equation an interface event was assumed and the acceleration

Table 3.1: The moment magnitude values for a full rupture of the CSZ fault *(Chen, Frankel and Peterson 2014)*:

Rupture Scenario	**Down-dip Option**	**3D Rupture Area (km$^{2)}$**	**Papazachos et al. (2004)**	**Strasser et al. (2010)**	**Murotani et al. (2008)**
Case A	Shallowest	84607.28	9.01	8.61	8.72
	Middle	106110.90	9.12	8.69	8.82
	Deepest	163956.66	9.34	8.85	9.01

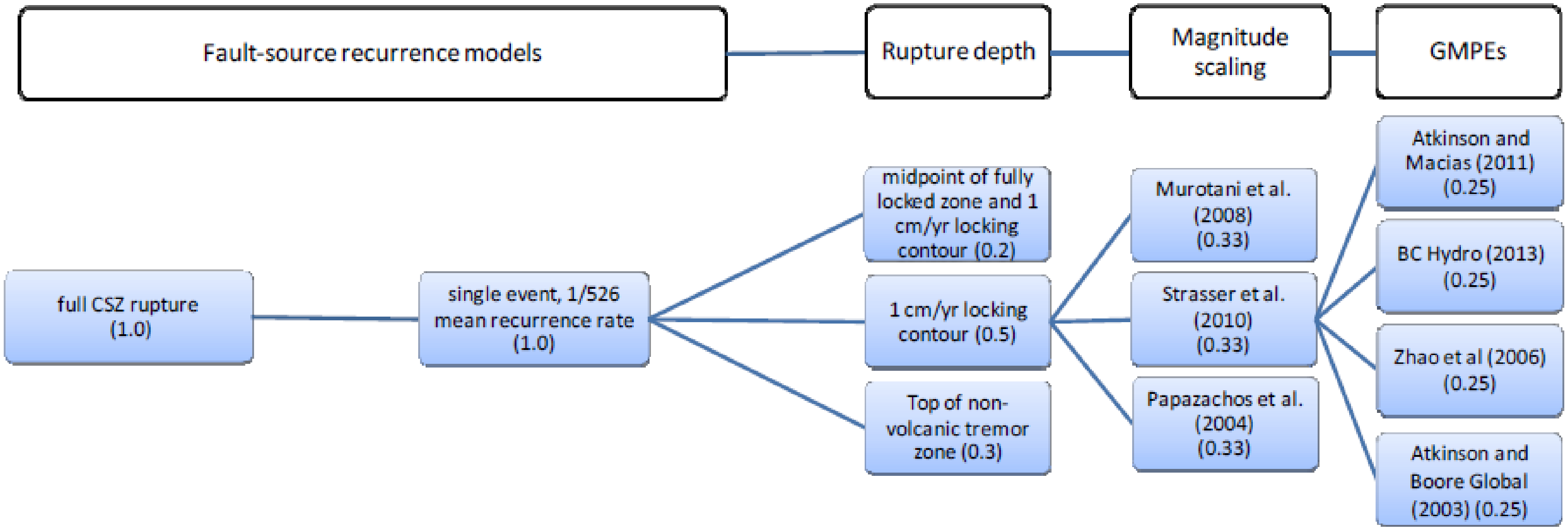

Figure 3.1: The logic tree used to calculate accelerations caused by a full rupture of the CSZ fault *(Peterson et al. 2014)*

Table 3.2: The latitude, longitude, and depth values for the points that defined the three different fault surface locations *(Chen et al. 2014)*

Down-dip edge									Up-dip edge		
Top of non-volcanic tremor zone (deepest option)			1 cm/yr locking contour (middle option)			Midpoint of fully locked zone and 1 cm/yr locking contour (shallowest option)					
longitude	latitude	depth (km)	longitude	latitude	depth (km)	longitude	latitude	depth (km)	longitude	latitude	depth (km)
-126.688	49.798	-26.481	-126.828	49.737	-23.691	-127.043	49.619	-19.120	-127.645	49.253	5
-125.859	49.387	-30.035	-126.175	49.214	-22.975	-126.383	49.096	-18.475	-127.080	48.689	5
-125.112	49.039	-32.420	-125.439	48.861	-25.034	-125.749	48.717	-19.011	-126.678	48.278	5
-124.458	48.658	-32.735	-124.804	48.553	-27.841	-125.214	48.413	-21.240	-126.439	47.992	5
-123.917	48.255	-32.443	-124.361	48.152	-27.869	-124.741	48.052	-22.808	-126.234	47.663	5
-123.509	47.780	-33.814	-123.916	47.709	-29.320	-124.334	47.627	-24.469	-126.049	47.279	5
-123.357	47.313	-34.714	-123.899	47.238	-27.913	-124.289	47.183	-23.127	-125.920	46.943	5
-123.352	46.835	-34.745	-124.116	46.779	-23.949	-124.405	46.758	-20.000	-125.816	46.629	5
-123.399	46.377	-34.884	-124.138	46.364	-22.909	-124.432	46.359	-18.595	-125.736	46.330	5
-123.413	**46.300**	**-34.828**	**-124.137**	**46.300**	**-22.928**	**-124.439**	**46.300**	**-18.441**	**-125.729**	**46.300**	**5**
-123.599	45.501	-33.129	-124.330	45.489	-20.210	-124.549	45.485	-16.708	-125.574	45.452	5
-123.702	**45.000**	**-30.998**	**-124.488**	**45.000**	**-17.459**	**-124.561**	**45.000**	**-16.309**	**-125.527**	**45.000**	**5**
-123.734	44.757	-30.306	-124.356	44.742	-19.362	-124.567	44.738	-15.667	-125.500	44.712	5
-123.764	43.882	-29.481	-124.492	43.863	-15.988	-124.630	43.858	-13.991	-125.427	43.841	5
-123.780	**43.700**	**-28.552**	**-124.509**	**43.700**	**-15.277**	**-124.631**	**43.700**	**-13.573**	**-125.411**	**43.700**	**5**
-123.809	42.996	-26.805	-124.514	42.980	-13.663	-124.638	42.975	-11.959	-125.289	42.957	5
-123.662	42.119	-27.892	-124.390	42.112	-12.127	-124.543	42.108	-9.928	-125.047	42.099	5
-123.329	41.215	-29.255	-124.173	41.218	-14.836	-124.348	41.214	-12.702	-125.085	41.214	5
-122.945	40.376	-37.830	-123.829	40.347	-24.018	-124.042	40.347	-22.818	-125.099	40.355	6.745

Note: Entries in bold fonts are northern end points of ruptures.

values were taken to be the log average of B and C site conditions. For the Atkinson and Macias equation no major assumptions were made.

For the BC Hydro 2012 equation an interface event and a shear wave velocity of 760 m/s were assumed. Furthermore, every rupture distance was considered unknown. This consideration was made because no information was provided in BC Hydro's report regarding forearc/backarc distances for the Pacific Northwest. For the Zhoa et al. 2006 equation an interface event and a shear wave velocity of 760 m/s were assumed and the magnitude scaling term was included. The attenuation equations and the parameters associated with them are described in detail in Appendix B.

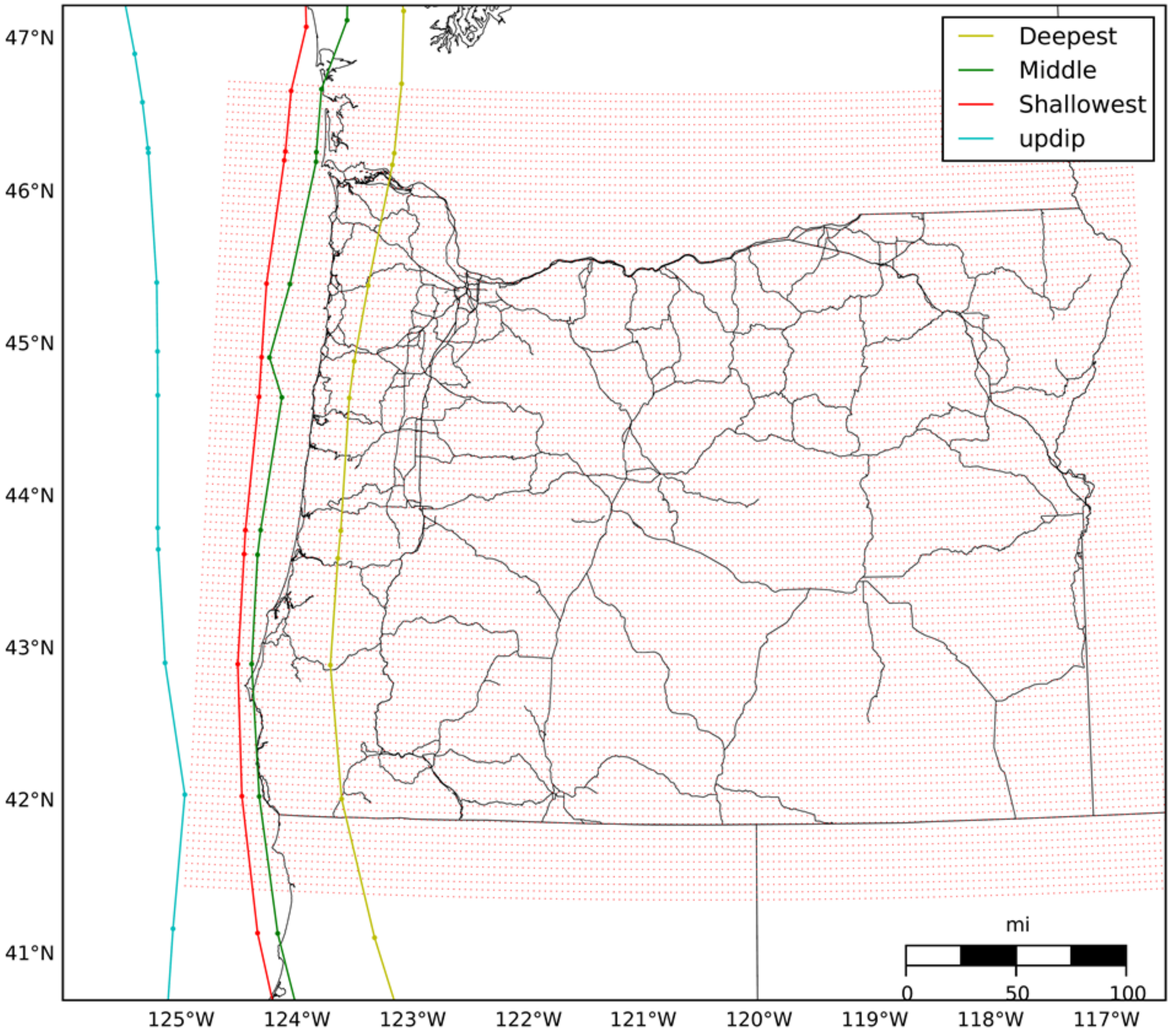

Figure 3.2: The terminuses of the three fault surfaces used to describe the CSZ rupture zone is displayed in red, green, and yellow. The grid of 18,511 points is shown as blue dots.

3.2.2 The 14CSZ Model

The framework of the 14CSZ model was based on information for the update to the 2014 National Seismic Hazard Maps provided by the USGS. The three main facets to this information were the logic flow for the acceleration calculations, the attenuation equations themselves, and the location of the rupture zone. The USGS information was used because it was up to date and allowed for relevant comparison between the 14CSZ model and other USGS models. Aside from the above stated similarities, the methods of 14CSZ model were unique from previous USGS deterministic or probabilistic models for acceleration calculation.

The goal of the 14CSZ model was to calculate the PGA, 0.2s, and 1.0s acceleration values for the 18,511 longitude-latitude points in the rectangular grid. Due to the number of points this was not feasible by hand calculation or in Microsoft Excel. Therefore, a number of scripts were developed in the Python 3.4.3 programing language *(Van Rossum 2015)*. These scripts were able to quickly calculate the acceleration values for the entire grid. During the process of development, many different scripts were written and modified. Only the scripts that were used to produce the final acceleration values were described in this chapter.

For the acceleration calculations, separate scripts were written for the PGA, 0.2s, and 1.0s accelerations. The general logic flow for all three of the scripts was to calculate the acceleration value for each point in the grid based on one of the three fault surface extents. Once all those calculations were complete, the same calculations were computed for the next fault surface. After all the acceleration values were calculated for all three-fault surfaces, the values were averaged for each point in the grid according to the weighting shown in Figure 3.1. This process generated one acceleration value, e.g. PGA, for each point in the grid.

The critical portion of each of the three scripts was the attenuation equations. These attenuation equations required a set of variable inputs that had to be calculated within the flow of the program or uploaded into the program in order to calculate the acceleration values for any one point in the grid. The variables were the hypocentral depth for the relevant fault surface, the moment magnitude values for the relevant fault surface, and the shortest distance from the grid point to the relevant fault surface. For every grid point and fault surface the hypocentral depth was taken to be 20km. The specific moment magnitude values for each fault surface were taken from the USGS 2014 update to the National Seismic Hazard Maps *(Chen et al. 2014)*. Originally the shortest distance calculation was completed in the Python script, however, during the quality checking process errors were found in the distance calculation. These errors were resolved by completing the distance calculation with a built in function in Matlab *(Matlab 2015)*, which calculated the shortest distance from each grid point to each of the three fault surfaces. The distance values were exported from Matlab and uploaded into the Python script that calculated the acceleration values. The exact method used in Matlab for calculating the shortest distance from a grid point to a fault surface is explained in detail in the Appendix C.

The general program logic flow was the same for the three different scripts that calculated the PGA, 0.2s, and 1.0s acceleration values. The only difference between the scripts was the parameters used in the attenuation equations. The program flow for calculating the accelerations for one of the three fault surface locations, e.g. the deepest fault surface in the PGA script, went as follows.

The longitude and latitude values that defined the 18,511 grid points were imported into the script. Then the three moment magnitude values for the deepest fault surface, the hypocentral depth for each grid point, and the shortest distance from each grid point to the deepest fault surface were imported into the script. For each of the moment magnitudes, the four attenuation equations were calculated for each grid point with the shortest distance, depth, and moment magnitude as inputs. The outputs of the four attenuation equations were averaged with the weighting described above to generate one PGA value for each point on the grid for one of the three moment magnitudes. This was repeated for the remaining two moment magnitudes. Finally, the outputs for all three moment magnitudes were averaged to produce one PGA value for each grid point for the deepest fault line.

The same program process was repeated for the middle fault surface and the shallowest fault surface in the PGA script. Once PGA values had been calculated for each point on the grid for the three fault surfaces, these values were averaged with the weighting, 0.2 shallowest, 0.5 middle, and 0.3 deepest, to generate one PGA value for each grid point. At this point a comma-separated values (CSV) file was exported from the script containing the longitude, latitude, and PGA value for each grid point. The final step in the script was to calculate the ratio between the PGA values generated by the script and the PGA values generated by different USGS models. To do this, the values for PGA from the other USGS models were imported into the script from a CSV file. Next, each PGA value from the 14CSV model was matched with the USGS PGA value for the same grid point. The ratio was calculated by dividing the 14CSV value by the corresponding USGS value. This process was repeated for every point in the grid. Finally, more CSV files were exported from the program that contained the longitude, latitude, and ratio values for each grid point for each of the model comparisons. The scripts for the 0.2s and 1.0s accelerations ran in exactly the same manner, and produced the same types of CSV files containing the acceleration and ratio data. A graphical representation of the program flow is provided in Figure 3.3. The ratio comparison between the 14PSH and 02PSH was calculated in a separate script in the same manner. For this comparison the 14PSH value was divided by the 02PSH value.

In order to make the acceleration data from the different USGS models correspond correctly to the data produced by the 14CSZ model, it was necessary to truncate some of the USGS data. This occurred because the USGS data generated by the 02PSH and 14PSH models was calculated for a much larger grid area that had the same grid spacing. Another script was written that parsed out the correct grid points and acceleration values from the 02PSH and 14PSH data sets to match the 14CSZ grid. Moreover, the 02CSZ data was calculated for the same size grid but with a smaller spacing of 0.02 degrees. In order to match this acceleration data correctly to the 14CSZ data, the grid points imported into the 14CSZ script were altered to have the same spacing.

After the acceleration and ratio data were produced, the next step was to create color contour maps of the acceleration data and the ratio comparison data. This was done in Python 3.4.3 as well. One script was written for the 14CSZ acceleration data, which produced color contour maps for PGA, 0.2s, and 1.0s. Four other scripts were written that generated color contour ratio maps for the comparison of 14CSZ to the other models and the comparison of 14PSH to 02PSH. The comparison maps are presented in the Appendix D. The program flow of the color contour map scripts was similar to that of the acceleration scripts.

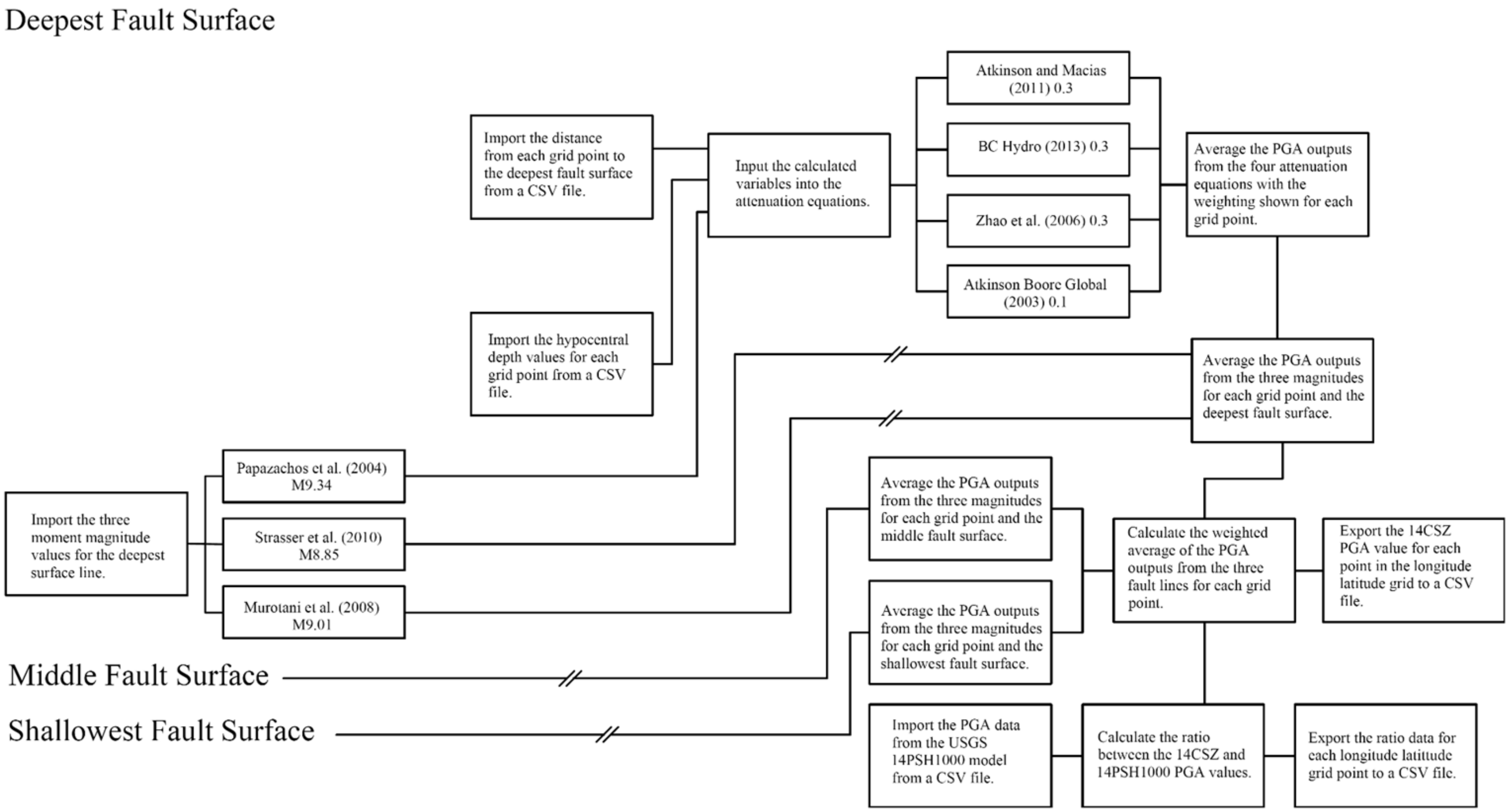

Figure 3.3: A flow chart that shows the process of the Python script that calculated the PGA values for the 14CSZ model. The same program flow was used for the 0.2s and 1.0s acceleration calculations. The ratio calculation was also shown in the chart

To begin, in all the scripts the acceleration (or ratio data) was imported into the script from a CSV file. Next the data was converted from latitude and longitude degrees into the chosen map projection, which was in meters. Finally, the acceleration or ratio data was overlaid on a map of Oregon and exported to a PDF file. For all the maps generated in this study the official map projection for Oregon, EPSG: 2991, was used. EPSG: 2991 was based off a Lambert Conic Conformal projection, and used the NAD83 datum and GRS1980 spheroid *(Oregon Geospatial Enterprise Office 2015)*.

3.3 RESULTS

3.3.1 14CSZ Data

This study had two main results. The first was the acceleration data produced by the 14CSZ model. The 14CSZ model calculated the PGA (Figure D.1) and pseudo accelerations at two spectral periods, 0.2s (Figure D.2) and 1.0s (Figure D.3) which were represented as a fraction of acceleration due to gravity (g). This data was stored in CSV files that can be opened in Microsoft Excel. For each grid point the longitude, latitude, and acceleration values were provided. The data was graphically displayed in the form of color contour maps. These maps used a red color scheme to depict the severity of the acceleration. Lighter colors indicated a smaller acceleration whereas darker colors indicated larger acceleration. The color contours were made to be consistent between the maps. The acceleration values for the contours were marked on the contour lines. As expected the maximum acceleration values for all three maps were located on the CSZ fault. The maximum values were, PGA 0.6220g, 0.2s 1.2495g, 1.0s 0.5216g. All three maximum values were located at -125 degrees longitude and 42.1 degrees latitude. The values for all three acceleration types dissipated rapidly to the east and west of the fault.

The second result of this study was the comparison of the 14CSZ to the models produced by USGS, 02CSZ, 02PSH500, 02PSH1000, 14PSH500, and 14PSH1000. Also, as part of these comparisons the 14PSH models were compared to the 02PSH models.

3.3.2 Comparison of 14CSZ to other Models

The comparisons made were, 14CSZ vs. 02CSZ (Figure D.4, Figure D.5, and Figure D.6), 14CSZ vs. 02PSH1000 (Figure D.7, Figure D.8, and Figure D.9), 14CSZ vs. 02PSH500 (Figure D.10, Figure D.11, and Figure D.12), 14CSZ vs. 14PSH1000 (Figure D.13, Figure D.14, and Figure D.15), 14CSZ vs. 14PSH500 (Figure D.16, Figure D.17, and Figure D.18), 14PSH1000 vs. 02PSH1000 (Figure D.19, Figure D.20, and Figure D.21), and 14PSH500 vs. 02PSH500 (Figure D.22, Figure D.23, and Figure D.24). For all of the comparisons, ratios were calculated for the PGA, 0.2s, and 1.0s accelerations. In order to compare the 14CSZ model to the USGS models, ratios were calculated by dividing the 14CSZ model acceleration value for a grid point by the value produced by the alternate model for the same grid point as illustrated in Equation (3.1). Therefore, ratios greater than one mean the 14CSZ model provides a larger acceleration value for that grid point and ratios less than one mean the alternate model provides a larger value.

$$Ratio_{14CSZ} \tag{3.1}$$

For the comparison of the 14PSH models to the 02PSH models the acceleration value produced by the 14PSH model was divided by the value produced by the 02PSH model.

The ratio values were displayed as color contours overlaid on a map of Oregon. The color scheme used was red, white, and gray. Red colors indicated a ratio greater than one and gray colors indicated a ratio less than one. White indicated a ratio of one. Darkening red or gray colors indicated that the ratio was moving further from one. The ratio values for the contours were marked on the maps.

3.3.3 Interpretation of Model Comparison

There was significant variance in the size of the ratios generated by the different model comparisons. In general, the comparison of 14CSZ to the PSH500 models produced the greatest ratios with a maximum ratio of 2.50 observed, while the comparison of 14CSZ to the PSH1000 models produced the smallest ratios with a maximum of 1.18. In the comparison between 14CSZ and 02CSZ the maximum ration observed was 1.48. In the comparison between the 14PSH1000 and 02PSH1000 models the maximum ratio was 1.65, and in the comparison between the 14PSH500 and 02PSH500 models the maximum ratio was 1.5. All of the model comparisons produced ratios less than one as well. The trend found when comparing 14CSZ against all the other models was for the ratios greater than one to be located in a band running the length of the Oregon coast, and the ratios less than one to be located east and west of this band. The location of the band of greater ratios roughly corresponded to the location of the CSZ fault. The trend for the comparison between the 14PSH and 02PSH models was for the greatest ratios to be located around the southwest corner of Oregon.

3.4 SUMMARY

This task presented a developed model, the 14CSZ, that calculates the spectral accelerations caused by a full rupture M9 CSZ earthquake and compare the data from the model to similar data produced by the USGS uniform hazard. Acceleration values for PGA, 0.2s, and 1.0s were generated by the 14CSZ model for a longitude-latitude grid covering Oregon and vicinity. These values were displayed as color contours overlaid over maps of Oregon. Furthermore, ratio comparisons were made between the 14CSZ model, the PSH models, and the 02CSZ model produced by the USGS. The outcome of these comparisons was a set of color contour maps that depicted the ratios over Oregon. Finally, the 14PSH models were compared to the 02PSH models, the outcome of which was also a set of color contour maps.

In the comparisons of the 14CSZ model against models produced by USGS for a 500 year earthquake, the ratio values produced were greater than or close to one for the region of Oregon between just west of the Oregon coast and just east of the longitude of Portland. The exact region fluctuated between the different model comparisons, but the general trend persisted. This meant that the 14CSZ model calculated approximately the same or greater acceleration values for that region. Moreover, for the areas not in this region the ratio values were less than or close to one, which meant that the acceleration values calculated by the other models were greater. In the comparison of the 14CSZ model to the USGS models for a 1000 year earthquake the ratio values were almost entirely less than 1 for the entire state of Oregon

4.0 SEISMIC PERFORMANCE OF CIRCULAR RC BRIDGE COLUMNS

4.1 GENERAL

The following sections describe the dynamic performance of cantilever reinforced concrete bridge columns subjected to dynamic shake table loading. The development of the inertial loading system, hereinafter referred as mass rig, is also presented. This unique system allows controlled shake table testing of single degree-of-freedom models. The large-scale specimens had a height of 96 inches and consisted of a circular cross section of 18 inches diameter. A constant axial load was applied at the top of the columns. Column instrumentation is also discussed, along with the loading protocol used in this study.

The test program was designed to model the behavior of a large-scale reinforced concrete bridge column, measure local and global response quantities, and provide experimental evidence of damage difference under longer duration shaking expected from CSZ event. The following sections summarize the aspects of the research program including specimen details, loading, and instrumentation.

4.2 EXPERIMENTAL PROGRAM

4.2.1 General Description

The experimental program consisted of six test specimens intended to represent scale models of typical circular RC bridge column. The scale of the specimens was based on the capacity of the laboratory and shake table system. The variables in the testing program were the duration of the motion, location of the lap splice and its respective length. The performance of these specimens was intended to reveal vulnerabilities in typical bridge column configurations under long duration earthquakes, expected from Cascadia subduction zone event.

4.2.2 Assessment of Representative Column

In 2015, Bazaez tested a half-scale reinforced concrete bent of a representative bridge, illustrated in Figure 4.4. Based on the results of his research and laboratory constraints, it was decided to use the same column cross-section and material properties but to be tested dynamically in a cantilever configuration. Table 4.1 lists the section and material properties of the column model tested by Bazaez *(Bazaez 2015)*.

Table 4.1: Geometry, reinforcement and material properties for the specimen

Column Diameter (in)	Longitudinal Reinforcement	Transverse Reinforcement	f'_c (psi)	f'_{ce} (psi)	f_y (ksi)	f_{ye} (ksi)
18	10-#5	Hoop D5 @6”	3300	4290	40	44

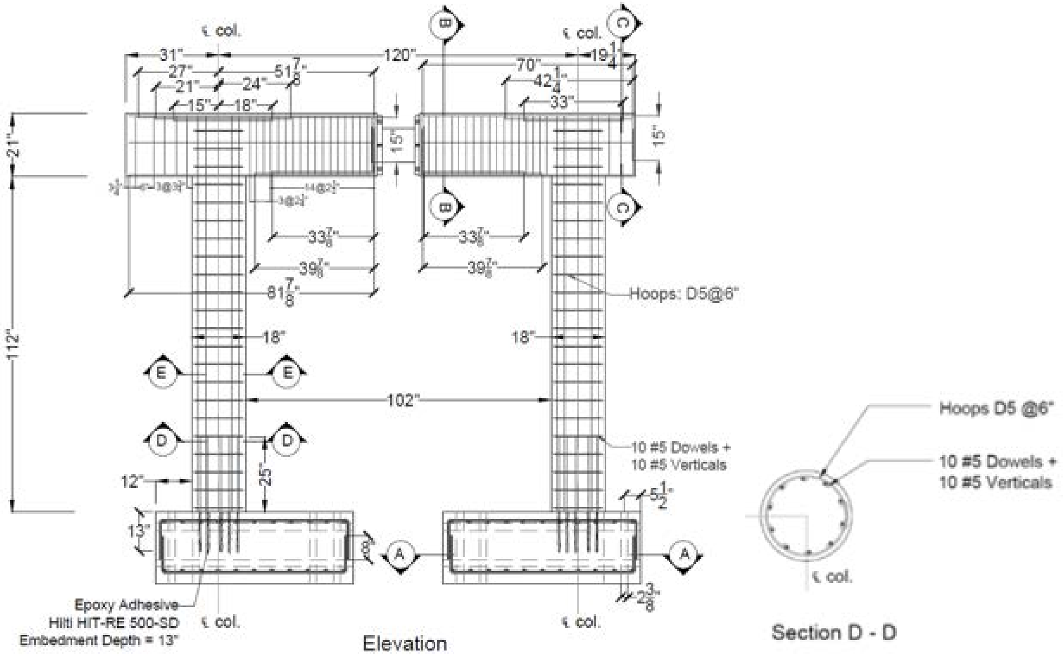

Figure 4.1: Representative RC bridge bent tested by Bazaez *(Bazaez 2015)*

In order to calculate the height of the specimens, a target displacement ductility demand of 4 and a target fundamental period of the column between 0.3 sec to 0.6 sec were first calculated in an iterative process. The column height was varied while the longitudinal steel, material properties, axial load and the cross section dimension were kept constant. The target displacement ductility was defined as the ratio of the displacement demand for a 1000-year event and the idealized effective yield displacement of the column at the formation of the plastic hinge, as per Equation 4.1. The displacement demand was obtained from the representative design response spectrum depicted in Figure 4.2, and calculated using Equation 4.2. This response spectrum corresponds to a 1000-year event (7 percent probability of exceedance in 75 years) and aims to be representative of a vast number of prestressed concrete stringer/girder bridges in Oregon. Further, the displacements were magnified through the use of the displacement magnification factor for short period structures, Rd as per AASHTO *(AASHTO 2009)*, and presented in Equation 4.3.

$$\mu_D{}^{col} = \frac{\Delta_{D,1000}}{\Delta_y^{col}} = \frac{\Delta_{D,1000}}{\frac{H^2}{3} \cdot \phi_y} \tag{4.1}$$

$$\Delta_{D,1000} = R_d \cdot \frac{S_{a,1000} \cdot T_{n,crack}{}^2 \cdot g}{4\pi^2} \tag{4.2}$$

$$R_d = \begin{cases} \left(1 - \frac{1}{\mu_D}\right)\frac{1.25T_s}{T_e} + \frac{1}{\mu_D} \geq 1.0 \quad for \quad \frac{1.25T_s}{T_e} > 1.0 \\ 1.0 \quad for \quad \frac{1.25T_s}{T_e} \leq 1.0 \end{cases} \tag{4.3}$$

Where, $T_{n,crack}$ is the fundamental period of the SDOF system; $S_{a,1000}$ is the spectral acceleration given by the 1000-year event response spectrum; g is the standard gravity constant; H is the distance from the point of maximum moment to the point of contra-flexure, and equal to the column height for a cantilever column; ϕ_y is the idealized yield curvature defined by an elasto-plastic representation of the cross-section M-ϕ curve; T_s is the period at the end of constant design spectral acceleration plateau and μ_D is the maximum local member displacement ductility demand. AASHTO *(AASHTO 2009)* states that μ_D may be taken as 6.

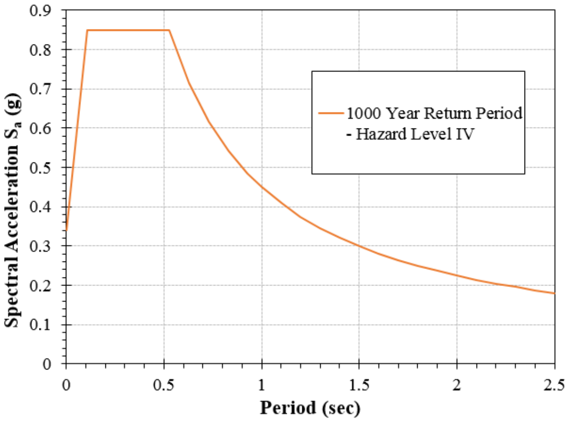

Figure 4.2: Representative response spectrum

The M-ϕ analysis was performed using the expected material properties, i.e., a concrete compressive strength of 4290 psi and a steel yield stress of 44 ksi. The axial load was assumed to be 10% of the column axial capacity ($0.10f'_cA_g$). Idealized yield curvature ϕ_y and cracked moment of inertia were then obtained.

The fundamental period of the column was calculated using Equation 4.4, where a seismic weight of 40 kips was considered.

Finally, based on the results shown in Figure 4.3 and due to laboratory height limitations, a column height of 8 ft was chosen. For this value, a displacement ductility demand of 4 and a fundamental period of 0.4 sec are obtained.

$$T_{n\_crack} = \frac{W \cdot 2 \cdot \pi}{3 \cdot 57{,}000 \cdot \sqrt{f'_{ce}} \cdot I_{crack} \cdot g} \cdot H^3 \tag{4.4}$$

Where, W is the seismic weight of the SDOF system; f'_{ce} is the expected concrete compressive strength; and I_{crack} is the cracked moment of inertia.

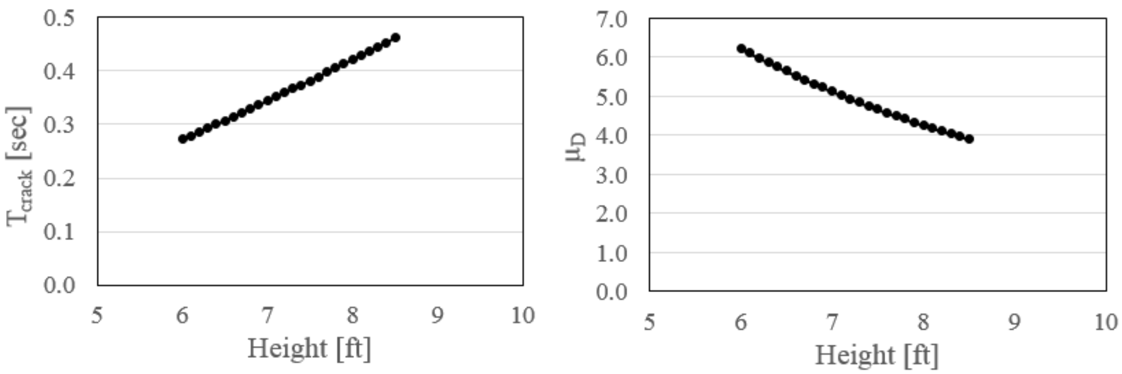

Figure 4.3: Parametric study of column height

4.2.3 Specimens Details

Three sets of circular RC bridge column were constructed and tested at iStar Laboratory at Portland State University. Two critical design parameters in these columns were the location and length of the lap-spliced longitudinal starter bars in the footing. Specimens 1 through 3 had the lap-splice outside the expected plastic hinge zone. Specimens 4 through 6 had the lap-splice inside the expected plastic hinge zone, in an effort to represent typical Oregon Bridge columns constructed in the 1950s to mid-1970s. Specimens 4 and 5 had lap-splice length of 16 inches, which corresponds to 25 times the diameter of the longitudinal steel reinforcement ($25d_b$). Specimens 6 had lap-splice length of 25 inches, which corresponds to 40 times the diameter of the longitudinal steel reinforcement ($40d_b$). The final details selected for construction are shown in Figure 4.4.

The column longitudinal reinforcement used in each specimen consisted of 10 #5 bars equally spaced. The transverse reinforcement was deformed wire D5 spaced at 6 inches center to center. The longitudinal reinforcing steel used to construct the test specimens consisted of Grade 40 deformed bar conforming to the American Society of Testing and Materials (ASTM) designation A615. On the contrary, the transverse steel consisted of deformed wire conforming the ASTM designation A496.

Normal weight concrete was used to construct the test specimens with a target 28-day strength of 3300 psi. A concrete cover of 1 inch was used for all the columns. Standard compression testing of 6-inch by 12-inch concrete cylinders was performed at 7-day, 28 days and at the day of test completion. The average of the concrete cylinder tests are shown in Table 4.2 and Table 4.3.

Table 4.2: Concrete compressive strengths Specimens 1 through 3

Concrete Pour	Compressive Strength (f'_c) psi
7-day	3233
28-day	4386
Specimen 1 (test day)	4734
Specimen 2 (test day)	4929
Specimen 3 (test day)	5102

Table 4.3: Concrete compressive strengths Specimens 4 through 6

Concrete Pour	Compressive Strength (f'_c) psi
7-day	3023
Specimen 4 (test day at 28-day)	4270
Specimen 5 (test day)	4352
Specimen 6 (test day)	4798

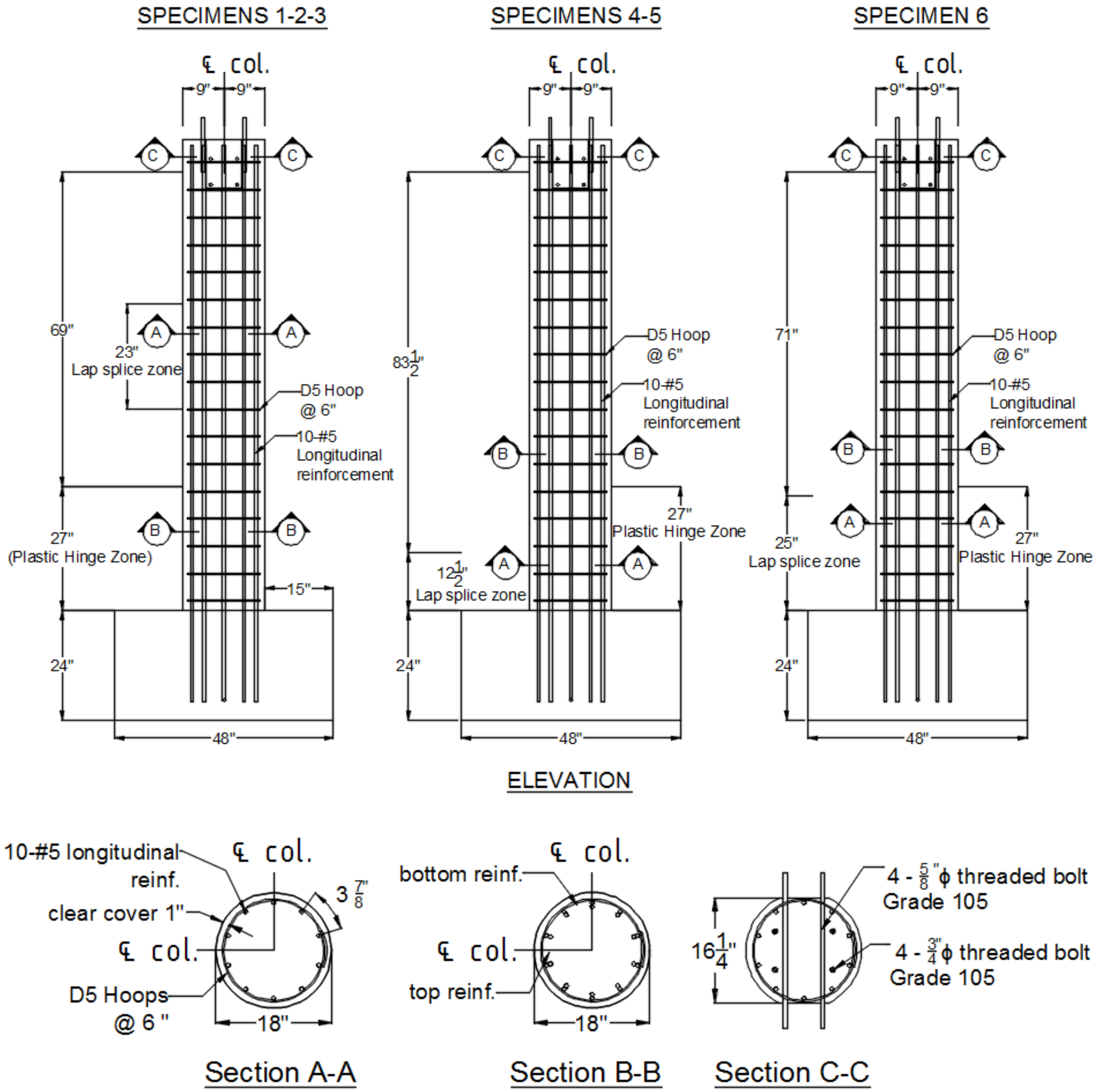

Figure 4.4: Geometry and reinforcement of RC Bridge column specimens

4.2.4 Mass-Rig System

Shake table tests requires inertial loads in order to study the dynamic effects on the performance of specimens. Different configurations of mass-rig systems have been utilized in shake table testing. Some shake table tests consider the additional mass placed directly on the top of the specimens to be tested, but has the disadvantage of the high-risk in operation for attaining performance levels near collapse and do not reproduce with exactitude the response of a particular prototype. Other tests configuration considers the use of external devices for transmitting the inertial loads to the specimen, but the loading and overall stiffness of the system are affected through the P-delta effect. To overcome the drawbacks of these configurations, a new mass-rig system was developed for this study, as shown in Figure 4.5. The mass rig consists of a steel column pin-connected to the shake table. To provide the inertial mass, a predefined quantity of concrete blocks is then attached to the column at the required height via high strength post-tension rods. An external steel frame was included to prevent damage to the shake table system if the collapse of specimen and mass occur. During column failure, the mass rig will translate until the distance between the bottom face of concrete blocks and the longitudinal beams is zero. To preclude out-of-plane motion, a caster was attached to the web of each longitudinal beam (Figure 4.6). The mass-rig is linked to the top of the specimen utilizing a pinned end rigid link, allowing free rotations. To ensure that the concrete blocks remain joined, and the inertial forces are being transmitted through the rigid link while shaking, a steel beam was added at the back of the concrete blocks.

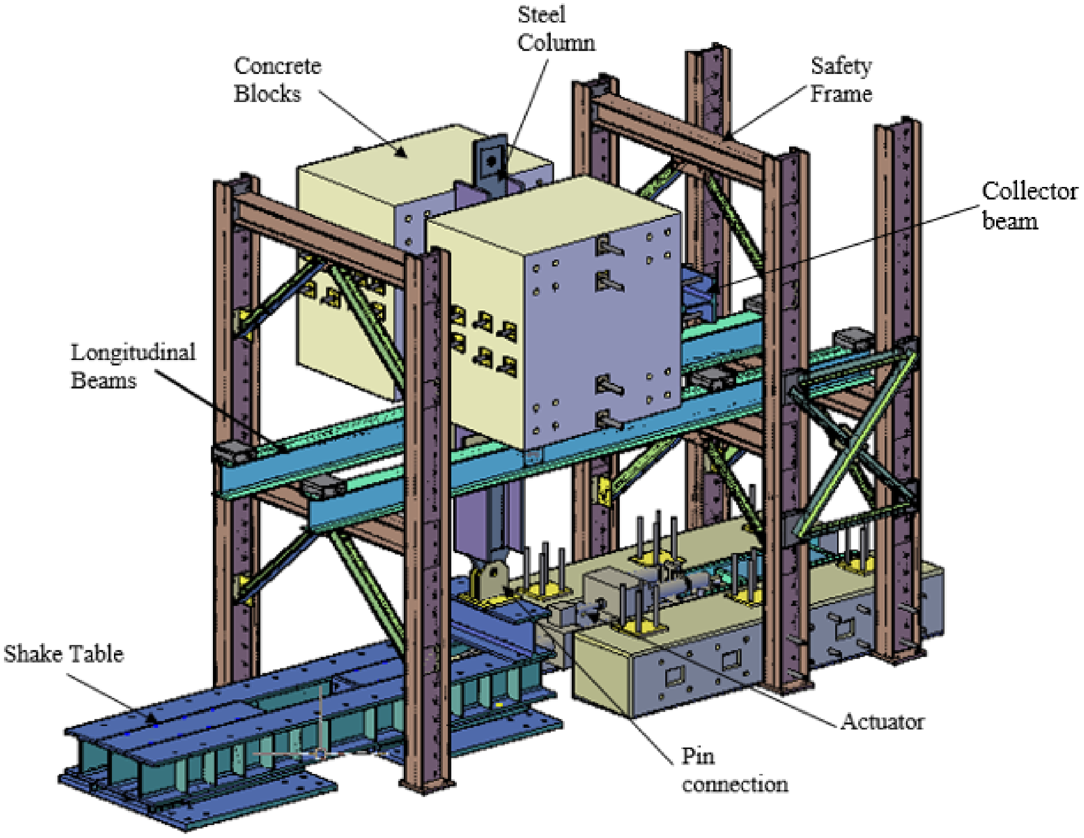

Figure 4.5: 3-D schematic of the Mass Rig system

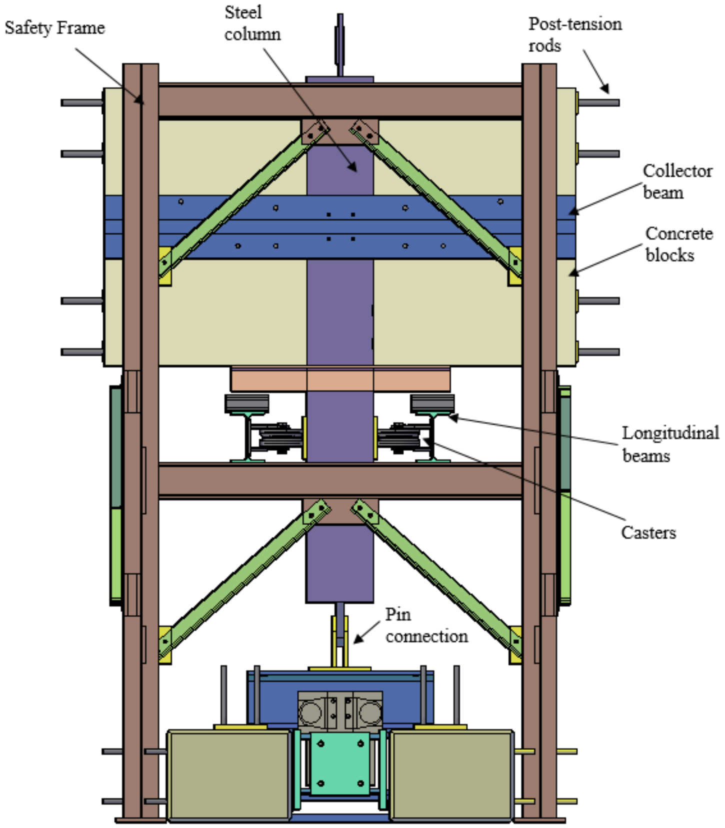

Figure 4.6: South view of Mass Rig system

4.2.5 Overall Test Configuration and Instrumentation

The test setup included a cantilever RC column, footing, mass-rig, and shake table system. A schematic representation of the experimental test setup is shown in Figure 4.7; meanwhile the actual test setup is illustrated in Figure 4.8. Four concrete blocks weighing a total of 37.7 kips were used on the mass rig. The steel and RC columns also provides a small portion of the inertial mass, as does the swiveled link system, column axial load system, and steel beam. Therefore, a total lateral effective weight (inertia mass) of 41.93 kips was used.

The footing of each specimen was secured to the shake table with high strength 1" post-tensioning rods to prevent decompression under maximum overturning moment and provide shear transfer without sliding. To measure the lateral force due to the inertial force, the pinned end rigid link was instrumented with a 50 kip MTS 661 Series High Capacity Force Transducer which was connected to the data acquisition system.

Axial load indexes typically vary between 5% to 25% for bridge columns. Particularly in this study and due to laboratory capabilities, 9% of the column axial capacity ($0.09f'_cA_g$) was used. This load was applied through two high-strength rods and two Power Team RH606 60 tons center-hole hydraulic rams attached to a steel spreader beam bolted to embedded 7/8" all-thread rods at the top of the column. The hydraulic rams were connected to a Hydac 3000 psi accumulator to minimize the axial load fluctuations. To monitor the axial load, two load cells between the rams and the spreader beam were used. The actual axial load system is shown in Figure 4.9.

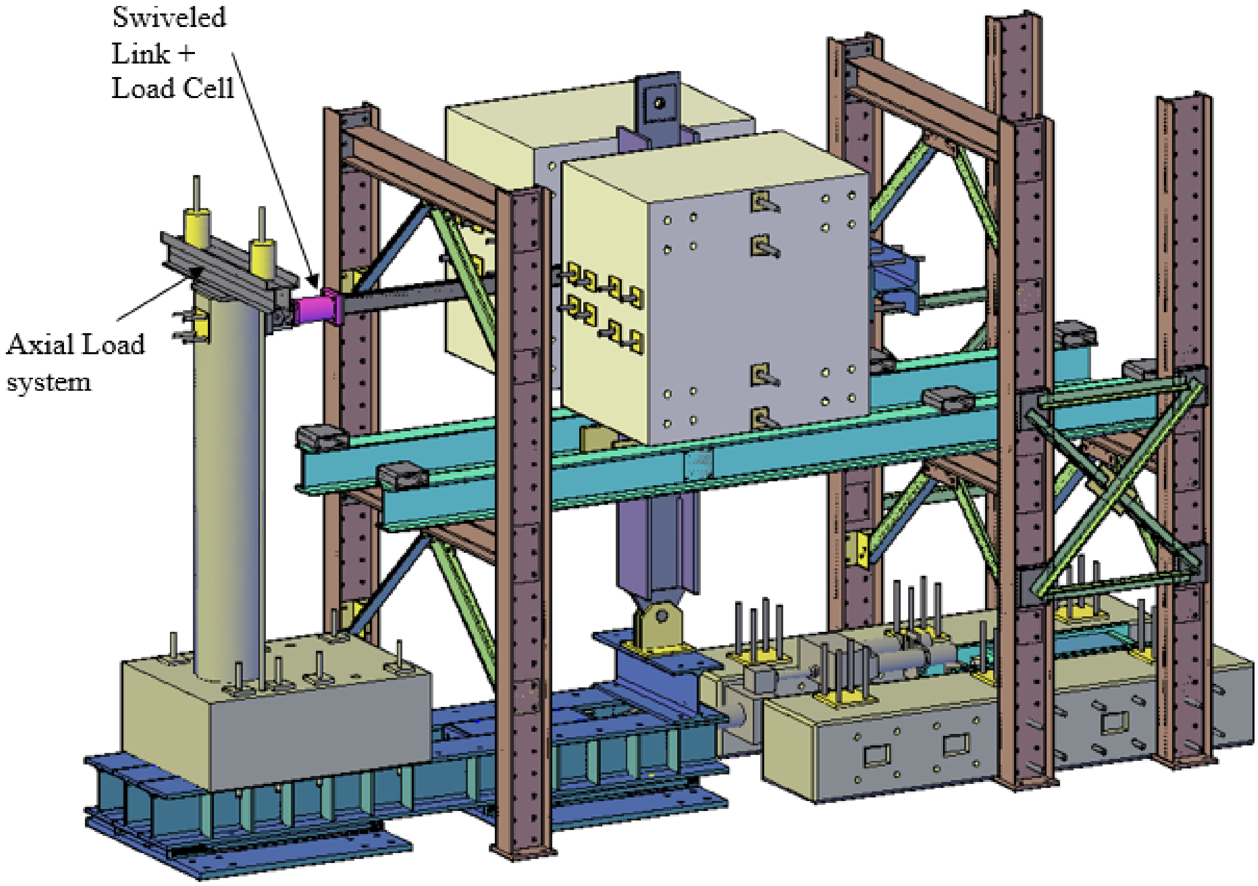

Figure 4.7: Schematic of test setup configuration

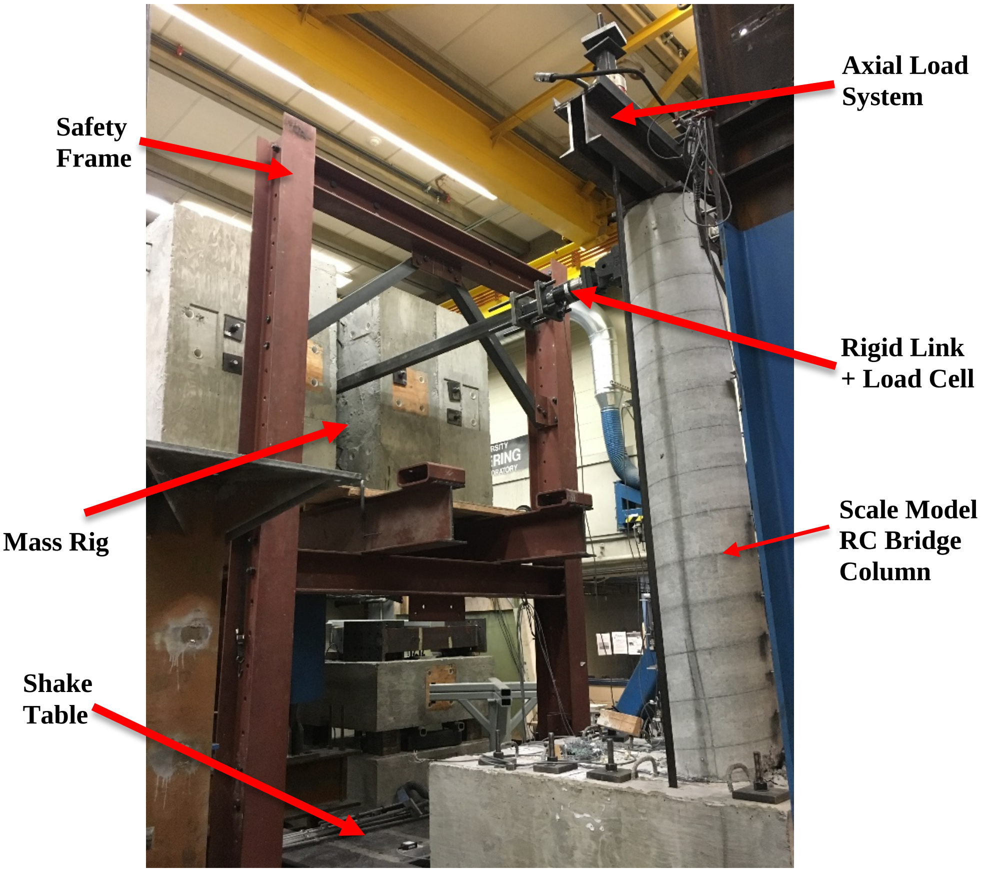

Figure 4.8: Actual Test setup

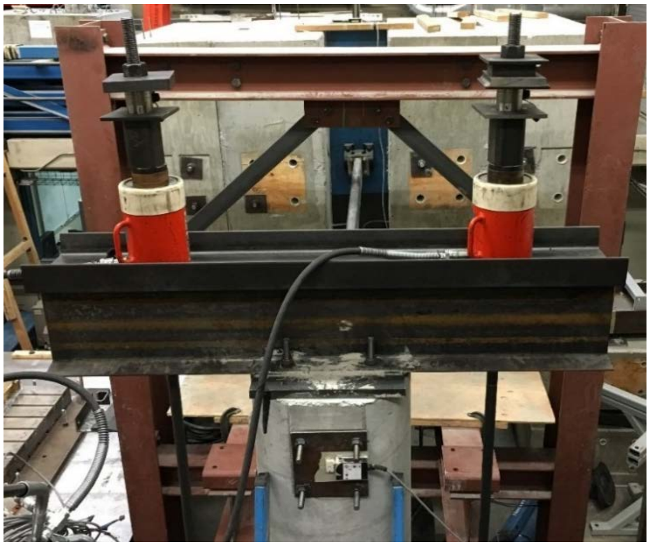

Figure 4.9: Axial load system

To analyze the behavior of the specimens subjected to dynamic loading, the columns were fully instrumented via strain gages and linear variable displacement transducers (LVDTs) as shown in Figure 4.10 and Figure 4.12, respectively. Strain gauges were used to measure the strain at specific points in the specimens. For Column 1 through Column 3, a total of twenty-one strain gauges were installed. Twenty strain gauges in the longitudinal bars of the columns, and one in the transverse reinforcement of the columns. For Column 4 through Column 6, a total of twenty-nine strain gauges were mounted. Eight strain gauges in the dowels embedded in the footings, eight in the column dowels, twelve in the longitudinal reinforcement of the columns, and one in the transverse reinforcement of the columns. All strain gauges were placed at expected plastic hinge zones of columns. Installation of all strain gages was performed before the placement of the concrete as shown in Figure 4.11. LVDTs were used to measure curvature in the plastic hinge zone.

String potentiometers were used to measure in-plane and out-of-plane column deflections. A table LDVT internal to the table actuator was used to measure the table displacement response. Thereby, top column deflection relative to the shake table was obtained by subtracting shake table displacement from measured top column displacement. Four accelerometers were installed at different locations on the setup: top of the column, top of the masses, top of the footing, and shake table.

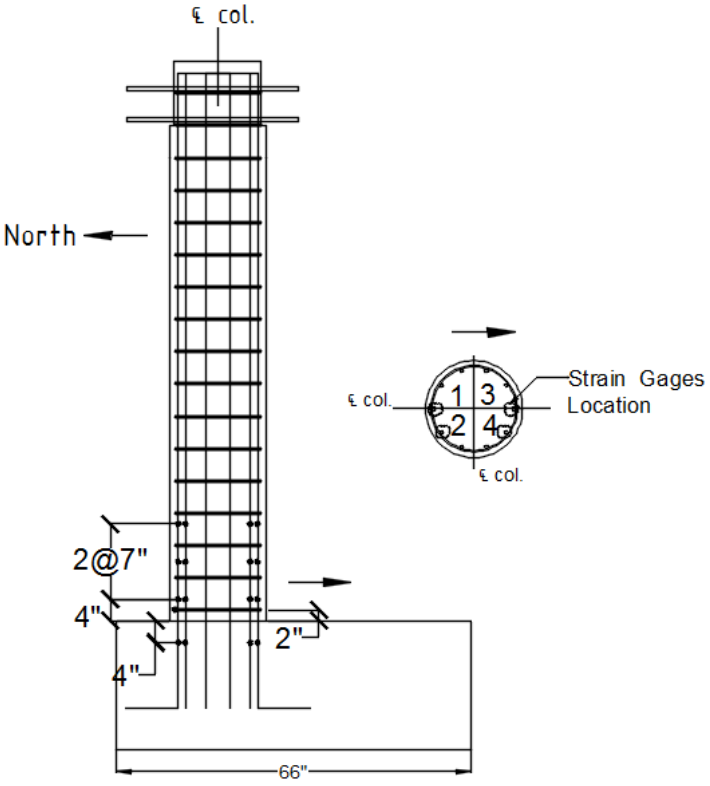

Figure 4.10: Location of strain gauges

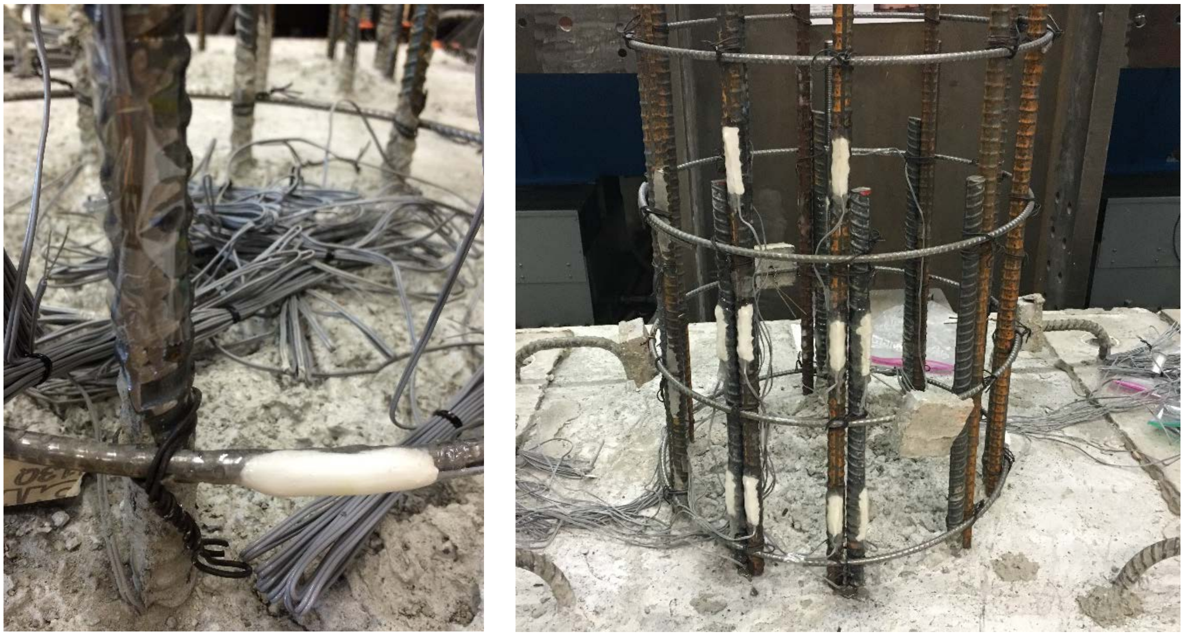

(a) (b)

Figure 4.11: Installation of strain gauges. (a)Strain gauges on longitudinal reinforcement and hoop for specimens 1 through 3, (b) Strain gauges with protective coating on longitudinal reinforcement and dowel for specimens 4 through 6

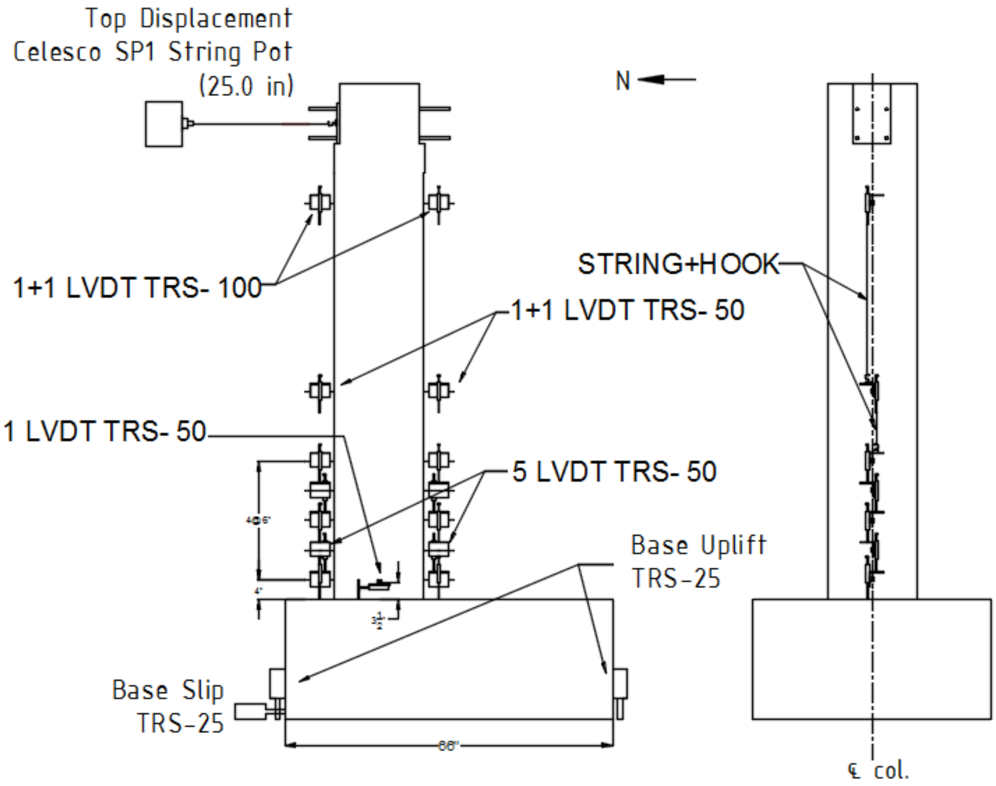

Figure 4.12: Location of LDVTs

4.2.6 Earthquake Selection

Three earthquake motions were considered as the input for the shake table tests and selected from subduction and crustal earthquake sets. The earthquake motions were the 1989 Loma Prieta earthquake, the 2010 Maule earthquake, and the 2011 Tohoku earthquake. The criteria used to select these earthquake motions was based on the duration of the motion and the number of inelastic cycles of pre-peak excursions for short period structures, i.e. T = 0.5 sec, imposed by the seismic excitations*(Bazaez et al. 2015)*. Table 4.4 lists the earthquakes motions used in this study.

Each record was then scaled to achieve a target displacement ductility. The scale factors for each motion were obtained from nonlinear time-history analyses of the column using OpenSees *(OpenSees 2011)*. Table 4.5 summarize the scale factors used on each motion.

The experimental research study was developed to investigate the effect ground motion duration and steel lap splice location on the seismic behavior of RC bridge columns. Thus, different loading patterns were developed for each column depending on the location of the lap splice. Column 1 through Column 3, which had the lap splice outside the expected plastic hinge, were subjected to a crustal and two different subduction zone earthquakes, respectively. For the second test series, which had the lap splice inside the expected plastic hinge, a crustal and one subduction zone earthquake were used. Based on the results of the first test series, the 2010 Maule subduction zone earthquake was chosen. Intermittent free vibration tests and low level random motions were conducted to measure the change in frequency and damping ratio of the columns.

Table 4.4: Ground motions used for testing

Set	Station	Component	N.I.C (Pre-peaks)	PGA (g)	Duration (sec)
Loma Prieta (Crustal)	Capitola	Horizontal (X)	12	0.53	39.95
Maule (Subduction)	Curico	Horizontal (X)	36	0.41	180
Tohoku2 (Subduction)	Iwaki	Horizontal (Y)	39	0.39	299.99

Table 4.5: Ground motion scale factors

Test	Record	Scale factor	Target displacement ductility	Expected Failure
Column 1	Capitola X	1.00	4	Plastic Hinge
		1.48	6	
		1.75	Failure	
Column 2	Curico X	1.57	4	Plastic Hinge
		1.68	6	
		1.74	Failure	
Column 3	Iwaki Y	1.77	4	Plastic Hinge
		1.92	6	
		2.04	Failure	
Column 4	Capitola X	1.00	4	Lap-splice
		1.48	6	
Column 5	Curico X	1.57	4	Lap-splice
Column 6	Curico X	1.57	4	Lap-splice

4.2.7 Experimental Results

This section describes the observed results from the experimental study of six circular RC columns using shake table tests. The observed performance and measured response of the specimens for all motions are described in this section. Table response acceleration and its respective response spectra, force-deformation hysteresis, strain profiles for longitudinal reinforcement, and column curvatures are also plotted for all motions.

4.2.7.1 Column 1

The test loading sequence applied to this specimen is listed in Table 4.6. A constant axial load of -75 kips (9% of the column axial capacity) was applied to the specimen. It is worth noting that a reduction of 6.7% in the applied axial load was done before the last motion, as denoted in Table 4.6. Target axial load for last test was then -70 kips.

Before and after each motion, a free vibration test, as well as a low level random motion, were performed to obtain the dynamic properties of the specimen, such as natural period, damping and stiffness. From the performed free vibration test, natural period and damping of the specimen were calculated. A Matlab script was written to compute the Fourier spectrum and obtain the predominate frequencies of each motion. The damping ratio ξ was calculated using the decrement logarithmic method *(Chopra 2001),* according to following equation:

$$\ln\frac{u_i}{u_{i+j}} = \frac{2\cdot\pi\cdot\xi}{\sqrt{1-\xi^2}} \qquad \textbf{(4.5)}$$

Where, u_i and u_{i+j} are the peak values of displacement, force or acceleration at the first and j^{th} successive cycle, respectively. Table 4.7 shows the dynamic properties for Column 1 measured from the free vibration tests.

Table 4.6: Column 1 test loading protocol

Test	Motion
FV1	Free Vibration
R1	Random
1	1.00 x Capitola X
FV2	Free Vibration
R2	Random
2	1.48 x Capitola X
FV3	Free Vibration
R3	Random
AR	Axial Load Reduction
FV4	Free Vibration
R4	Random
3	1.75 x Capitola X

The low level random motion was used to calculate the natural period and stiffness of the specimen. Natural period was found by using the Matlab script for Fourier Analysis *(MATLAB 8.5 2015*. Then, the following equation was used to calculate the stiffness of the specimen at each motion:

$$K = \frac{4 \cdot \pi^2}{T_n^2} \cdot m \qquad \textbf{(4.6)}$$

Where, m is the inertial mass; and T_n is the natural period of the column. A summary of the calculated stiffness for specimen 1 is shown in Table 4.8.

Table 4.7: Dynamic Properties from Free Vibration tests for Column 1

Event	Motion S.F	Period T_n [sec]	Damping ζ [%]
FV1	1.00	0.35	1.77
FV2	1.48	0.65	3.60
FV3	1.75	0.65	3.68
FV4	1.75	0.67	3.91

Table 4.8: Measured elastic stiffness from low level Random motion for Column 1

Test	Motion SF	Period T_n [sec]	Stiffness [kip/in]
R1	1.00	0.36	32.5
R2	1.48	0.60	11.8
R3	1.75	0.67	9.6
R4	1.75	0.67	9.5

Good agreement for the dynamic properties was found between both tests. As can be seen, as the specimen degraded and the stiffness reduced, the period and the damping of the specimen increased.

Figure 4.13 shows the 1.00 Capitola X ground motion. Figure 4.14 depicts the target and achieved elastic response spectra for a 5% damping ratio. Target and achieved values of table acceleration, velocity and displacement for each scale factor are given in Table E.1. The shake table performed well for all the motions used in this test.

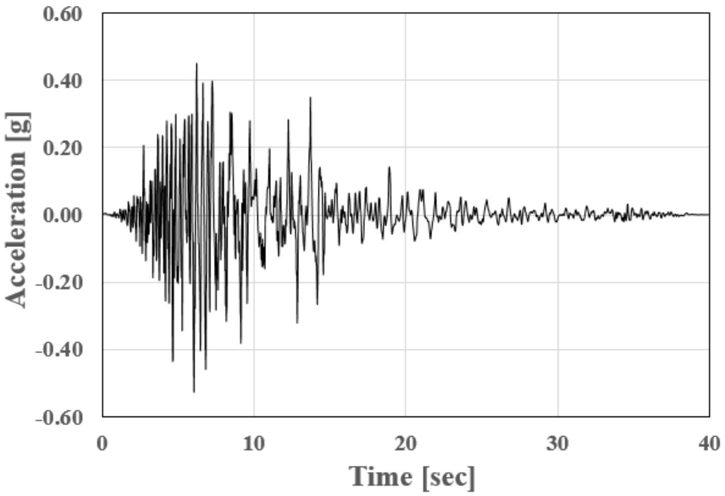

Figure 4.13: Ground acceleration for 1.00 Capitola X

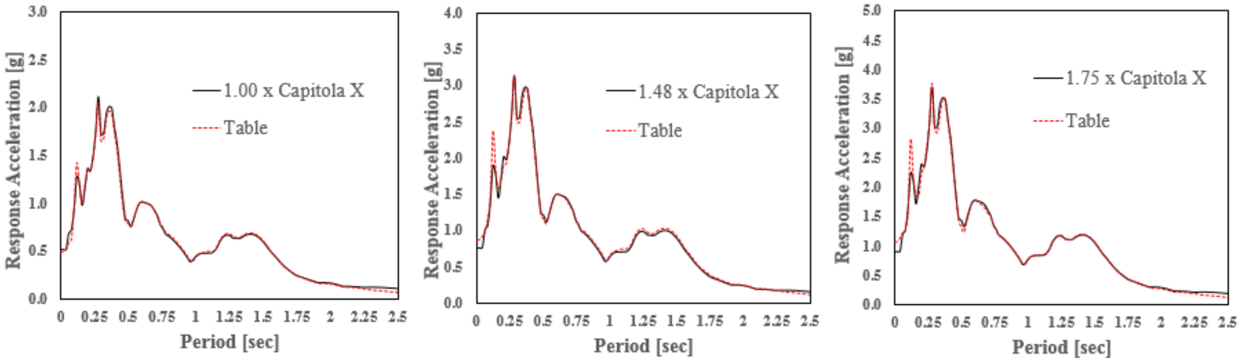

Figure 4.14: Target and achieved elastic response spectra for 5% damping ratio for each motion

Figure 4.15 shows the lateral load vs. displacement hysteresis curve for 1.00 Capitola X. The experimental yield displacement for this specimen was 0.58 inches. This value was obtained from the reading of the strain gauges placed on the column reinforcement and it was defined as the point at which the first rebar reached a strain over the yield strain (ε_{sy} = 1724 µs). The damage consisted of three major horizontal cracks located in the expected plastic hinge zone that gave place to minor spalling of concrete, as shown in Figure 4.17(a). The first crack was located on the north side about 2 inches above the footing, in the first level of transverse reinforcement. The other two cracks were developed all around the column about 8 inches and 14 inches above the footing, at the second and third level of transverse reinforcement, respectively. These two cracks were closed after shaking. Minor spalling up to 4 inch in height occurred at the column base on both north and south side. No out-of-plane deformation was observed.

The hysteretic behavior of this specimen for the first motion showed a moderate to high ductile behavior by reaching a displacement ductility near 5 and 6 in the positive and negative direction, respectively. The peak lateral load was -17 kip and occurred at a lateral displacement of approximately -2.2 inches. After this motion, the specimen did not exhibit a significant decrease in lateral strength.

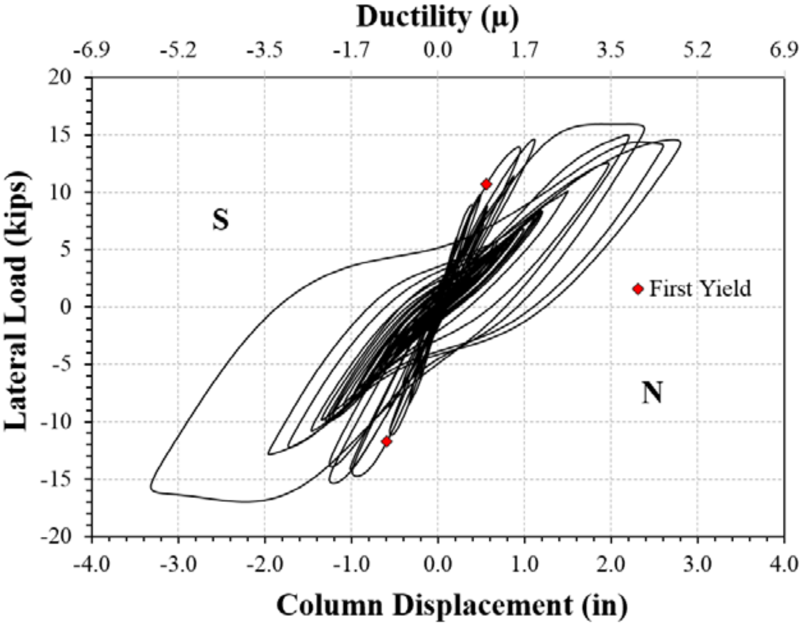

Figure 4.15: Column 1 Load vs. Displacement curve for 1.00 x Capitola X

Following the 1.48 Capitola X ground motion the spalled region increased to a height of 8 inches on the south side, as shown in Figure 4.17(b). Crushing of the concrete at the base of the column was observed on the north and south sides. One level of transverse reinforcement was visible in the hinge region on the south side. No longitudinal bars were visible and a few more cracks were visible at 6 inches above the base of the column. As in the first motion, the damage was fully concentrated in the expected plastic hinge region. No out-of-plane deformation was observed.

Figure 4.16 shows the lateral load vs. displacement hysteresis curve for 1.48 Capitola X. Before this motion, the column period has moved beyond the higher energy portion of the spectrum due to the stiffness degradation. The hysteretic behavior for this motion showed a high ductile behavior by reaching a displacement ductility slightly over 7 in both directions. The peak lateral load was -16 kip and occurred at a lateral displacement of approximately -3.3 inches. After this motion, the specimen did not exhibit a significant decrease in lateral strength.

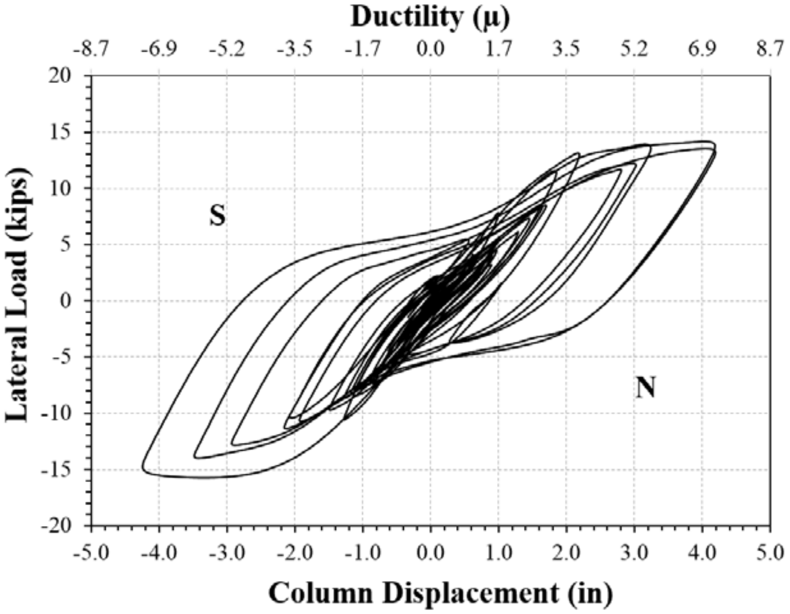

Figure 4.16: Column 1 Load vs. Displacement curve for 1.48 x Capitola X

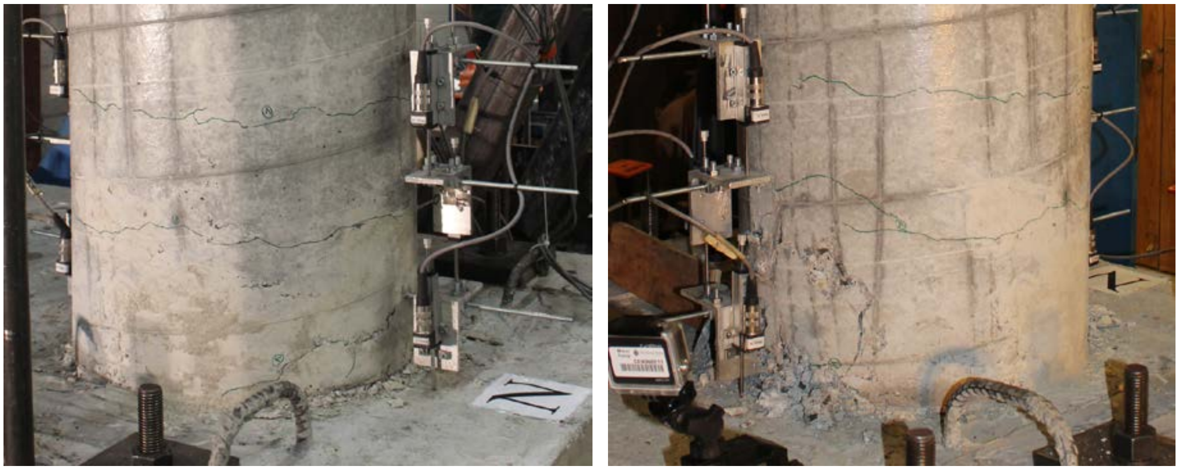

(a) (b)

Figure 4.17: Damage in Column 1. (a)Horizontal cracks and spalling of concrete for 1.00 Capitola X, (b) Crushing of concrete for 1.48 Capitola X

The 1.75 Capitola X motion caused the complete collapse of the column. During testing, the specimen started rocking at a height of 8 inches due to the loss on effectiveness of the second level of transverse reinforcement. The ultimate mode of failure was crushing of concrete and longitudinal bar buckling at the bottom of the column in the plastic hinge zone, as shown in Figure 4.19. The longitudinal bars buckled over an approximate length of 12 inches. This length corresponds to 2 times the spacing of the transverse reinforcement. Lateral instability caused the column to deflect close to the mass rig system maximum limit.

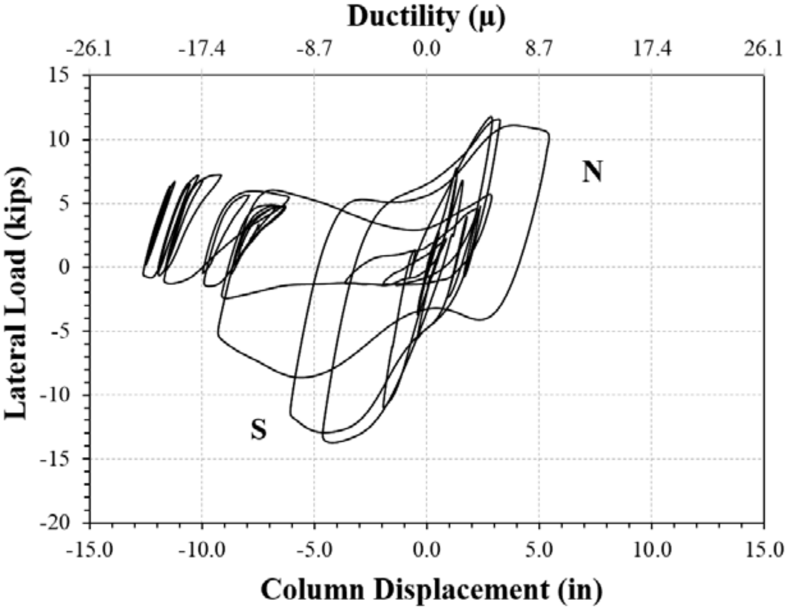

Figure 4.18: Column 1 Load vs. Displacement curve for 1.75xCapitola X

The final response for 1.75 Capitola X is shown in Figure 4.18. The peak lateral load was -14 kip and occurred at a lateral displacement of approximately -4.2 inches.

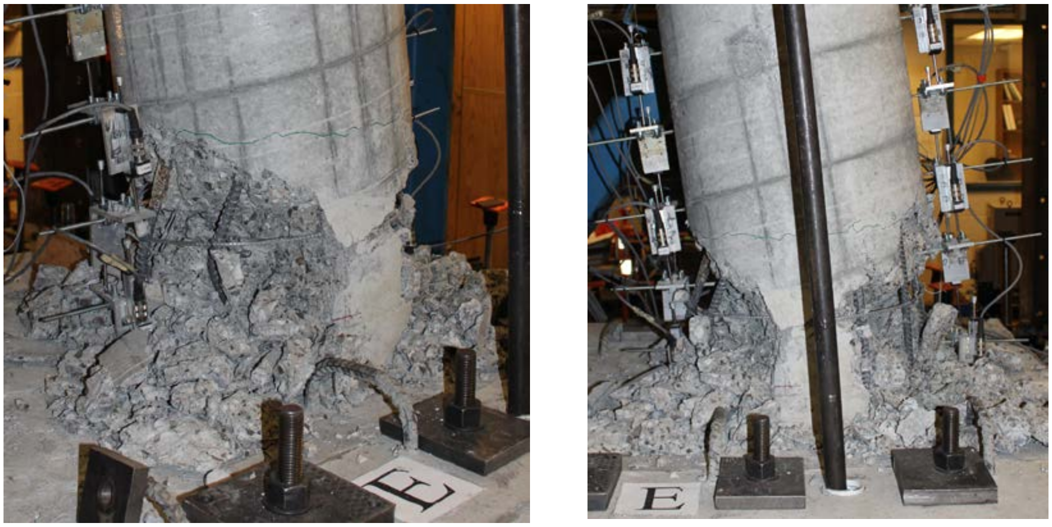

(a) (b)

Figure 4.19: Damage in Column 1 for 1.75 Capitola X. (a) Bar buckling, (b) Lateral Instability

Based on the experimental results, Column 1 showed a hysteresis response typical of flexural behavior. Measured values for peak top column displacement, ductility and drift are summarized in Table 4.9. Note that the values for the peak lateral force did not occur at the peak top column displacement.

Table 4.9: Measured performance for Column 1

Event	Motion S.F	Peak Δ [in]	Peak μ_Δ (Δ_y = 0.58 in.)	Peak Drift Ratio [%]	Peak Lateral Force [kip]	Peak Moment [kip-in]
1	1.00	3.32	5.8	3.5	17.0	1630.8
2	1.48	4.24	7.4	4.4	15.7	1510.4
3	1.75	9.3	16.1	9.7	13.7	1319.0

4.2.7.2 Column 2

The test loading sequence applied to this specimen is listed in Table 4.10. A constant axial load of -75 kips (9% of the column axial capacity) was applied to the specimen. It is worth noting that a reduction of 6.7% in the applied axial load was done before the last motion, as denoted in Table 4.10. Target axial load for last test was then -70 kips.

Table 4.10: Column 2 test loading protocol

Test	Motion
FV1	Free Vibration
R1	Random
1	1.57 x Curico X
FV2	Free Vibration
R2	Random
2	1.68 x Curico X
FV3	Free Vibration
R3	Random
AR	Axial Load Reduction
FV4	Free Vibration
R4	Random
3	1.74 x Curico X
FV5	Free Vibration
R5	Random

As in Column 1, a free vibration test, as well as a low level random motion were performed before and after each motion, in order to obtain the dynamic properties of the specimen. From the performed free vibration test, natural period and damping of the specimen were calculated. The natural period was obtained performing a Fourier analysis of the column free vibration response. The damping ratio ξ was calculated using Equation

$$\ln\frac{u_i}{u_{i+j}} = \frac{2\cdot\pi\cdot\xi}{\sqrt{1-\xi^2}} \qquad \textbf{(4.5)}.$$

Table 4.11 shows the dynamic properties for Column 2 measured from the free vibration tests.

Table 4.11: Dynamic Properties from Free Vibration tests for Column 2

Test	**Motion S.F**	**Period T_n [sec]**	**Damping ζ [%]**
FV1	1.57	0.35	1.89
FV2	1.68	0.58	2.66
FV3	1.74	0.60	3.39
FV4	1.74	0.63	4.44
FV5	-	0.90	6.16

From the low level random motion, natural period was obtained using Fourier analysis, whereas the stiffness of the specimen was calculated using Equation 4.6.

$$K = \frac{4\cdot\pi^2}{T_n^2}\cdot m \qquad \textbf{(4.6)}.$$

A summary of the calculated stiffness for specimen 2 is shown in Table 4.12.

Table 4.12: Measured elastic stiffness from low level Random motion for Column 2

Test	**Motion SF**	**Period T_n [sec]**	**Stiffness [kip/in]**
R1	1.57	0.37	32.5
R2	1.68	0.57	13.2
R3	1.74	0.59	12.3
R4	1.74	0.63	10.8
R5	-	0.83	6.2

Good agreement for the dynamic properties was found between both tests. As expected from the results of Column 1, as the specimen degraded and the stiffness reduced, the period and the damping of the specimen increased.

Figure 4.20 shows the 1.00 Curico X ground motion. Figure 4.21 depicts the target and achieved elastic response spectra for a 5% damping ratio. Target and achieved values of table acceleration, velocity and displacement for each scale factor are given in Table E- 2. The shake table performed well for all the motions used in this test.

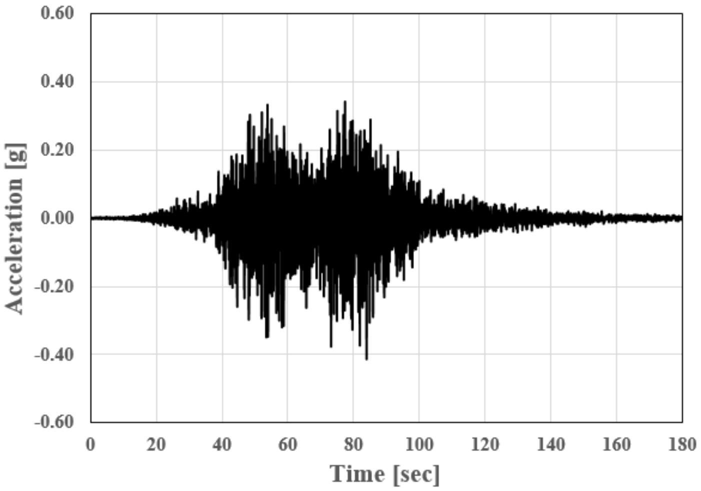

Figure 4.20: Ground acceleration for 1.00 Curico X

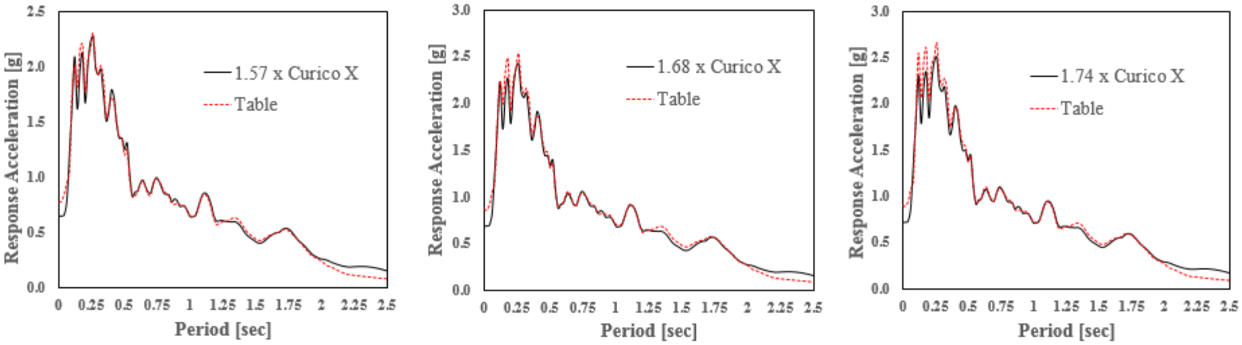

Figure 4.21: Target and achieved elastic response spectra for 5% damping ratio for each motion

Figure 4.22 shows the lateral load vs. displacement hysteresis curve for 1.57 Curico X. The experimental yield displacement for this specimen was 0.65 inches. This value was obtained from the reading of the strain gauges placed on the column reinforcement and it was defined as the point at which the first rebar reached a strain over the yield strain (ε_{sy} = 1724 µs). The damage consisted of two major horizontal cracks located in the expected plastic hinge zone, as shown in Figure 4.23(a). Both cracks were closed after shaking and developed all around the column about 8 inches and 14 inches above the footing, at the second and third level of transverse reinforcement, respectively. Some vertical cracks were also noticed at the column base. Considerable spalling in the bottom of the column on the north and south sides was observed after the motion. The spalled region was up to 4 inches in height. First level of transverse reinforcement and one longitudinal rebar were visible on the north side, although no significant core damage had occurred (Figure 4.23(b)). This specimen suffered more damage than specimen 1 for the same target displacement ductility. No out-of-plane deformation was observed.

The hysteretic behavior of this specimen for the first motion showed a high ductile behavior by reaching a displacement ductility near 6 and 5 in the positive and negative direction, respectively. The peak lateral load was 17.5 kip and occurred at a lateral displacement of approximately 2.4 inches. After this motion, there was no significant loss in column strength.

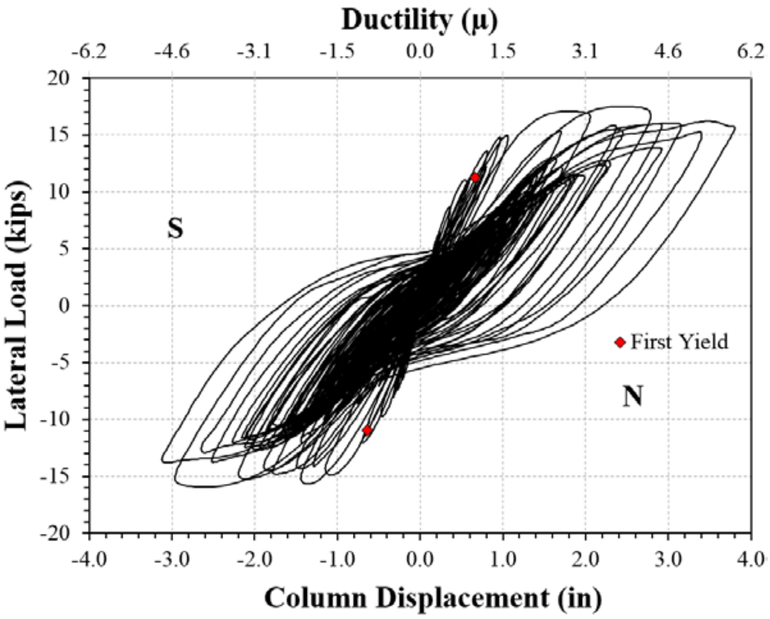

Figure 4.22: Column 2 Load vs. Displacement curve for 1.57 x Curico X

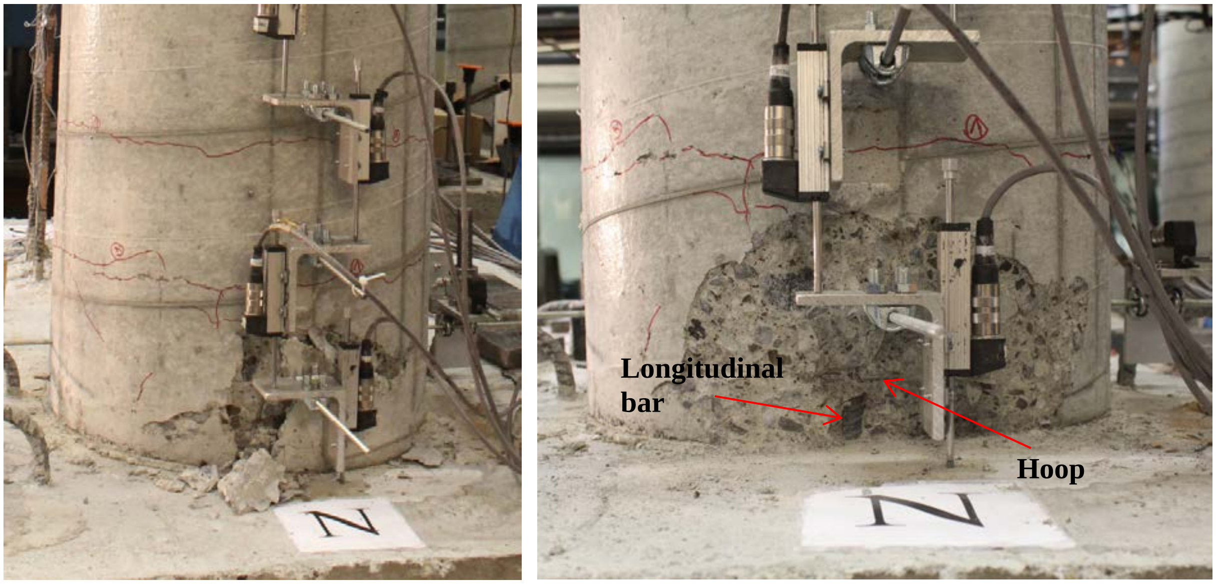

(a) (b)

Figure 4.23: Damage in Column 2 for 1.57 x Curico X. (a) Horizontal cracks and spalling of concrete (b) Hoop and Longitudinal bar visible

Considerable spalling in the bottom of the column to a height of 10 inches on the north side, as well as propagation of horizontal and vertical cracks was observed after 1.68xCurico X (Figure 4.25(a)). Crushing of concrete at the base of the column was observed on the north and south sides. One and two levels of transverse reinforcement were visible in the hinge region on the south and north side, respectively. Three longitudinal bars were visible with core damage beginning to extend beyond the longitudinal bars. Buckling of these three longitudinal bars occurred, one on the south side and two on the north side. The extreme bar on the south side buckled across a distance of 2 inches, starting above the footing surface, as shown in Figure 4.25(b). The bars on the north side buckled across a distance of 6 inches, starting at 2 inches above the footing surface, as shown in Figure 4.25(c). Two failure modes occurred during this motion; crushing of concrete and longitudinal bar buckling. No out-of-plane deformation was observed.

Figure 4.24 shows the lateral load vs. displacement hysteresis curve for 1.68xCurico X. The hysteretic behavior for this motion showed a high ductile behavior by reaching a displacement ductility close to 7 and 6 in the positive and negative direction, respectively. Specimen exhibited a reduction in its lateral strength of about 18% with respect to the first motion. The peak lateral load was 14.4 kip and occurred at a lateral displacement of approximately 3.7 inches.

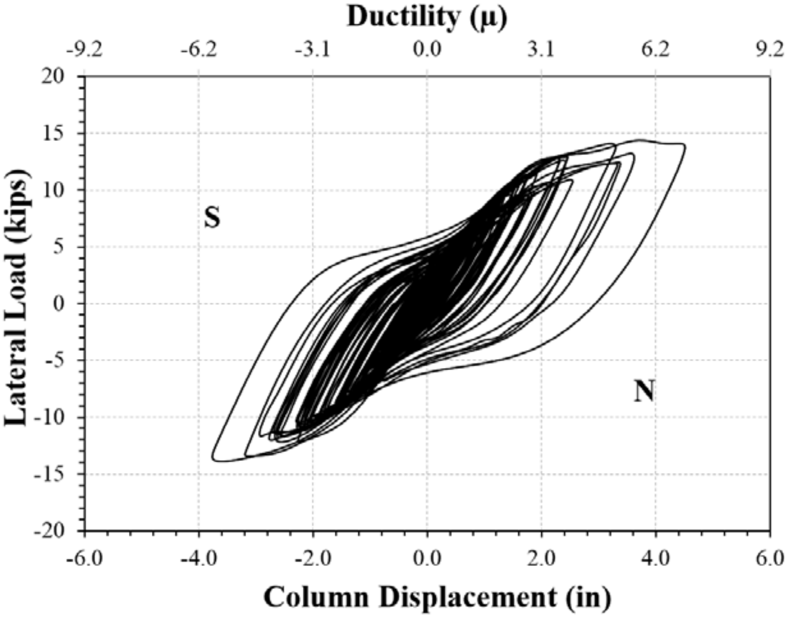

Figure 4.24: Column 2 Load vs. Displacement curve for 1.68 x Curico X

The 1.74xCurico X motion caused the complete failure of the column. Extensive core damage was observed, past the longitudinal bars. The ultimate mode of failure was crushing of concrete, longitudinal bar buckling and longitudinal bar fracture. Three longitudinal bars fractured during this motion, one on the south side and two on the north side of the column. Each bar fractured at mid-height of the buckle length. Three longitudinal bars, two on the south side and one on the north side, buckled across a distance of 6 inches, starting at 2 inches above the footing surface.

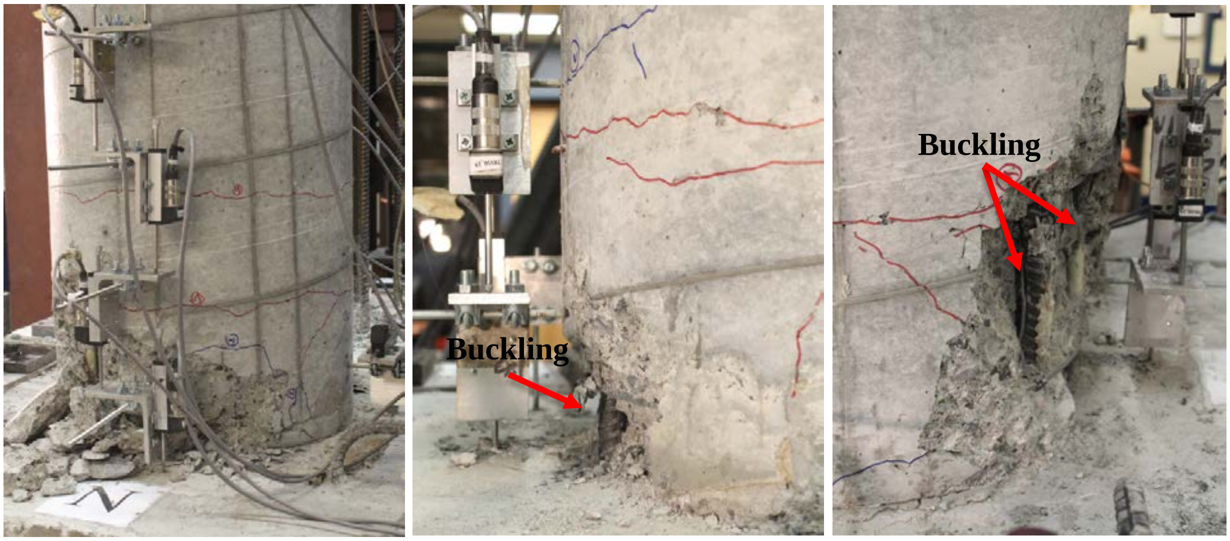

(a) (b) (c)

Figure 4.25: Damage in Column 2 for 1.68 x Curico X. (a) Spalling and crushing of concrete, (b) Bar buckling south side, (c) Bar buckling north side

The final response for 1.74xCurico X is shown in Figure 4.26. The peak lateral load was -12 kip and occurred at a lateral displacement of approximately -4.2 inches. Lateral strength of the specimen decreased about 30% with respect to the lateral strength measured in the first motion.

Based on the experimental results, Column 2 showed a hysteresis response typical of flexural behavior. Measured values for peak top column displacement, ductility and drift are summarized in Table 4.13. Note that the values for the peak lateral force did not occur at the peak top column displacement.

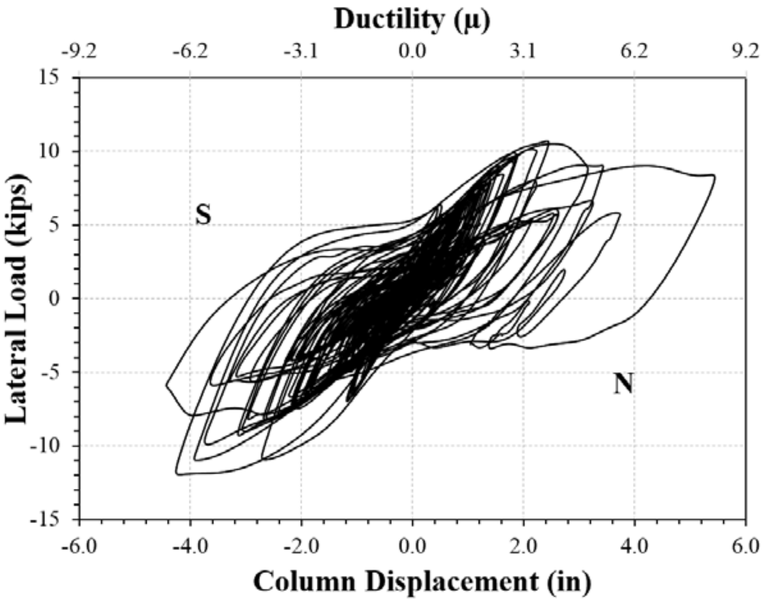

Figure 4.26: Column 2 Load vs. Displacement curve for 1.74 x Curico X

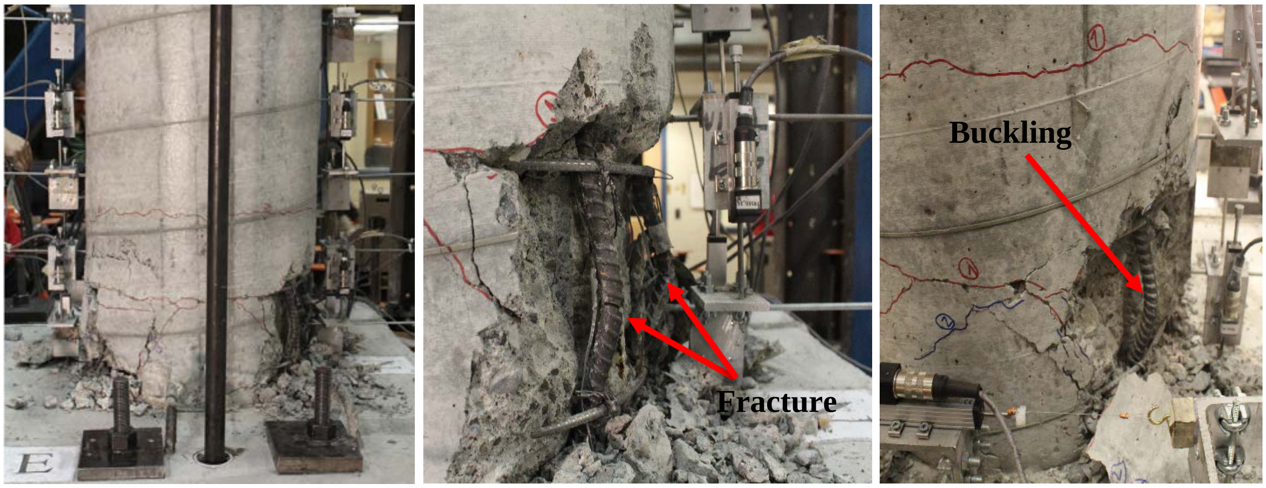

(a) (b) (c)

Figure 4.27: Damage in Column 2 for 1.74 x Curico X. (a) Crushing of concrete, (b) Bar Fracture north side, (c) Bar Buckling south side

Table 4.13: Measured performance for Column 2

Event	Motion S.F	Peak Δ [in]	Peak μ_Δ (Δ_y = 0.65 in.)	Peak Drift Ratio [%]	Peak Lateral Force [kip]	Peak Moment [kip-in]
1	1.57	3.80	5.9	4.0	17.5	1681.7
2	1.68	4.51	6.9	4.7	14.4	1380.3
3	1.74	5.44	8.4	5.7	12.0	1148.2

4.2.7.3 Column 3

The test loading sequence applied to this specimen is listed in Table 4.14. A constant axial load of -75 kips (9% of the column axial capacity) was applied to the specimen. It is worth noting that a reduction of 6.7% in the applied axial load was done before the last motion, as denoted in Table 4.14. Target axial load for last test was then -70 kips.

As in the previous tests, a free vibration test, as well as a low level random motion were performed before and after each motion, in order to obtain the dynamic properties of the specimen. From the performed free vibration test, natural period and damping of the specimen were calculated. The natural period was obtained performing a Fourier analysis of the column free vibration response. The damping ratio ξ was calculated using Equation

$$\ln \frac{u_i}{u_{i+j}} = \frac{2 \cdot \pi \cdot \xi}{\sqrt{1-\xi^2}} \tag{4.5}$$

Table 4.15 shows the dynamic properties for Column 3 measured from the free vibration tests.

From the low level random motion, natural period was obtained using Fourier analysis, whereas the stiffness of the specimen was calculated using Equation 4.6.

$$K = \frac{4 \cdot \pi^2}{T_n^2} \cdot m \tag{4.6}$$

A summary of the calculated stiffness for specimen 3 is shown in **Error! Reference source not found.**.

Table 4.14: Column 3 test loading protocol

Test	**Motion**
FV1	Free Vibration
R1	Random
1	1.77 x Iwaki Y
FV2	Free Vibration
R2	Random
2	1.92 x Iwaki Y
FV3	Free Vibration
R3	Random
AR	Axial Load Reduction
FV4	Free Vibration
R4	Random
3	2.04 x Iwaki Y
FV5	Free Vibration
R5	Random

Table 4.15: Dynamic Properties from Free Vibration tests for Column 3

Test	**Motion S.F**	**Period T_n [sec]**	**Damping ζ [%]**
FV1	1.77	0.39	2.12
FV2	1.92	0.59	3.50
FV3	2.04	0.60	3.60
FV4	2.04	0.65	4.40
FV5	-	0.66	4.54

Table 4.16: Measured elastic stiffness from low level Random motion for Column 3

Test	Motion SF	Period T_n [sec]	Stiffness [kip/in]
R1	1.77	0.40	26.6
R2	1.92	0.59	12.2
R3	2.04	0.60	11.8
R4	2.04	0.64	10.6
R5	-	0.65	10.1

Good agreement for the dynamic properties was found between both tests. As expected from the results of previous tests, as the specimen degraded and the stiffness reduced, the period and the damping of the specimen increased.

Figure 4.28 shows the 1.00xIwaki Y ground motion. Figure 4.29 depicts the target and achieved elastic response spectra for a 5% damping ratio. Target and achieved values of table acceleration, velocity and displacement for each scale factor are given in Table E.3. The shake table performed well for all the motions used in this test.

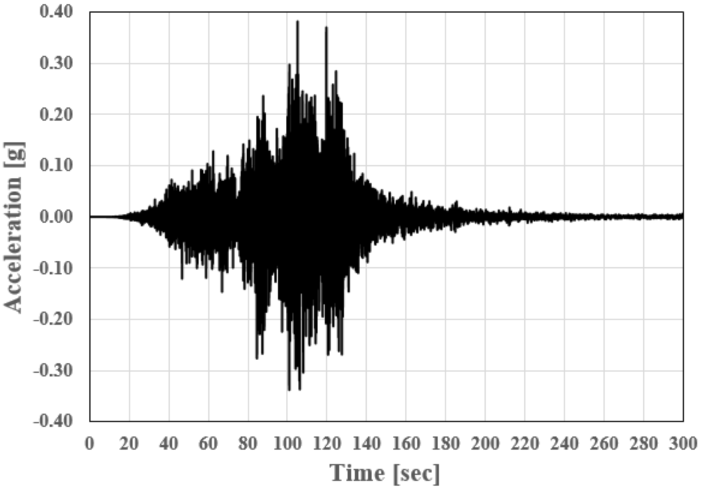

Figure 4.28: Ground acceleration for 1.00 x Iwaki Y

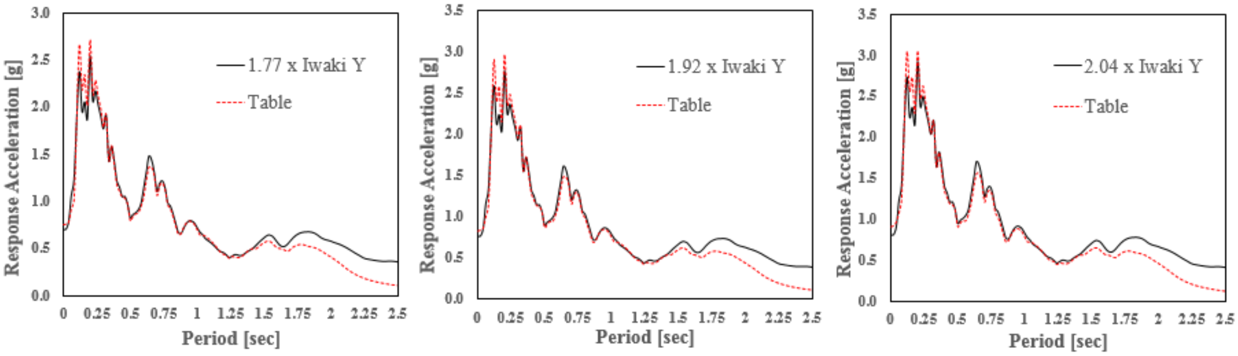

Figure 4.29: Target and achieved elastic response spectra for 5% damping ratio for each motion

Figure 4.30 shows the lateral load vs. displacement hysteresis curve for 1.77xIwaki Y. The experimental yield displacement for this specimen was 0.80 inches. This value was obtained from the reading of the strain gauges placed on the column reinforcement and it was defined as the point at which the first rebar reached a strain over the yield strain (ε_{sy} = 1724 µs). The damage consisted of three major horizontal cracks located in the expected plastic hinge zone, as shown in Figure 4.31(a). Cracks were closed after shaking and developed all around the column about 2, 8, and 14 inches above the footing, at the first three consecutive levels of transverse reinforcement. Some vertical cracks were noticed at the column base. Spalling of the concrete cover in the bottom of the column on the north and south sides was observed after the motion. The spalled region was up to 4 inches in height (Figure 4.31(b)). This specimen suffered less damage than specimen 2 for the same target displacement ductility. No out-of-plane deformation was observed.

The hysteretic behavior of this specimen for the first motion showed a moderate to high ductile behavior by reaching a displacement ductility of 3.8 and slightly over 4 in the positive and negative direction, respectively. The peak lateral load was 16.2 kip and occurred at a lateral displacement of approximately 2.0 inches. After this motion, there was no significant loss in column strength.

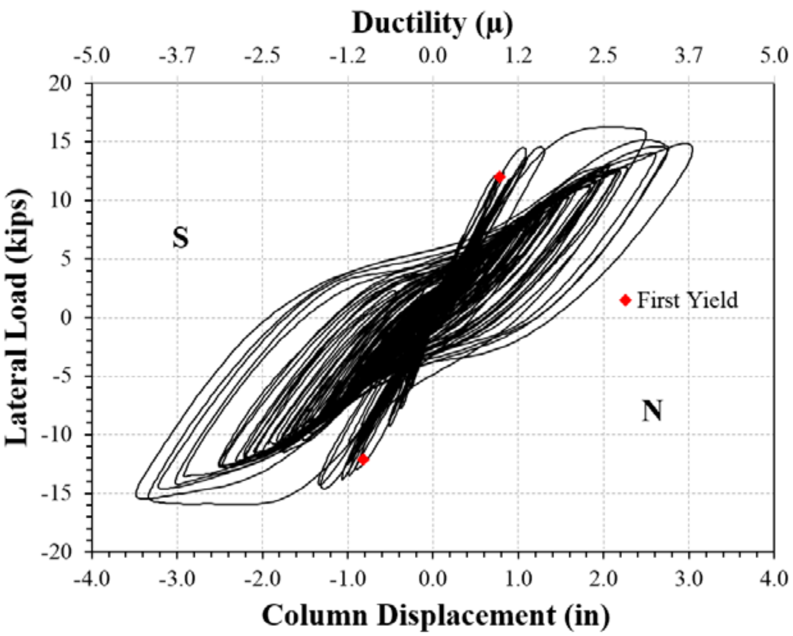

Figure 4.30: Column 3 Load vs. Displacement curve for 1.77 x Iwaki Y

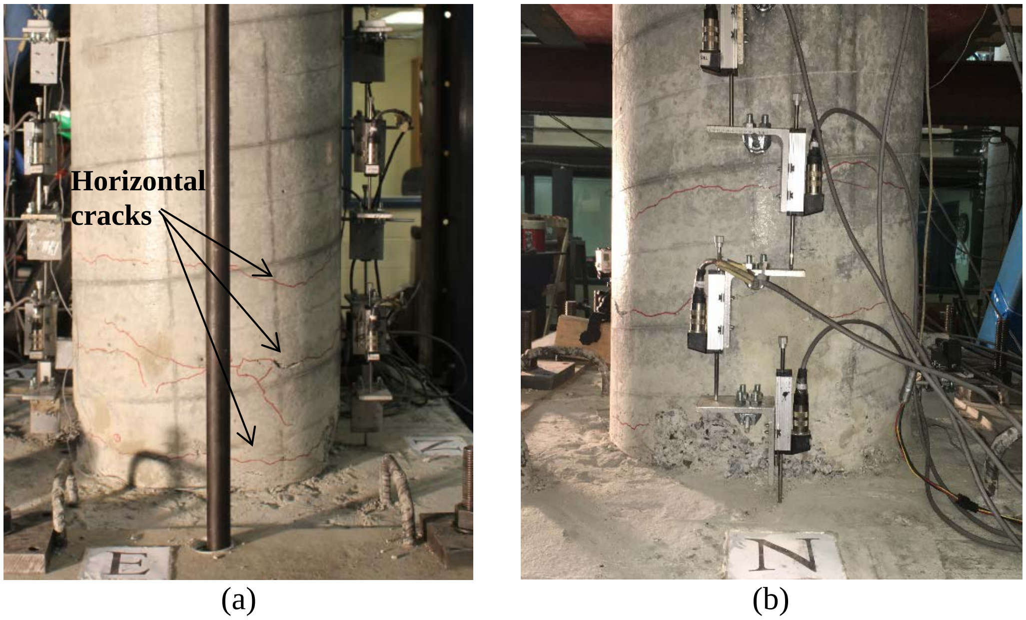

(a) (b)

Figure 4.31: : Damage in Column 3 for 1.77 x Iwaki Y. (a) Horizontal and vertical cracks (b) Spalling of concrete cover

Considerable spalling in the bottom of the column to a height of 8 inches on the south side, as well as propagation of horizontal and vertical cracks was observed after 1.92xIwaki Y (Figure 4.33(a)). Crushing of concrete at the base of the column was observed on the north and south sides. First level of transverse reinforcement was visible on the north and south side. Extreme longitudinal bars were visible on the north and south side, although no significant core damage had happened. The extreme longitudinal bar on the south side buckled across a distance of 6 inches, starting at 2 inches above the footing surface, as shown in Figure 4.33(b). Two failure modes occurred during this motion; crushing of concrete and longitudinal bar buckling. No out-of-plane deformation was observed.

Figure 4.32 shows the lateral load vs. displacement hysteresis curve for 1.92xIwaki Y. The hysteretic behavior for this motion showed a moderate to high ductile behavior by reaching a displacement ductility close to 4 and 5 in the positive and negative direction, respectively. Specimen exhibited a reduction in its lateral strength of about 12% with respect to the first motion. The peak lateral load was 14.4 kip and occurred at a lateral displacement of approximately 3.1 inches.

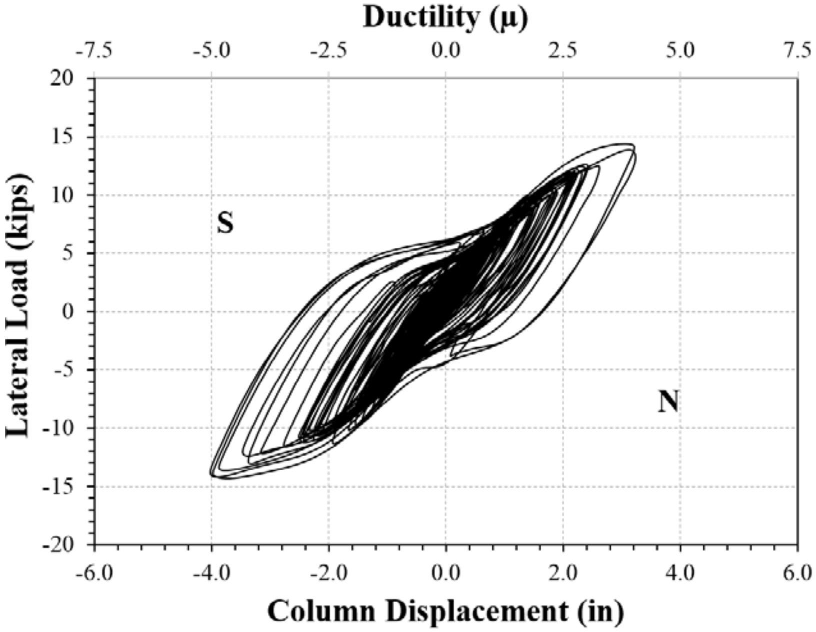

Figure 4.32: Column 3 Load vs. Displacement curve for 1.92 x Iwaki Y

Extensive core damage, past the longitudinal bars, was observed on the south side for 2.04xIwaki Y motion. Fracture of the extreme longitudinal bar on the south side occurred during this motion. The two adjacent longitudinal bars on the south side were buckled across a distance of 6 inches, starting at 2 inches above the footing surface. Since the north side of the column had less visible damage than the south side, it was not possible to see if the longitudinal bars on the north side were buckled. The ultimate mode of failure was crushing of concrete, longitudinal bar buckling and longitudinal bar fracture.

(a) (b)

Figure 4.33: Damage in Column 3 for 1.92 x Iwaki Y. (a) Spalling and crushing of concrete, (b) Bar buckling south side

The final response for 2.04xIwaki Y is shown in Figure 4.34. The peak lateral load was computed as 12 kip in both directions and occurred at a lateral displacement of approximately 2.7 and -3.9 inches, positive and negative direction respectively. Lateral strength of the specimen decreased about 25% with respect to the lateral strength measured in the first motion.

Based on the experimental results, Column 3 showed a hysteresis response typical of flexural behavior. Measured values for peak top column displacement, ductility and drift are summarized in Table 4.17. Note that the values for the peak lateral force did not occur at the peak top column displacement.

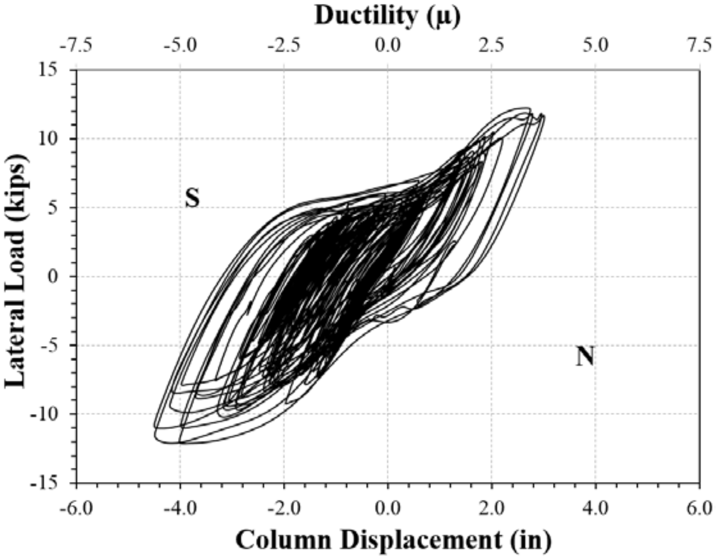

Figure 4.34: Column 3 Load vs. Displacement curve for 2.04 x Iwaki Y

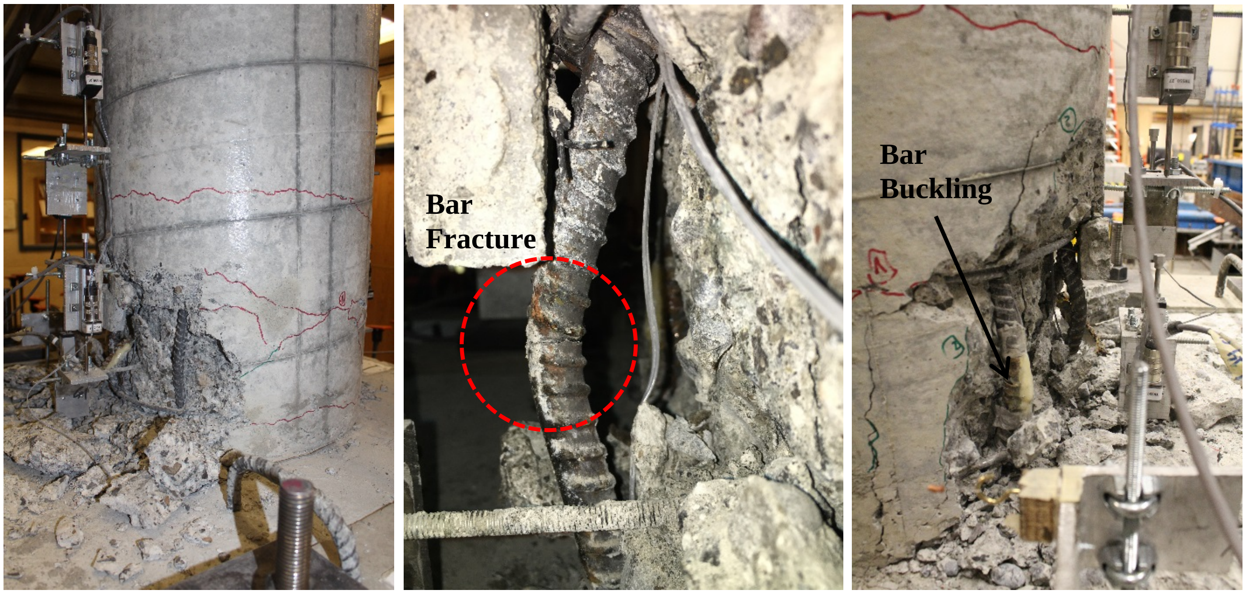

(a) (b) (c)

Figure 4.35: Damage in Column 3 for 2.04 x Curico X. (a) Crushing of concrete, (b) Bar Fracture south side, (c) Bar Buckling south side

Table 4.17: Measured performance for Column 3

Event	**Motion S.F**	**Peak Δ [in]**	**Peak μ_Δ (Δ_y = 0.80 in.)**	**Peak Drift Ratio [%]**	**Peak Lateral Force [kip]**	**Peak Moment [kip-in]**
1	1.77	3.48	4.3	3.6	16.3	1560.3
2	1.92	4.02	5.0	4.2	14.4	1379.8
3	2.04	4.50	5.6	4.7	12.2	1174.4

4.2.7.4 Column 4

The test loading sequence applied to this specimen is listed in Table 4.18. A constant axial load of -75 kips (9% of the column axial capacity) was applied to the specimen.

As in the previous tests, a free vibration test, as well as a low level random motion were performed before and after each motion, in order to obtain the dynamic properties of the specimen. From the performed free vibration test, natural period and damping of the specimen were calculated. The natural period was obtained performing a Fourier analysis of the column free vibration response. The damping ratio ξ was calculated using Equation $\ln \frac{u_i}{u_{i+j}} = \frac{2 \cdot \pi \cdot \xi}{\sqrt{1-\xi^2}}$ (4.5). Table 4.19 shows the dynamic properties for Column 4 measured from the free vibration tests.

From the low level random motion, natural period was obtained using Fourier analysis, whereas the stiffness of the specimen was calculated using Equation

$$K = \frac{4 \cdot \pi^2}{T_n^2} \cdot m$$

(4.6). A summary of the calculated stiffness for specimen 4 is shown in Table 4.20.

Table 4.18: Column 4 test loading protocol

Test	Motion
FV1	Free Vibration
R1	Random (failed)
FV2	Free Vibration
R2	Random
1	1.00 x Capitola X
FV3	Free Vibration
R3	Random
2	1.48 x Capitola X
FV4	Free Vibration
R4	Random

Table 4.19: Dynamic Properties from Free Vibration tests for Column 4

Test	Motion S.F	Period T_n [sec]	Damping ζ [%]
FV1	1.00	0.33	1.67
FV2	1.00	0.44	2.36
FV3	1.48	0.60	3.78
FV4	-	0.66	4.31

Table 4.20: Measured elastic stiffness from low level Random motion for Column 4

Test	Motion SF	Period T_n [sec]	Stiffness [kip/in]
R1	1.00	-	-
R2	1.00	0.44	22.4
R3	1.48	0.58	12.6
R4	-	0.63	10.8

As can be seen in Table 4.18, the first random motion failed due to technical problems. Shake table behaved unstable for this motion, showing high amplitude level instead the preset low level. This issue caused column's natural period to shift to from 0.33 to 0.44 sec, although no visible damage was detected. Once the problem was fixed, the testing protocol was successfully developed.

Good agreement for the dynamic properties was found between both tests. As expected from the results of previous tests, as the specimen degraded and the stiffness reduced, the period and the damping of the specimen increased.

The 1.00xCapitola X ground motion, target and achieved elastic response spectra for a 5% damping ratio, as well as target and achieved values of table acceleration, velocity and displacement for each scale factor, are given in Figure 4.13, Figure 4.14, and Table E.1, respectively. The shake table performed well for all the motions used in this test, but first random motion.

Figure 4.36 shows the lateral load vs. displacement hysteresis curve for 1.00xCapitola X. The experimental yield displacement for this specimen was 0.81 inches. This value was obtained from the reading of the strain gauges placed on the column reinforcement and it was defined as the point at which the first rebar reached a strain over the yield strain (ε_{sy} = 1724 μs). No significant damage was observed in overall. A few horizontal cracks were seen at the base of the column (Figure 4.37(a)). Little spalling of concrete cover was seen at the base of the column on the north side only. Specimen showed vertical cracks consistent with lap splice failure on the north and south side, as illustrated in Figure 4.37(b). This specimen suffered less damage than specimen 1 for the same motion. No out-of-plane deformation was observed.

The hysteretic behavior of this specimen for the first motion showed a moderate ductile behavior by reaching a displacement ductility of 3.7 in both directions. The peak lateral load was -18.6 kip and occurred at a lateral displacement of approximately -2.5 inches. After this motion, there was no significant loss in column strength.

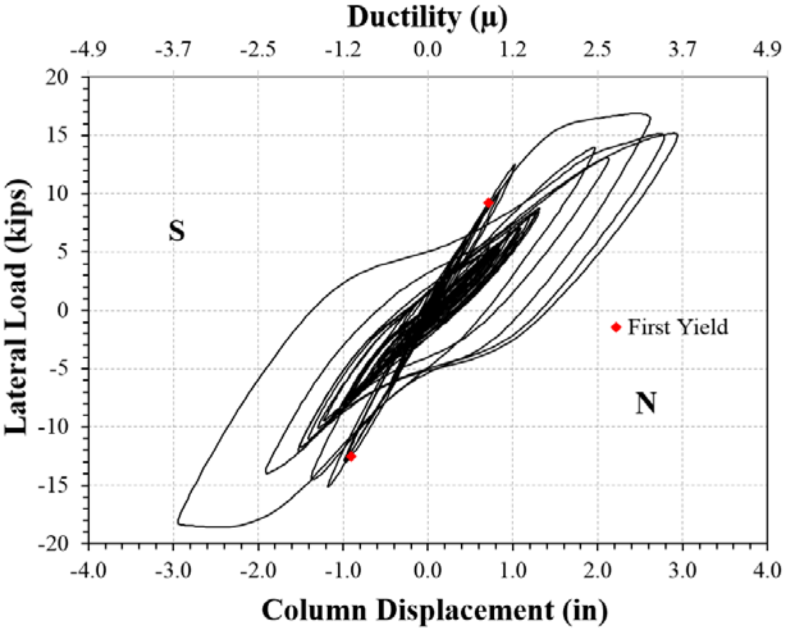

Figure 4.36: Column 4 Load vs. Displacement curve for 1.00 x Capitola X

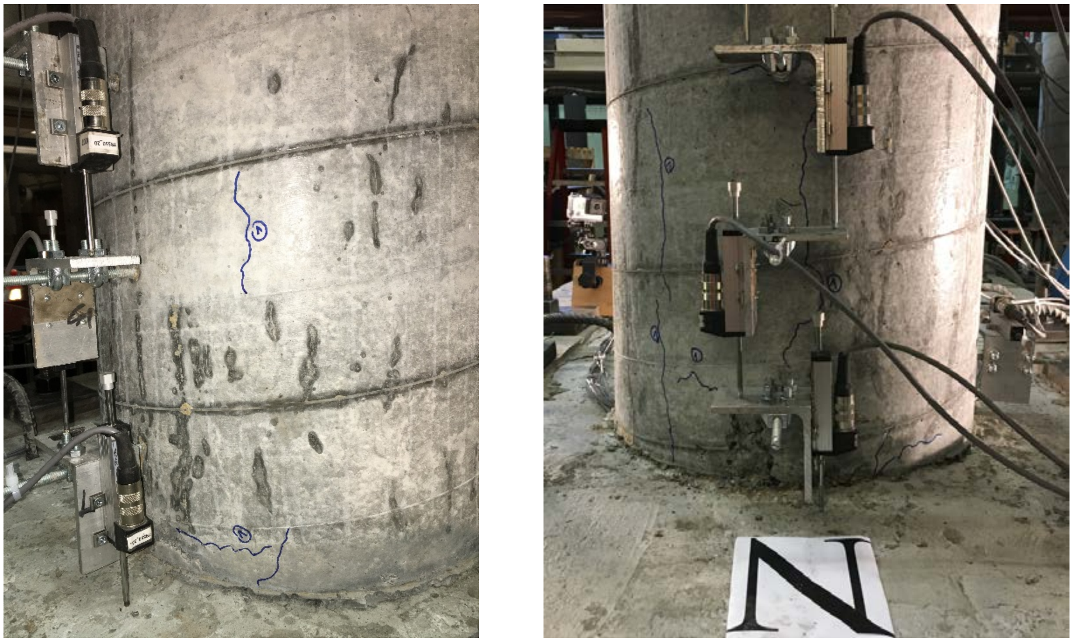

(a) (b)

Figure 4.37: Damage in Column 4 for 1.00 Capitola X. (a) Vertical and horizontal cracks on south side (b) Spalling of concrete cover and vertical cracks on north side

The 1.48xCapitola X motion caused the complete collapse of the column. During testing, the splitting cracks along the spliced length suddenly opened due to the slippage of the spliced bars. This phenomenon was followed by an extensive damage in the column core. Horizontal and vertical cracks propagated over the splice zone around the circumference of the column. Spalling of concrete was observed on the north side over the splice length.

The primary mode of failure was lap splice failure followed by crushing of concrete core, as shown in Figure 4.39. Lateral instability was followed.

Figure 4.38 shows the lateral load vs. displacement hysteresis curve for 1.48xCapitola X. The specimen showed a moderate ductile hysteretic behavior typical of sections with lap-spliced reinforcement. Peak load was computed as 14 kip in the positive direction and -16.3 kip in the negative direction and occurred at a lateral displacement of approximately 3.5 and -2.5 inches, respectively. Once the specimen reached both peak loads, its lateral strength decreased rapidly due to the lap splice failure.

Based on the experimental results, Column 4 showed an initial hysteresis response typical of flexural behavior. Measured values for peak top column displacement, ductility and drift are summarized in Table 4.21.

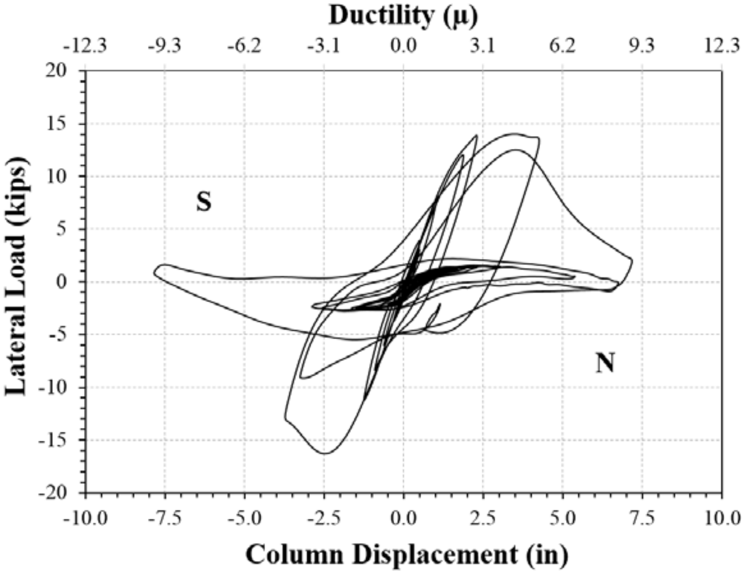

Figure 4.38: Column 4 Load vs. Displacement curve for 1.48 x Capitola X


(a) (b) (c)

Figure 4.39: Damage in Column 4 for 1.48 x Capitola X. (a) South-East side, (b) North side, (c) West side

Table 4.21: Measured performance for Column 4

Event	Motion S.F	Peak Δ [in]	Peak μ_Δ (Δ_y = 0.81 in.)	Peak Drift Ratio [%]	Peak Lateral Force [kip]	Peak Moment [kip-in]
1	1.00	2.95	3.6	3.1	18.6	1785.4
2	1.48	7.84	9.7	8.2	16.3	1563.8

4.2.7.5 Column 5

The test loading sequence applied to this specimen is listed in Table 4.22. A constant axial load of -75 kips (9% of the column axial capacity) was applied to the specimen.

As in the previous tests, a free vibration test, as well as a low level random motion were performed before and after each motion, in order to obtain the dynamic properties of the specimen. From the performed free vibration test, natural period and damping of the specimen were calculated. The natural period was obtained performing a Fourier analysis of the column free vibration response. The damping ratio ξ was calculated using Equation $\ln \frac{u_i}{u_{i+j}} = \frac{2 \cdot \pi \cdot \xi}{\sqrt{1-\xi^2}}$ (4-5). Table 4.23 shows the dynamic properties for Column 5 measured from the free vibration tests. From the low level random motion, natural period was obtained using Fourier analysis, whereas the stiffness of the specimen was calculated using Equation $K = \frac{4 \cdot \pi^2}{T_n^2} \cdot m$ (4.6). A summary of the calculated stiffness for specimen 3 is shown in Table 4.24.

Table 4.22: Column 5 test loading protocol

Test	Motion
FV1	Free Vibration
R1	Random
1	1.57 x Curico X (failed)
FV2	Free Vibration
R2	Random
1	1.57 x Curico X
FV3	Free Vibration
R3	Random

Table 4.23: Dynamic Properties from Free Vibration tests for Column 5

Test	Motion S.F	Period T_n [sec]	Damping ζ [%]
FV1	1.57	0.36	1.63
FV2	1.57	0.46	2.37
FV3	-	0.67	4.13

Table 4.24: Measured elastic stiffness from low level Random motion for Column 5

Test	Motion SF	Period T_n [sec]	Stiffness [kip/in]
R1	1.57	0.36	33.2
R2	1.57	0.46	20.2
R3	-	0.61	11.4

As can be seen in Table 4.22, the first try to replicate the earthquake motion failed due to inconsistencies with some input parameters of the shake table system. On the first try, the test stopped at 25 sec of the ground motion. The issue caused column’s natural period to shift to from 0.36 to 0.46 sec, although no visible damage was detected. Once the problem was fixed, the testing protocol was successfully developed.

Good agreement for the dynamic properties was found between both tests. As expected from the results of previous tests, as the specimen degraded and the stiffness reduced, the period and the damping of the specimen increased.

The 1.57xCurico X ground motion, target and achieved elastic response spectra for a 5% damping ratio, as well as target and achieved values of table acceleration, velocity and displacement are shown in Figure 4.20, Figure 4.21, Table E.2, respectively. The shake table performed well for the motion used in this test.

Figure 4.40 shows the lateral load vs. displacement hysteresis curve for 1.57xCurico X. The experimental yield displacement for this specimen was 0.85 inches. This value was obtained from the reading of the strain gauges placed on the column reinforcement and it was defined as the point at which the first rebar reached a strain over the yield strain (ε_{sy} = 1724 µs). Considerable damage was observed on this specimen. Horizontal and vertical cracks propagated over the spliced length all around the circumference of the column. The vertical cracks were well defined due to slippage of the longitudinal bars. Extensive crushing of concrete at the base of the column on the north and south side. The primary mode of failure was lap splice failure followed by crushing of concrete at the column base, as shown in Figure 4.41. This specimen suffered more damage than specimen 2 for the same ground motion. No out-of-plane deformation was observed.

The specimen showed a moderate ductile hysteretic behavior typical of sections with lap-spliced reinforcement. Peak load was computed as 19.9 kip in the positive direction and -16.8 kip in the negative direction and occurred at a lateral displacement of approximately 2.6 and -2.9 inches, respectively. Once the specimen reached both peak loads, its lateral strength decreased rapidly due to the lap splice failure.

Based on the experimental results, Column 5 showed an initial hysteresis response typical of flexural behavior. Measured values for peak top column displacement, ductility and drift are summarized in Table 4.25. Note that the values for the peak lateral force did not occur at the peak top column displacement.

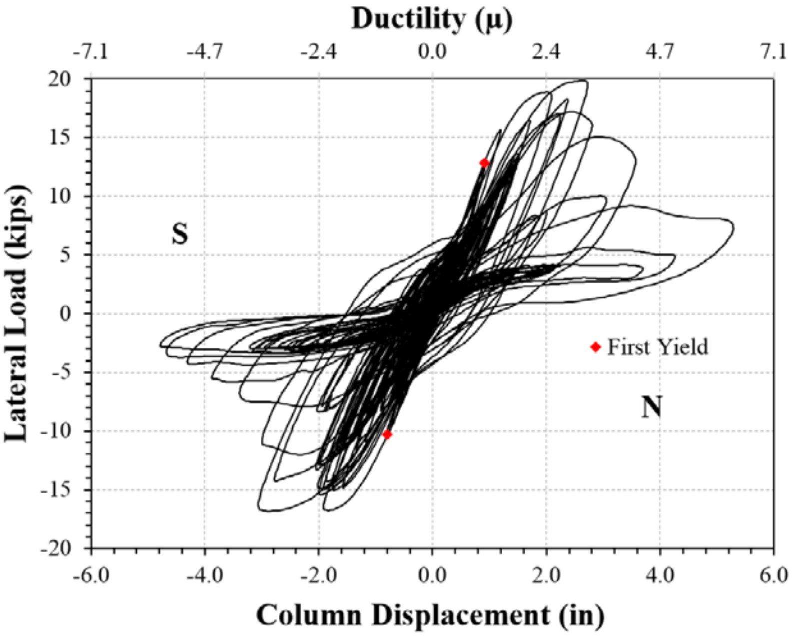

Figure 4.40: Column 5 Load vs. Displacement curve for 1.57 x Curico X

(a) (b) (c)

Figure 4.41: Damage in Column 5 for 1.57 Curico X. (a) South-East side (b) North side, (c) West side

Table 4.25: Measured performance for Column 5

Event	**Motion S.F**	**Peak Δ [in]**	**Peak μ_Δ (Δ_y = 0.85 in.)**	**Peak Drift Ratio [%]**	**Peak Lateral Force [kip]**	**Peak Moment [kip-in]**
1	1.57	5.29	6.2	5.5	19.9	1907.6

4.2.7.6 Column 6

The test loading sequence applied to this specimen is listed in Table 4.26. A constant axial load of -75 kips (9% of the column axial capacity) was applied to the specimen.

As in the previous tests, a free vibration test, as well as a low level random motion were performed before and after each motion, in order to obtain the dynamic properties of the specimen. From the performed free vibration test, natural period and damping of the specimen were calculated. The natural period was obtained performing a Fourier analysis of the column free vibration response. The damping ratio ξ was calculated using Equation

$$\ln\frac{u_i}{u_{i+j}} = \frac{2\cdot\pi\cdot\xi}{\sqrt{1-\xi^2}}$$ (4-5).

Table 4.27 shows the dynamic properties for Column 3 measured from the free vibration tests.

From the low level random motion, natural period was obtained using Fourier analysis, whereas the stiffness of the specimen was calculated using Equation $K = \frac{4\cdot\pi^2}{T_n^2}\cdot m$

(4.6 $K = \frac{4 \cdot \pi^{2}}{T_{n}^{2}} \cdot m$ (4-6). A summary of the calculated stiffness for specimen 3 is shown in Table 4.28.

Table 4.26: Column 6 test loading protocol

Test	Motion
FV1	Free Vibration
R1	Random
1	1.57 x Curico X
FV2	Free Vibration
R2	Random

Table 4.27: Dynamic Properties from Free Vibration tests for Column 6

Test	Motion S.F	Period T_n [sec]	Damping ζ [%]
FV1	1.57	0.33	1.71
FV2	-	0.54	3.39

Table 4.28: Measured elastic stiffness from low level Random motion for Column 6

Test	Motion SF	Period T_n [sec]	Stiffness [kip/in]
R1	1.57	0.33	39.7
R2	-	0.51	16.4

Good agreement for the dynamic properties was found between both tests. As expected from the results of previous tests, as the specimen degraded and the stiffness reduced, the period and the damping of the specimen increased.

The 1.57xCurico X ground motion, target and achieved elastic response spectra for a 5% damping ratio, as well as target and achieved values of table acceleration, velocity and displacement are shown in Figure 4.20, Figure 4.21, Table E.2, respectively. The shake table performed well for the motion used in this test.

Figure 4.42 shows the lateral load vs. displacement hysteresis curve for 1.57xCurico X. The experimental yield displacement for this specimen was 0.70 inches. This value was obtained from the reading of the strain gauges placed on the column reinforcement and it was defined as the point at which the first rebar reached a strain over the yield strain (ε_{sy} = 1724 µs). The damage consisted of spalling of the concrete cover up to 4 inches in height on the north and south sides, as shown in Figure 4.43(a). Figure 4.43(b) shows the vertical cracks along the lap splice at the column base. After the test, crushing of concrete at the column base was observed. This specimen suffered less damage than specimens 2 and 5 for the same motion. No out-of-plane deformation was observed.

The specimen showed a moderate to high ductile hysteretic behavior by reaching a displacement ductility of 5.2 and 4.7 in the positive and negative direction, respectively. The peak lateral load was computed as 18.3 kip in both directions and occurred at a lateral displacement of approximately 2.3 and -2.8 inches, positive and negative direction respectively. After this motion, there was no significant loss in column strength.

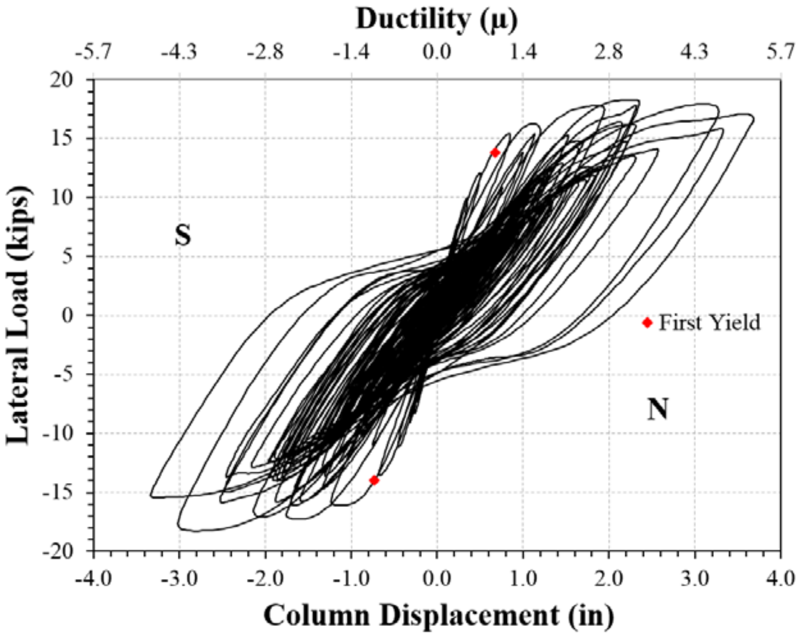

Figure 4.42: Column 6 Load vs. Displacement curve for 1.57 x Curico X

(a) (b)

Figure 4.43: Damage in Column 6 for 1.57 Curico X. (a) Spalling of concrete cover (b) Crushing of concrete and vertical cracks

Based on the experimental results, Column 6 showed a hysteresis response typical of flexural behavior. Measured values for peak top column displacement, ductility and drift are summarized in Table 4.29. Note that the values for the peak lateral force did not occur at the peak top column displacement.

Table 4.29: Measured performance for Column 6

Event	**Motion S.F**	**Peak Δ [in]**	**Peak μ_Δ (Δ_y = 0.70 in.)**	**Peak Drift Ratio [%]**	**Peak Lateral Force [kip]**	**Peak Moment [kip-in]**
1	1.57	3.68	5.2	3.8	18.3	1754.7

4.2.8 Analysis of Results

4.2.8.1 Comparison between backbone curves

One of the objectives of the experimental program was to study the effect of the demand on the column behavior. Figure 4.44 and Figure 4.45 show a comparison between the experimental Load vs. Displacement envelope curves when varying the demand imposed. In Figure 4.44, the specimens had the same cross section, material properties, and continuous longitudinal reinforcement (lap-splice outside the expected plastic hinge zone), but were subjected to different ground motions. For target displacement ductility 4 (Figure 4.44(a)), 1.57xCapitola X motion produces a higher capacity and deflection as compared to the other motions. On the other hand, initial stiffness is lower in column 3 (1.77xIwaki Y motion), while the other two columns have same initial stiffness. For target displacement ductility 6 (Figure 4.44(b)), subduction earthquakes (Curico and Iwaki) produce lower capacity and initial stiffness than the crustal one. Figure 4.45 shows the comparison between the backbone curves for the specimens with the lap splice inside the plastic hinge for the same target displacement ductility 4. While initial stiffness was the same for both specimens, the specimen tested under subduction earthquake showed the typical lap splice failure, as can be found in the literature (Priestley, Seible and Calvi 1996). Column 5 showed a higher strength than Column 4 but decreased rapidly due to the slippage of the longitudinal bars.

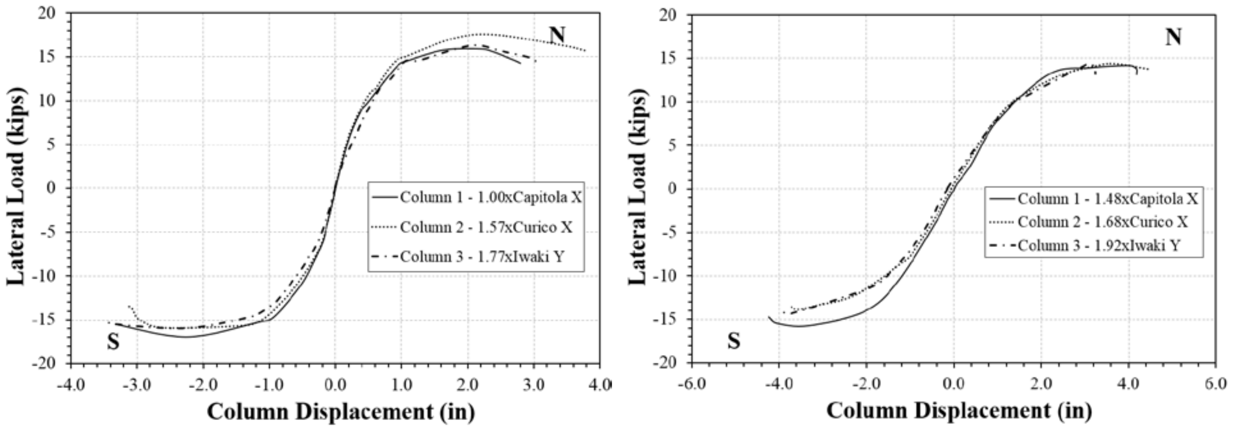

(a) (b)

Figure 4.44: Experimental envelope curves for specimens with continuous longitudinal reinforcing. (a) Comparison for target displacement ductility 4, (b) Comparison for target displacement ductility 6

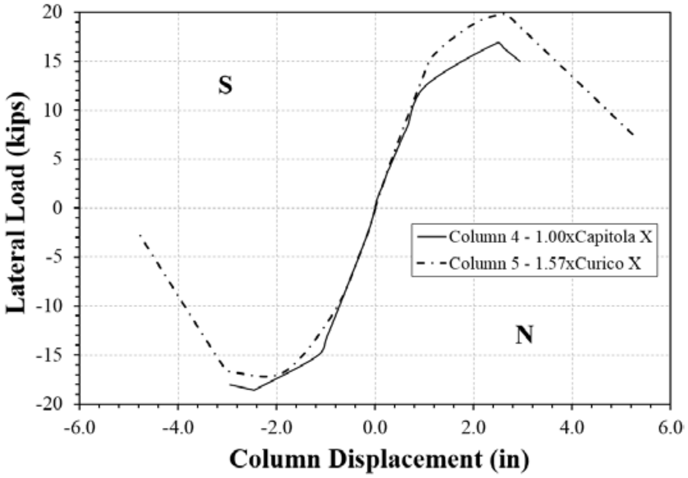

Figure 4.45: Experimental envelope curves for specimens with lap-spliced reinforcement.

The second purpose of the experimental program was to study seismic detailing deficiencies such as sections with lap splices in critical sections. This can be found in bridges constructed in the 1950 to mid-1970 in Oregon. Figure 4.46 shows the performance of Column 1 and Column 4 for a Capitola X motion, which had continuous and lap-spliced reinforcement respectively. Even though specimens showed same initial stiffness and peak capacity for both motion scale factors, Column 4 showed a severe strength degradation after reaching its capacity. This behavior was expected due to the short lap splice length (25d$_b$). Figure 4.47 shows the performance of specimens 2, 5, and 6 for 1.57xCurico X motion, which had continuous reinforcement, and short and long lap-spliced reinforcement respectively. Column 2 and column 6 had the same initial stiffness, while Column 5 was tested with a deteriorated stiffness due to problems with the shake table system. Specimens 2 and 6 showed about the same strength and displacement capacity. This behavior is likely a result of a relatively long lap splice length ($40d_b$). On the other hand, Column 5 showed the typical lap-splice failures but with a higher strength as compared to the other two specimens for the same demand.

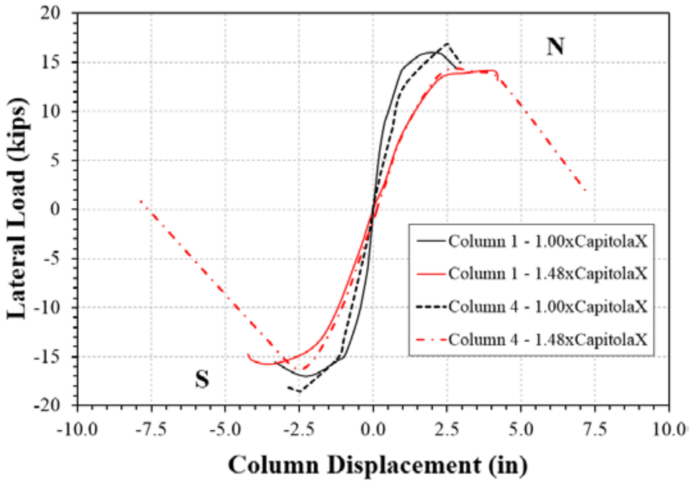

Figure 4.46: Comparison between experimental envelope curves for Capitola X

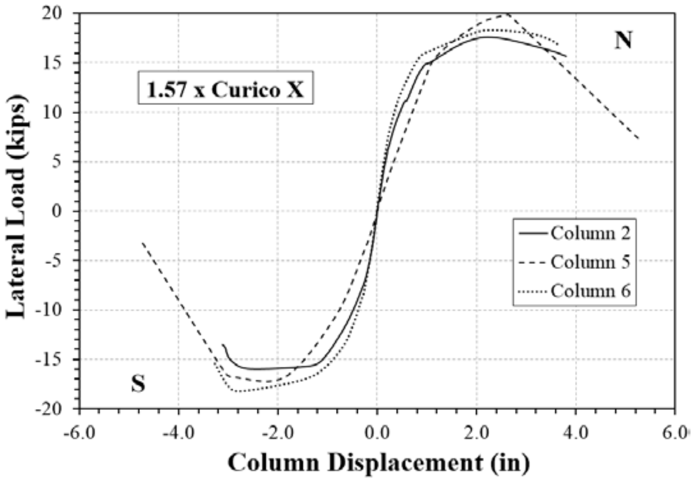

Figure 4.47: Comparison between experimental envelope curves for Curico X

4.2.8.2 Curvature

Linear variable displacement transducers (LDVTs) were used to measure the average curvature along the height of the column. For each level, the average curvature was calculated by dividing the difference between the recorded deflections of the two opposite transducers by the gauge instrumentation length and by the total horizontal distance between the instruments. The curvature details were presented in Section 4.2.5.

The curvature profiles are shown in Figure 4.48 for each specimen. The values of the curvature profiles correspond to the maximum and minimum peak values of column top displacement at different displacement ductility levels. First yield curvature value of ϕ_{yc} = 1.74e-4 rad/in for the columns is represented by dashed lines in each figure. This value was computed using moment-curvature relations. The high curvatures values were measured at the base of the column due to the high moment at the base of each specimen. Moreover, the average curvatures at potential plastic hinge were considerable higher than the calculated yield curvature. When varying the ground motion used (Figure 4.48(a) through Figure 4.48(c)), it can be seen that subduction zone earthquakes induced higher curvatures than crustal earthquakes. Further, specimens with relatively short lap-splice length (Figure 4.48(d) and Figure 4.48(e)) showed higher curvatures than specimen with relatively long lap-splice length (Figure 4.48(f)).

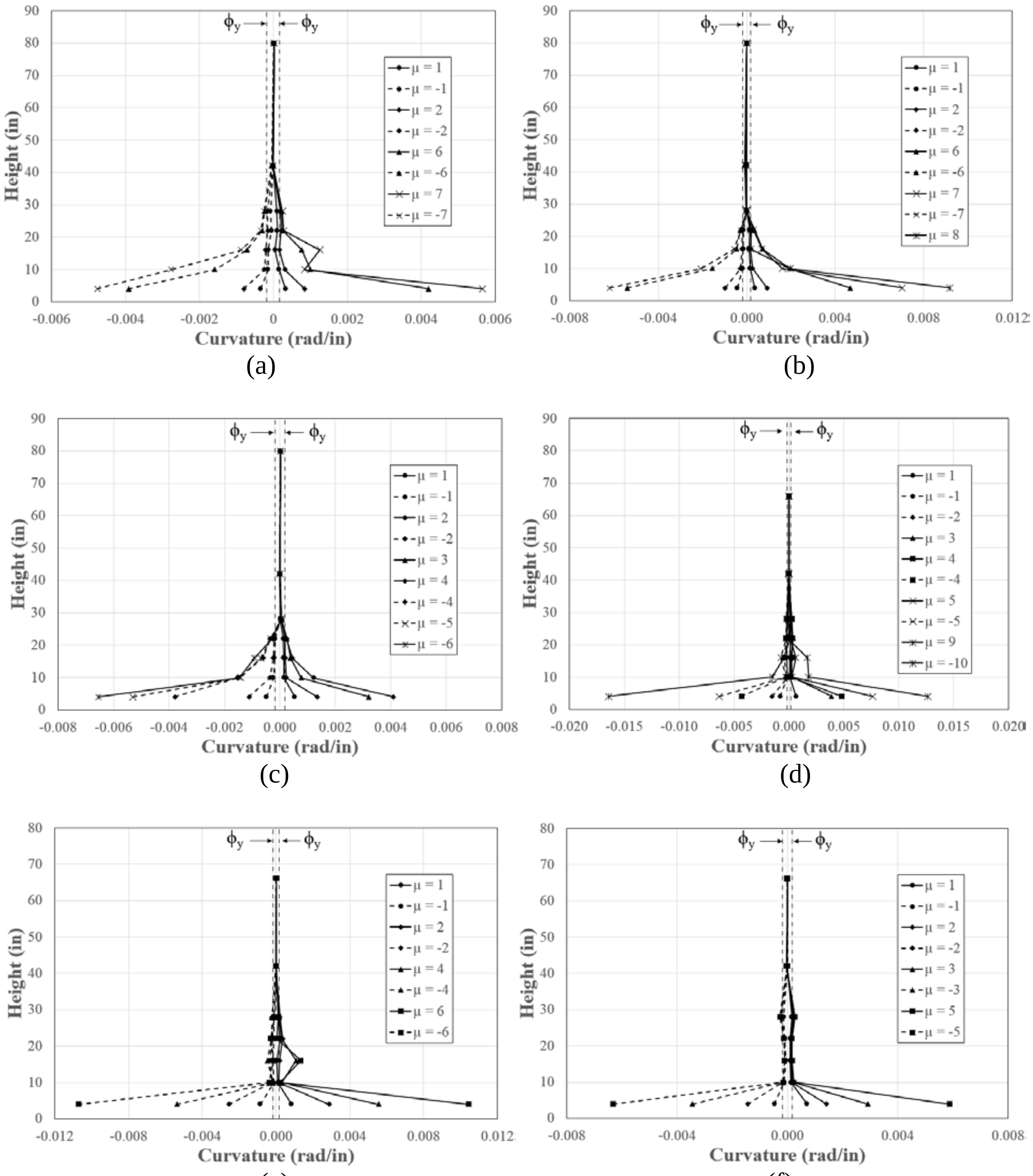

Figure 4.48: Curvature profiles. (a) Column 1, (b) Column 2, (c) Column 3, (d) Column 4, (e) Column 5, (f) Column 6

4.3 SUMMARY

The seismic performance of circular bridge columns was studied through the experimental test of six specimens. This study examined two main variables such as ground motion duration and lap-splice length. The column cross-section used in this study was selected to represent an approximately ½-scale bridge bent. A mass rig system was developed to provide inertial mass for the specimens. This system was designed to support an inertial mass off the test specimen on the shake table system.

First, the effects of the ground motion on the behavior of continuously reinforced concrete bridge columns was studied. Three identically designed specimens were subjected to two different loading scenarios. Column 1 was subjected to a crustal earthquake until failure. Column 2 and Column 3 were shaken under two different subduction zone earthquakes until failure. The second variable to be studied was the behavior of lap-spliced bridge columns. A lap splice length of 25db was used in Column 4 and Column 5, while a 40 db length was provided to Column 6. Moreover, Column 4 was subjected to a crustal earthquake while Column 5 and Column 6 were tested under a subduction earthquake.

The experimental results showed that subduction earthquakes reduce the displacement ductility capacity of reinforced concrete columns and modify the failure mode of the columns. The primary mode of failure for the no lap-spliced columns tested under subduction zone records was buckling and/or fracture of the longitudinal bars at the bottom of the column in the plastic hinge zone. In addition, columns with short lap splice experienced a lap splice failure. On the contrary, Column 1 tested under crustal loading failed showing crushing of concrete as primary mode of failure, while Column 4 showed lap splice failure. The results also validated that longer lap splice length increases the displacement ductility capacity of the column.

5.0 IMPACT ON DUAL DESIGN CRITERIA

5.1 GENERAL

Nowadays, bridge seismic design codes are trending to a relatively new design methodology called “Performance-based seismic design” (PBSD). In this methodology, a number of performance levels, which are frequently defined in terms of acceptable levels of damage, need to be satisfied under different levels of seismic hazards, which are usually referred in terms of specific probability of exceedance.

Many studies are in progress in order to quantify and define performance objectives and limit states of damage to develop a multi-level bridge design methodology. In this progress a few departments of transportation have implemented this methodology, such as CALTRANS, Oregon DOT, and South Carolina DOT *(NCHRP 2013)*. Despite this fact, there is not a national consensus with respect to deformation limits, damage states, and performance objectives and levels. In this section, the performance metrics for performance-based seismic design and retrofit of bridges based on ODOT’s requirements are experimentally evaluated to provide data points for discussion of appropriate strain limits.

5.2 CURRENT ODOT DESIGN PHILOSOPHY

According to ODOT design, two level performance criteria have to be satisfied for the design of new bridges. This means that structural performance is described with two discrete performance levels and two seismic hazards, as is shown in Table 5.1.

Table 5.1: ODOT’s Performance Criteria

Performance Level	Seismic Hazard (Return Period)
Operational	500-year
Life Safety	1000-year

On the other hand, for old bridges ODOT has adopted the performance levels described in the publication “Seismic Retrofitting Manual for Highway Structures, Part 1-Bridges” *(FHWA 2006)*. However, the performance objective, in the case of the Lower Level Ground Motion, is different.

Figure 5.1 illustrates a four level performance criteria adapted from *(Moehle and Deierlein 2004)* to satisfy ODOT requirements.

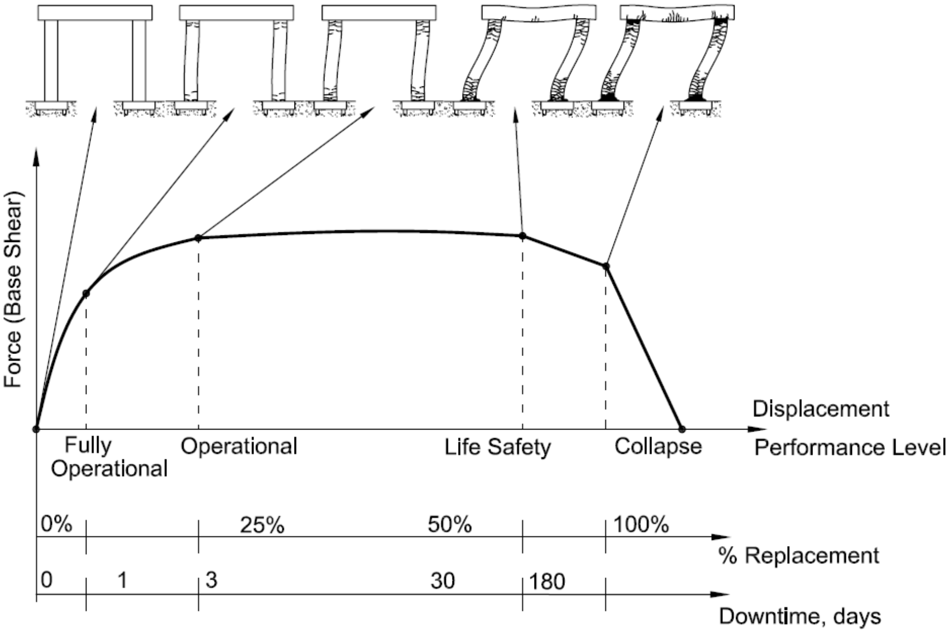

Figure 5.1: Visualization of PBSD (after Moehle and Deierlein 2004), adaptation to ODOT's requirements

5.3 GLOBAL PERFORMANCE LEVELS IN TERMS OF STRAIN

The two-level performance criteria required by ODOT for SDC D in terms of strains is as follows,

Table 5.2: ODOT's Limit States in terms of strains

Performance Level	Seismic Hazard (Return Period)	Steel reinforcing strains	Concrete strains
Operational	500-year	$\varepsilon_s \leq 2\varepsilon_{sh}$	$\varepsilon_{cc} = 0.005$
Life Safety	1000-year	$\varepsilon_s \leq \varepsilon^R_{su}$	$\varepsilon_{cc} = 0.9\ \varepsilon_{cu}$

Where,

ε_s is the reinforcing steel strain

ε_{sh} is the reinforcing steel strain at the onset of strain hardening

ε^R_{su} is the reduced ultimate tensile strain in the reinforcing steel

ε_{cc} is the strain in the confined section of columns

ε_{cu} is the ultimate concrete strain computed using Mander's model

5.4 COMPONENT PERFORMANCE LEVELS

In order to relate the global performance levels to component's levels, a five level component performance is shown in Table 5.3. This table is based on the work carried out by Hose and

Seible *(Hose and Seible 1999)* and adapted to correspond with ODOT's performance criteria. The table also shows the corresponding performance criteria suggested by Hose and Seible, in which the Operational level corresponds to first yielding and minor cracking, and Life Safety corresponds to the onset of spalling.

Table 5.3: Component Performance Levels adapted form Hose & Seible (1999)

Level	Component Performance	Repair Description	Hose & Seible Global Performance	ODOT's Performance
I	Cracking	No Repair	Fully Operational	-
II	First Yield	Possible Repair	Operational	-
III	Effective Yield	Possible Repair	-	-
IV	Onset of Spalling	Minimum Repair	Life Safety	Operational
V	Buckling or Rupture	Replacement	Collapse	Life Safety

5.5 EXPERIMENTAL STRAINS

5.5.1 Square RC column

The experimental program investigating performance of square columns consisted of four test specimens intended to represent full-scale models of typical bridge columns as illustrated in Figure 5.2. All four specimens have the same material properties, cross-sectional dimensions and reinforcement ratios. The variables in the testing program were the column conditions (as-built and retrofitted), loading protocol and applied vertical axial load.

The longitudinal reinforcement in each prototype column consisted of 4 No. 10 bars on four corners with No. 3 stirrups with 90^0 hooks at 12 inches center to center spacing and 2 inches of clear cover concrete confining the column core.

Normal weight concrete was used to construct the test specimens with a target 28-day strength of 3500 psi (24.1 N/mm^2). Standard compression testing of 6-inch (152.4 mm) by 12-inch (304.8 mm) concrete cylinders were performed at approximately 7-day intervals up to 28 days and at the day of test completion. Concrete slump test was also done.

All reinforcing steel used to construct the test specimens consisted of Grade 60 deformed bar conforming to the American Society of Testing and Materials (ASTM) Designation A615. Longitudinal reinforcement consisted of four U.S. No. 10 bars and column ties were created from U.S. No. 3 bars, and footing reinforcements were composed of U.S. No. 6 bars. The column cage and footing cage were assembles in place. There are dowels that extend through the footing to 36 inches (914 mm) from the top of the footing. The longitudinal steel extended through the stubs to 15 mm from the end. The U.S. No. 3 lateral ties were spaced at 12 inches (305 mm) to represent typical pre-1971 column design details.

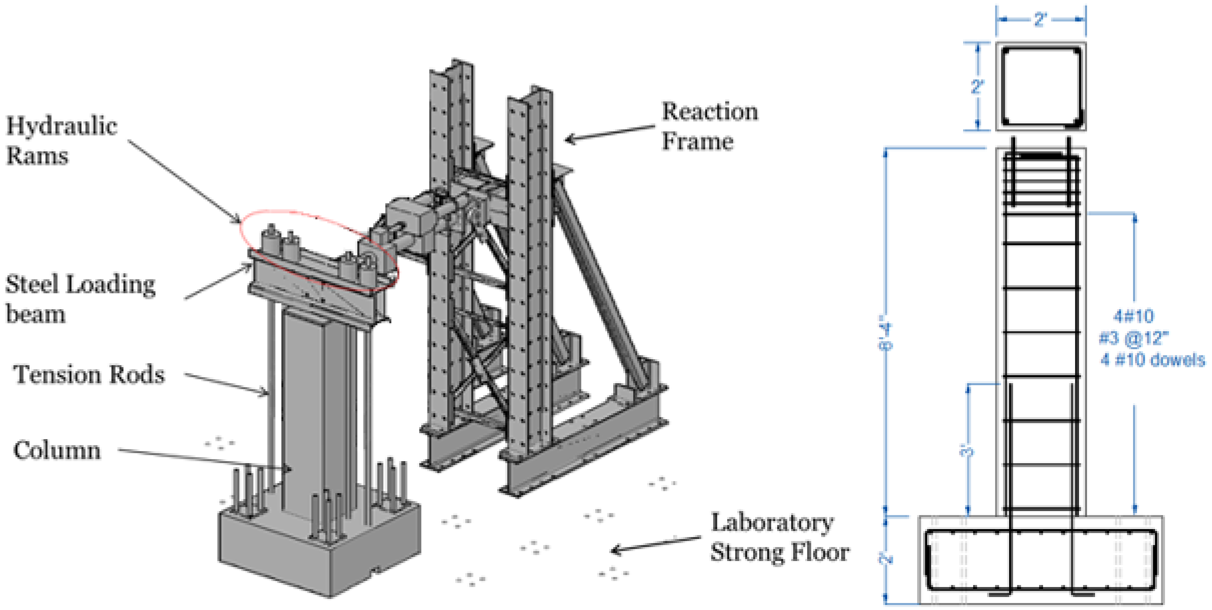

Figure 5.2: Test setup and geometry of RC column specimen

The Figure 5.3 along with Table 5.4 shows the RC square column performance during the experiments:

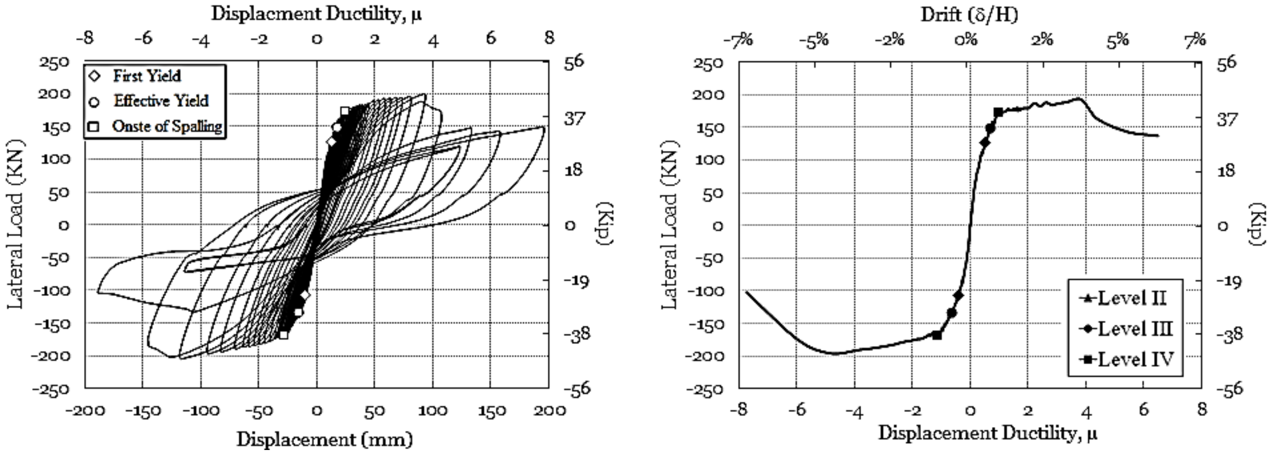

(a) (b)

Figure 5.3: RC square column performance. (a) Force-Displacement Hysteresis Curve, (b) Force-Displacement Envelope

Table 5.4: Bridge Performance Parameters (Limit States) for RC Square Column

Level	Limit State	Steel Strains (ε_s)	Concrete* strains (ε_c)	% Drift	Ductility (μ)
I	Cracking	0.00017	0.0004	0.26	0.4
II	First Yield	0.0024	0.0016	0.46	0.8
III	Effective Yield	x	x	0.60	1
IV	Onset of Spalling	x	x	0.86	1.4
V	Buckling or Rupture	x	x	x	x

* The extreme concrete compressive strains of the columns were obtained using curvature data.

Strain for performance levels III, IV and V were not able to be computed due to failure of strain gauges prior to those levels. There also was rocking at the base of the column where a cold joint between the column and footing exists which made acquiring those strains impossible.

5.5.2 RC Bent

In this section, the performance of a half scale RC bridge bent retrofitted utilizing Buckling Restrained Braces (BRBs) is assessed by presenting and discussing the steel-reinforcement strains and concrete strains. The experimental program consisted of three tests evaluating half-scale models of a RC bridge bent as illustrated in Figure 5.4. The first two experiments consisted of different BRBs options in an effort to assess the influence of BRB stiffness on the overall structural performance. In the third test, the bent was evaluated in the as-built non-retrofitted condition, hereinafter referred to as “As-built”.

The longitudinal reinforcing steel used to construct the test specimens consisted of Grade 40, f_y = 40 ksi, f_u = 60 ksi, deformed bar conforming to the American Society of Testing and Materials (ASTM) designation A615. The measured yield stress for the longitudinal reinforcement was 50 ksi. The transverse steel consisted of deformed wire D5 conforming the ASTM A496.

Normal weight concrete was used to construct the test specimens with a target 28-day strength (f'_c) of 3.3 ksi. Standard compression testing of 6-inch by 12-inch concrete cylinders was performed at 7-day, 28 days and at the day of test completion. The day of testing the compressive strength was 4.8ksi approximately.

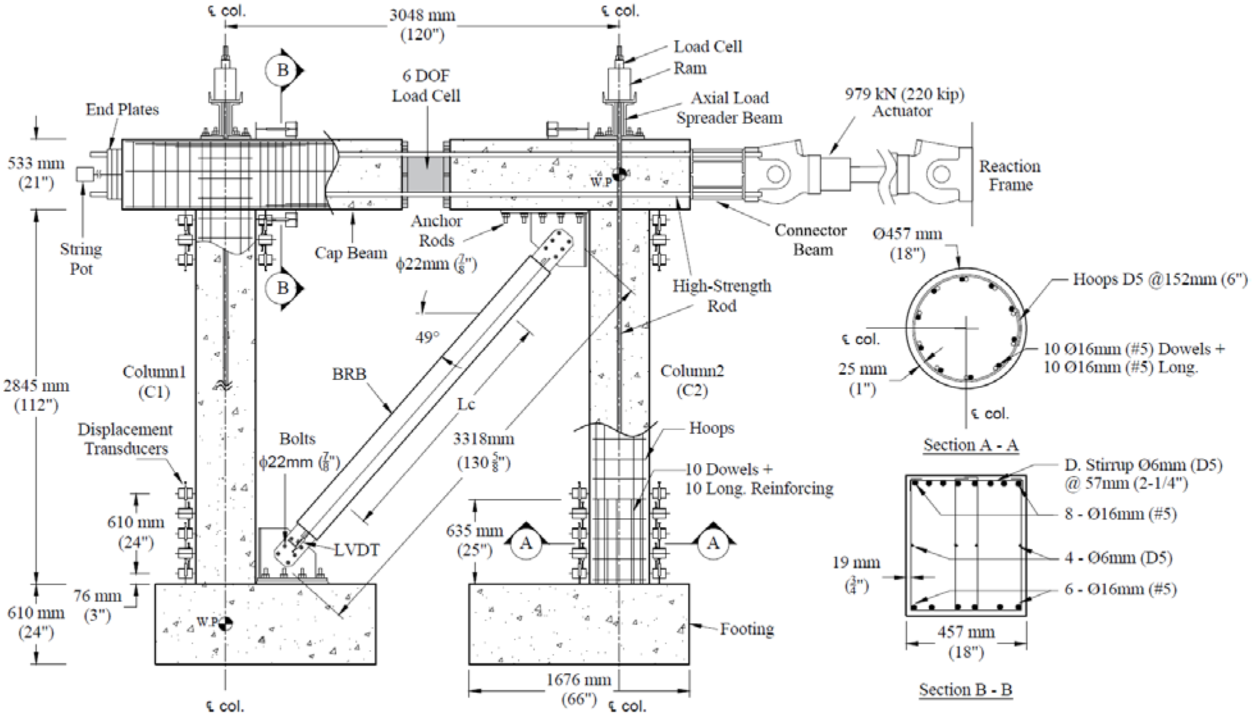

Figure 5.4: Reinforced concrete bent test setup

The Figure 5.5 along withTable 5.5 shows the RC bent performance during the experiments:

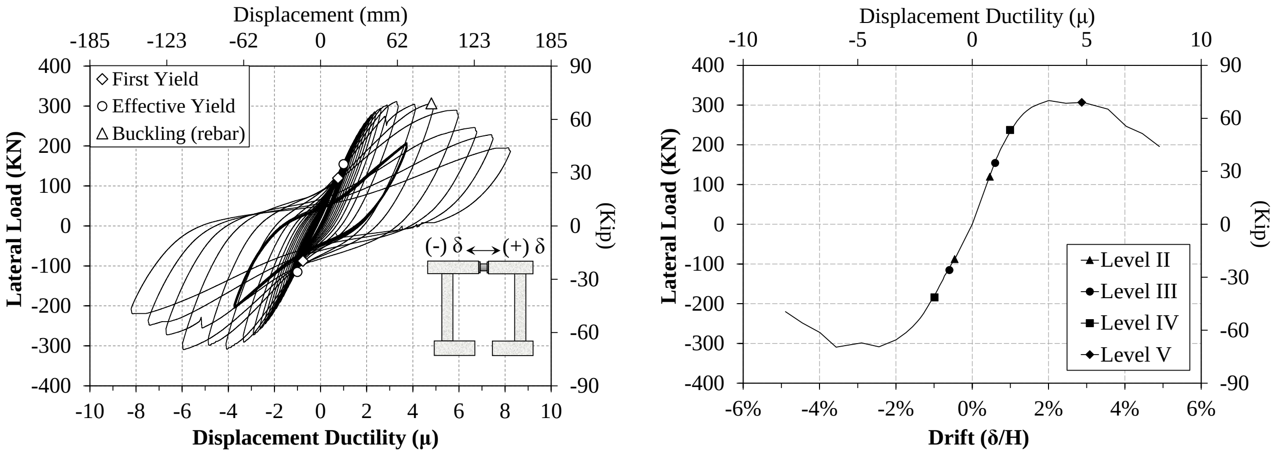

(a) (b)

Figure 5.5: RC bent performance. (a) Force-Displacement Hysteresis Curve, (b) Force-Displacement Envelope

Table 5.5: Bridge Performance Parameters (Limit States) for RC bent

Level	Limit State	Steel Strains (ε_s)	Concrete** strains (ε_c)	% Drift	Ductility (μ)
I	Cracking	0.0008	0.0007	0.21	0.3
II	First Yield	0.0017	0.0012	0.46	0.8
III	Effective Yield	0.0020	0.0017	0.60	1
IV	Onset of Spalling	0.010	0.0042	0.99	1.7
V	Buckling or Rupture	0.048	0.0080	2.87	4.8

** The extreme concrete compressive strains of the columns were obtained using the results from the strains in the reinforcing steel and a linear strain profile for a circular section. The actual values of concrete strain in the confined section are expected to be lower since these values are the maximum compressive strain and not the strain in the confined section.

As a point of comparison, Table 5.6 shows the concrete strains for each ODOT's performance levels. From this table it can be seen that the difference in concrete strains between the operational and the life safety performance level is only 0.002. This low margin is due to the poor confinement given by the transverse reinforcement ratio and detailing, which is typical of RC bents built prior to 1970 in the State of Oregon.

Table 5.6: Expected strain limit states based on ODOT's requirements

Performance Level	Steel reinforcing strains	Concrete strains
Operational	$\varepsilon_s \leq 2\varepsilon_{sh} = 0.03$	$\varepsilon_{cc} = 0.005$
Life Safety	$\varepsilon_s \leq \varepsilon^R_{su} = 0.09$	$\varepsilon_{cc} = 0.9\ \varepsilon_{cu} \approx 0.007$

5.5.3 Circular RC column

In this section, the dynamic performance of scale circular RC bridge columns is assessed by presenting and discussing the steel-reinforcement strains and concrete strains. The experimental program consisted of six test specimens intended to represent scale models of typical circular bridge columns as illustrated in Figure 4.4. All six specimens have the same material properties, cross-sectional dimensions and reinforcement ratios. The variables in the testing program were the ground motion duration and lap splice length.

The longitudinal reinforcing steel used to construct the test specimens consisted of Grade 40, f_y = 40 ksi, f_u = 60 ksi, deformed bar conforming to the American Society of Testing and Materials (ASTM) designation A615. The measured yield stress for the longitudinal reinforcement was 50 ksi. The transverse steel consisted of deformed wire D5 conforming the ASTM A496.

Normal weight concrete was used to construct the test specimens with a target 28-day strength (f'_c) of 3.3 ksi. Standard compression testing of 6-inch by 12-inch concrete cylinders was performed at 7-day, 28 days and at the day of test completion. The day of testing the compressive strength was 4.8ksi approximately.

The following figures (Figures 5.6 and 5.7) and Table 5.7 show the circular RC column performance during the experiments:

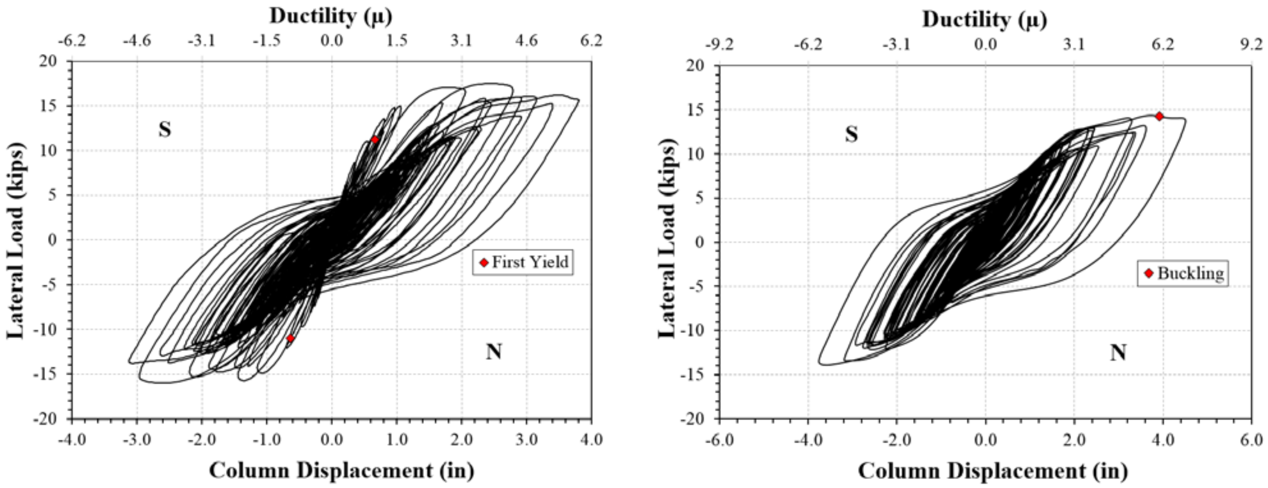

(a) (b)

Figure 5.6: Circular RC column performance. (a) Force-Displacement Hysteresis Curve, (b) Force-Displacement Envelope

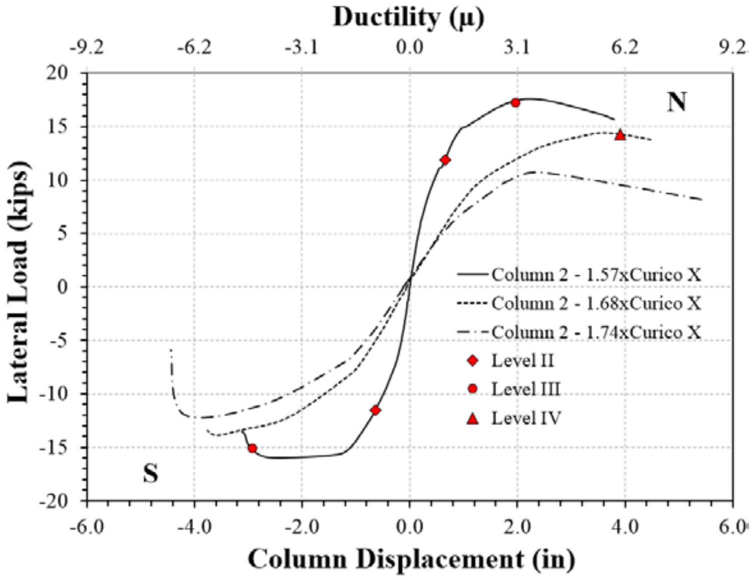

Figure 5.7 : Force-Displacement Envelope for circular RC column

Table 5.7: Bridge Performance Parameters (Limit States) for circular RC columns

Level	Limit State	Steel Strains (ε_s)	Concrete** strains (ε_c)	% Drift	Ductility (μ)
I	Cracking	0.0002	0.0004	0.20	0.3
II	First Yield	0.0013	0.0008	0.68	1.0
III	Effective Yield	-	-	-	-
IV	Onset of Spalling	0.0117	0.0046	2.55	3.8
V	Buckling or Rupture	0.0402	0.0099	4.08	6.0

** The extreme concrete compressive strains of the columns were obtained using the results from the strains in the reinforcing steel and a linear strain profile for a circular section. The actual values of concrete strain in the confined section are expected to be lower since these values are the maximum compressive strain and not the strain in the confined section.

5.6 SUMMARY

ODOT bridges are intended to meet two performance levels. This means that structural performance is described with two discrete performance levels and two seismic hazards. Results from experiments conducted as part of this research as well as previous ODOT based research were used to attempt to quantify various performance levels and associated material strains to initiate the discussion of these strain limits for bridge design. More data is needed to further inform this process, especially for existing bridge detailing and for components outside of the column itself.

Steel reinforcing limits were calculated from the data recorded by strain gauges placed at the potential plastic hinge region for longitudinal reinforcement. Extreme concrete compressive strains of the columns were obtained from two methods; either using the results from the strains in the reinforcing steel and a linear strain profile for a circular section or curvature data collected by linear variable transducers.

6.0 OVERALL SUMMARY AND CONCLUSIONS

Comparison of ground acceleration values expected from a megathrust subduction earthquake originating from the Cascadia Subduction Zone were analyzed and compared to the uniform hazard that has been used to date for the design of bridges in Oregon. The results from the de-aggregation process showed that for a 108 year return period, the uniform hazard values are significantly lower than the CSZ accelerations, as related to the longer return period of the CSZ events. Conversely, for the 2475 year return period, the CSZ values are consistently lower than those that originate from the uniform hazard. However, for the 475 year return period, which corresponds to ODOT’s 500-year Serviceability Criteria as well as the approximate return period of CSZ, the 2002 Uniform Hazard Maps could under predict the ground acceleration for majority of the highways through the Oregon West Coast Range with the exception of the Greater Portland Metro area. Even the 975 year return period, which corresponds to ODOT’s 1000-year No-Collapse Criteria, showed some areas between the coast and I-5 where accelerations exceeded the 2002 Uniform Hazard Maps. Additionally, it was found that the values from the 2002 D-DSHA (deaggregated) are typically higher than those that were generated by the 2002 S-DSHA (scenario). This was believed to be because the difference in fault zone geometry. Whereas S-DSHA uses a defined fault surface and varying hypocenter depth, D-DSHA uses the deaggregated data to select the closest possible fault source, and uses a constant 20 km hypocenter depth. It was found that the 2002 hazard typically predicted larger ground accelerations than the 2008 hazard.

In an effort to recognize the changes with the 2014 USGS hazard, a model for calculating the spectral accelerations was developed based on a full rupture M9 CSZ earthquake. The comparison to the uniform hazard data was characterized by computing the ratio of the 14CSZ model to the uniform hazard models produced by USGS. Results shown that for a 500 year return period, the ratios were greater than or close to one for the region of Oregon between the west coast and approximately I-5 corridor. The exact regions fluctuated between the different model comparisons, but the general trend persisted. This meant that the 14CSZ model calculated approximately the same or greater acceleration values for that region. Moreover, for the areas not in this region the ratio values were less than or close to one, which meant that the acceleration values calculated by the uniform hazard were greater. In the comparison of the 14CSZ model to the USGS models for a 1000-year earthquake the ratio values were almost entirely less than 1 for the entire state of Oregon. It should be noted that for the case of the PSH models, seismic sources other than the CSZ were contribute to the hazard, which can result in greater accelerations in regions less affected by the full-rupture CSZ.

Six lightly-reinforced bridge columns typical to Oregon were subjected to shaking table loading to investigate the effect of subduction ground motion. The inertial loading system developed for this study performed as expected providing reliable mechanism for testing single-degree of freedom columns subjected to ground accelerations. Two sets of three columns were subjected to one crustal and two subduction zone earthquakes. The first set corresponded to circular columns with continuous reinforcement, all of them with same material properties and dimensions. The seismic performance of these specimens showed moderate ductility and was controlled by flexural behavior. For all these specimens, the hysteresis were stable and showed acceptable energy dissipation. The columns resisted several repetitions of earthquakes until failure. The second set of specimens included lap splice in the plastic hinge region; two specimens with short lap splice ($25d_b$) and one column with relatively long but still deficient lap splice ($40d_b$). Specimens with short lap splice showed anticipated lap-splice failure characterized by sudden degradation of their lateral strength after reaching their flexural capacity.

The experimental results also showed that long duration earthquakes reduce the displacement capacity of the column as compared to a short duration. Furthermore, the failure mode of columns can change due to the long duration effects of the earthquake. For continuous reinforced columns, long duration earthquakes induced buckling and fracture of longitudinal bars, while short duration induced crushing of core concrete as the primary failure mode. For lap-spliced specimens, the primary mode of failure was consistently a lap-splice failure, however this failure occurred for lower ductility values when subjected to the subduction motion as compared to short duration. As for the lap splice length, a deficient yet a relatively long lap splice length can improve the performance of the column to the point of moderately ductile behavior.

The measured dynamic properties of the specimens (periods and damping) changed with the damage progression. The periods gradually lengthened with increasing levels of excitation as a consequence of the stiffness degradation. Moreover, the variation in damping also increased within successive runs. The period lengthening was more pronounced for tests using the subduction earthquakes and can have an impact on the post earthquake response of the damaged structures including strong aftershocks.

To satisfy the aims of performance-based seismic design, damage levels that interrupt the serviceability of the structure or require repair techniques could be related to engineering criteria. Three experimental studies, including those conducted as part of this project, were analyzed to assess the performance levels of bridge columns. Performance strain limits recommendations from ODOT’s requirements for new bridges were evaluated using measuring reinforcement strains or curvature data. Based on ODOT’s performance criteria, buckling or rupture of longitudinal reinforcement represents the point at which repair is necessary, interrupting the use of the structure, but not necessarily posing a safety concern. Dynamic test results exhibited bar buckling after reversal from peak tensile strain for subduction zone earthquakes, while significant damage to the core concrete was observed for crustal earthquakes. The experimental results also showed that fracture of previously buckled reinforcement occurred for long duration earthquakes due to the increased number of cycles. When comparing concrete strains between the operational and the life safety performance level, the difference was only 0.002. This low margin is due to the poor confinement given by the transverse reinforcement ratio and detailing, which is typical of RC bents built prior to 1970 in the State of Oregon.

7.0 REFERENCES

AASHTO. *Guide Specifications for LRFD Seismic Bridge Design.* American Association of State Highway and Transportation Officials, 444 N. Capitol Street NW, Washington D.C., 2009..

Addo, K., N. Abrahamson, and R. Youngs. *Probabilistic Seismic Hazard Analysis (PSHA) Model. Volume 3: Ground Motion Characterization (GMC) Model*. Report No. E658-Vol.3, BC Hydro, 2012.

ASCE/SEI. *Minimum Design Loads for Buildings and Other Structures*. Standards ASCE/SEI 7-10. American Society of Civil Engineers.Reston. VA. 2010.

Atkinson, G.M, and D.M. Boore. Empirical Ground-Motion Relations for Subduction-Zone Earthquakes and Their Application to Cascadia and Other Regions. *Bulletin of the Seismological Society of America*, Vol. 93, No. 4, 2003, pp. 1703-1729.

Atkinson, G.M., and M. Macias. Predicted Ground Motions for Great Interface Earthquakes in the Cascadia Subduction Zone. *Bulletin of the Seismological Society of America*, Vol. 3, No. 99, 2009, pp. 1552-1578.

Bazaez, R, P. Dusicka, and S. Knoles. *Bridge Seismic Retrofit Measures Considering Subduction Zone Earthquakes*. Oregon Department of Transportation, Salem, OR, 2015.

Chen, R., A. Frankel, and M. Peterson. 2014. "Implementation of the Cascadia Subduction Zone Source Models for the 2014 Update of the National Seismic Hazard Maps." Report.

Chopra, A. *Dynamic of Structures. Theory and Applications to Earthquake Engineering*. Second Edition. Prentice-Hall, Englewood Cliffs, NJ, 2001.

Dickenson, S. *Recommended Guidelines for Liquefaction Evaluations using Ground Motions from Probabilistic Seismic Hazard Analyses*. Oregon Department of Transportation, Corvallis, OR, 2005.

Douglas, J. A Comprehensive Worldwide Summary of Strong-Motion Attenuation Relationships for Peak Ground Acceleration and Spectral Ordinates (1969 to 2000). *Engineering Seismology and Earthquake Engineering,* Vol. 01, No.103, 2001.

FHWA. 2006. *Seismic Retrofitting Manual for Highway Structures: Part 1-Bridges*. Publication No. FHWA-HRT-06-032, Federal Highway Administration, (FHWA), U.S. Department of Transportation, McLean, VA, 2006.

Frankel , A., C. Mueller, T. Barnhard, D. Perkins, E.V. Leyendecker, N. Dickman, S. Hanson, and M. Hopper. *National Seismic Hazard Maps*. U.S. Geological Survey, Denver, CO, 1996.

Frankel A., M.D. Petersen, C.S. Mueller, K.M. Haller, R.L. Wheeler, E.V. Leyendecker, R.L. Wesson, S.C. Harmsen, C.H. Cramer, D.M. Perkins. *Documentation for the 2002 Update of the National Seismic Hazard Maps*. U.S. Geological Survey Web, Denver, CO, 2002.

Frankel, A. Email correspondence. Portland, Oregon, April 21, 2014.

Frankel, A. *Description of Deterministic Ground Motions for a Mw 9.0 Earthquake on the Cascadia Subduction Zone*. U.S. Geological Survey, Seattle, WA, 2013.

Hose, Y., and F. Seible. *Performance Evaluation Database for Concrete Bridge Components and Systems under Simulated Seismic Loads*. PEER Report 1999/11, Pacific Earthquake Engineering Research Center, Berkeley, CA, 1999.

MATLAB 8.5. *The MathWorks, Inc*. Natick, MA, 2015.

McLean, D., S. Kuebler, and T. Mealy. *Seismic Performance and Retrofit of Multi-Column Bridge Bents*. Technical Report No. WA-RD 449.1. Washington State Transportation Center (TRAC), Pullman, WA, 1998.

Moehle, J., and G. Deierlein. A Framework Methodology for Performance-Based Earthquake Engineering. 13th World Conference on Earthquake Engineering, Vancouver, B.C., Canada, 2004.

National Cooperative Highway Research Program (NCHRP). Performance-Based Seismic Bridge Design, Number 440. In *National Cooperative Highway Research Program Synthesis*, Transportation Research Board, National Academy of Sciences, Washington, D.C., 2013.

ODOT. *Sesimic Design*. Geotechnical Design Manual. Oregon Department of Transportation, Salem, OR 2013.

OpenSees. *Open System for Earthquake Engineering Simulation*, Pacific Earthquake Engineering Research Center. 2011. http://opensees.berkeley.edu.

Oregon Geospatial Enterprise Office, 625. *Oregon State Government*.2015. http://www.oregon.gov/DAS/CIO/GEO/pages/coordination/projections/projections.aspx.

Pantelides, C.P., and J. Gergely. Seismic Retrofit of Reinforced Concrete Beam-Column T-Joints in Bridge Piers with FRP Composite Jackets. *ACI Special Publication*, Vol. 258-1, 2008.

Petersen, M.D., A.D. Frankel, S.C. Harmsen, C.S. Mueller, K.M. Haller, R.L. Wheeler, R.L. Wesson, Y. Zeng, O.S. Oliver, D.M. Perkins, N. Luco, D.H. Field, C.J. Wills, and K.S.

Rukstales. *Documentation for the 2008 Update of the United States National Seismic Hazard Maps*. U.S. Geological Survey, Reston, VA, 2008.

Peterson, M., M. Moschetti, P. Powers, C. Mueller, K. Haller, A. Frankel, and A. Olsen. *Documentation for the 2014 Update of the United States National Seismic Hazard Maps*. Reston, Virginia: U.S. Geological Survey, Reston, VA, 2014.

Sadigh, K., C. Egan, J. Chang, F. Makdisi, and R. Youngs. Attenuation Relationships for Shallow Crustal Earthquakes Based on California Strong Motion Data. Web: *Seismological Research Letters*, Vol. 68, 1997, pp. 180-189.

Van Rossum, G. *Phyton Programming Language 3.4.3*. 2015 www.python.org. https://docs.python.org/3/tutorial/.

Youngs, R., S. Chiou, W. Silva, and J. Humphrey. Strong Ground Motion Attenuation Relationships for the Subduction Zone Earthquakes. Web: *Seismological Research Letters*, Vol. 68, 1997, pp. 58-73.

Zhao, J., J. Zhang, A. Asano, Y. Ohno, T. Oouchi, T. Takahashi, H. Ogawa, K. Irikura, H.K. Thio, P.G. Somerville, Y. Fukushima, Y. Fukushima. Attenuation Relations of Strong Ground Motion in Japan Using Site Classification Based on Predominant Period. *Bulletin of the Seismological Society of America*, Vol. 96, No. 3, 2006, pp. 898-913.

APPENDIX A

RESULTS FROM CHAPTER 2

APPENDIX A – RESULTS FROM CHAPTER 2

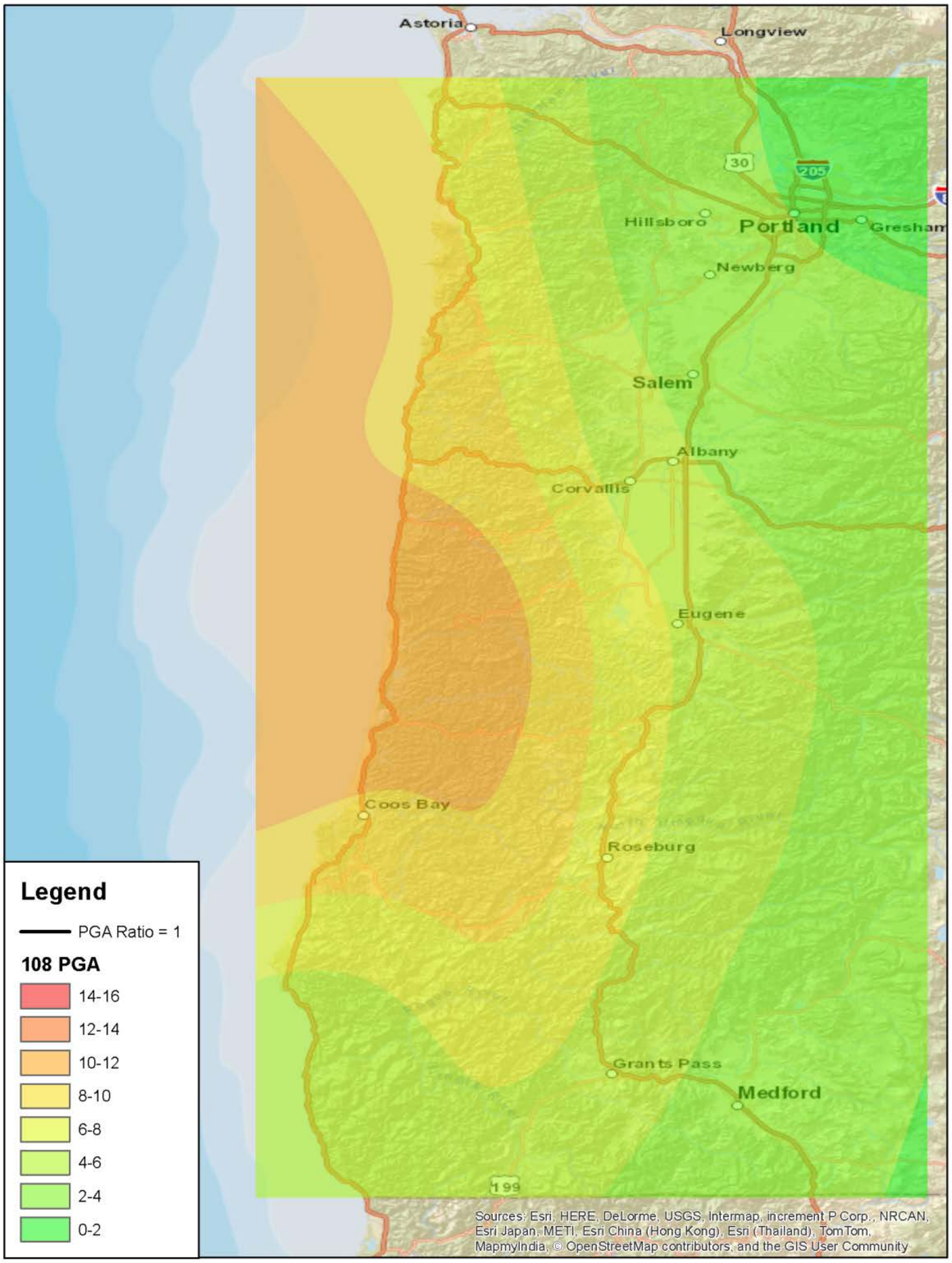

Figure A- 1: Ratio of 2002 D-DSHA and the 2002 UHS Maps for the peak ground acceleration and 108 year return period

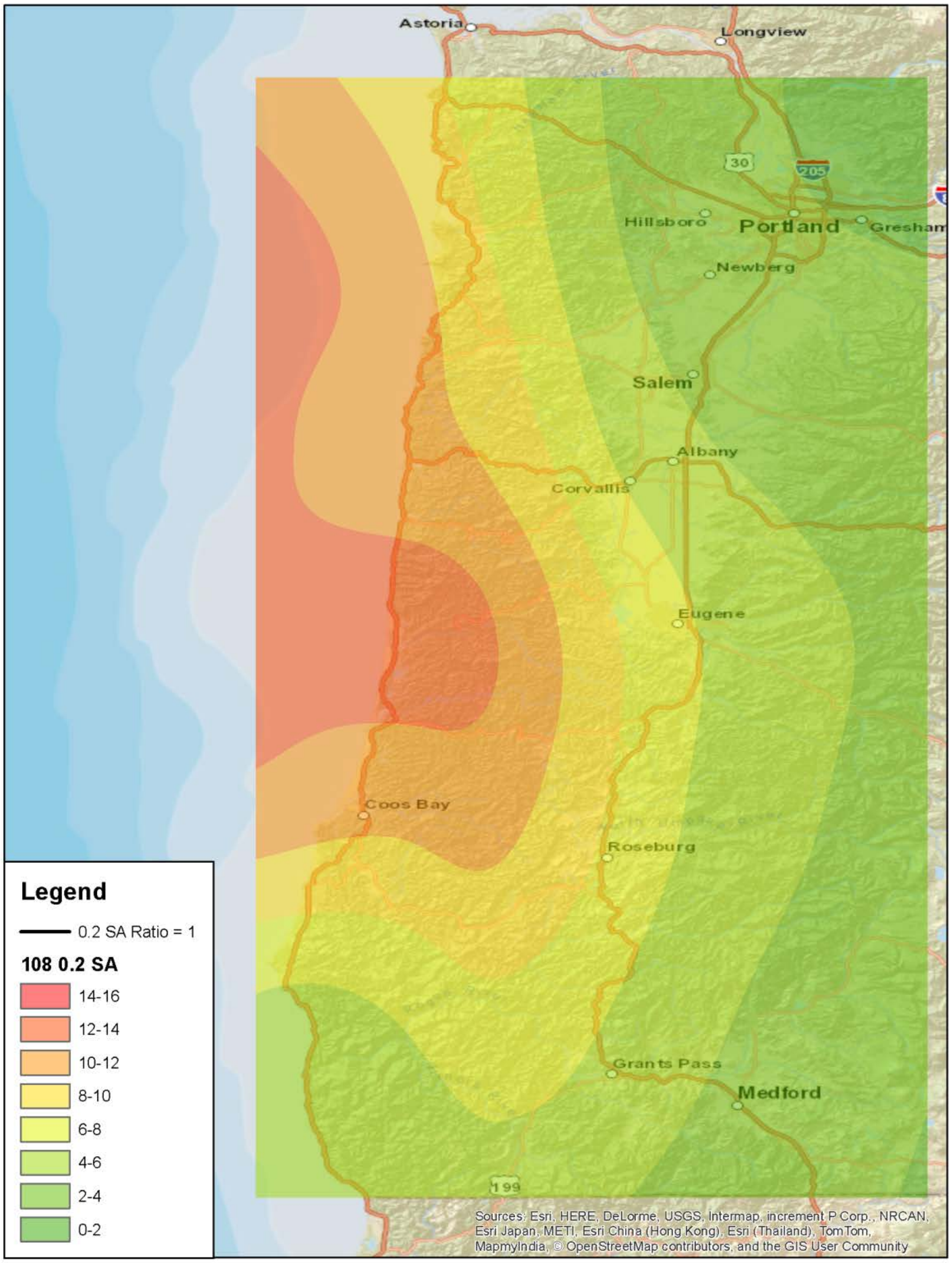

Figure A- 2: Ratio of 2002 D-DSHA and the 2002 UHS Maps for the 0.2 second spectral acceleration and 108 year return period

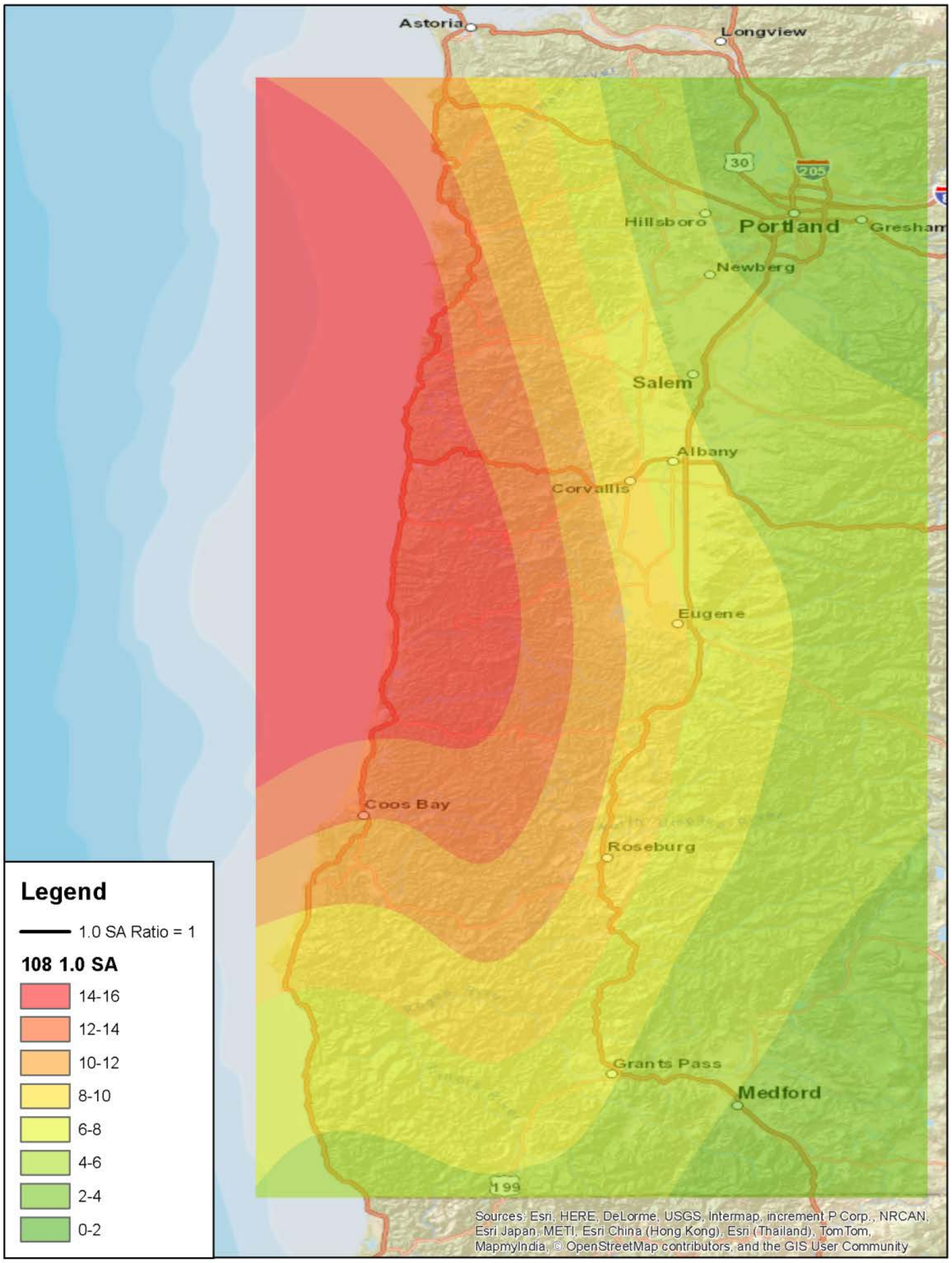

Sources: Esri, HERE, DeLorme, USGS, Intermap, increment P Corp., NRCAN, Esri Japan, METI, Esri China (Hong Kong), Esri (Thailand), TomTom, MapmyIndia, © OpenStreetMap contributors, and the GIS User Community

Figure A- 3: Ratio of 2002 D-DSHA and the 2002 UHS Maps for the 1.0 second spectral acceleration and 108 year return period

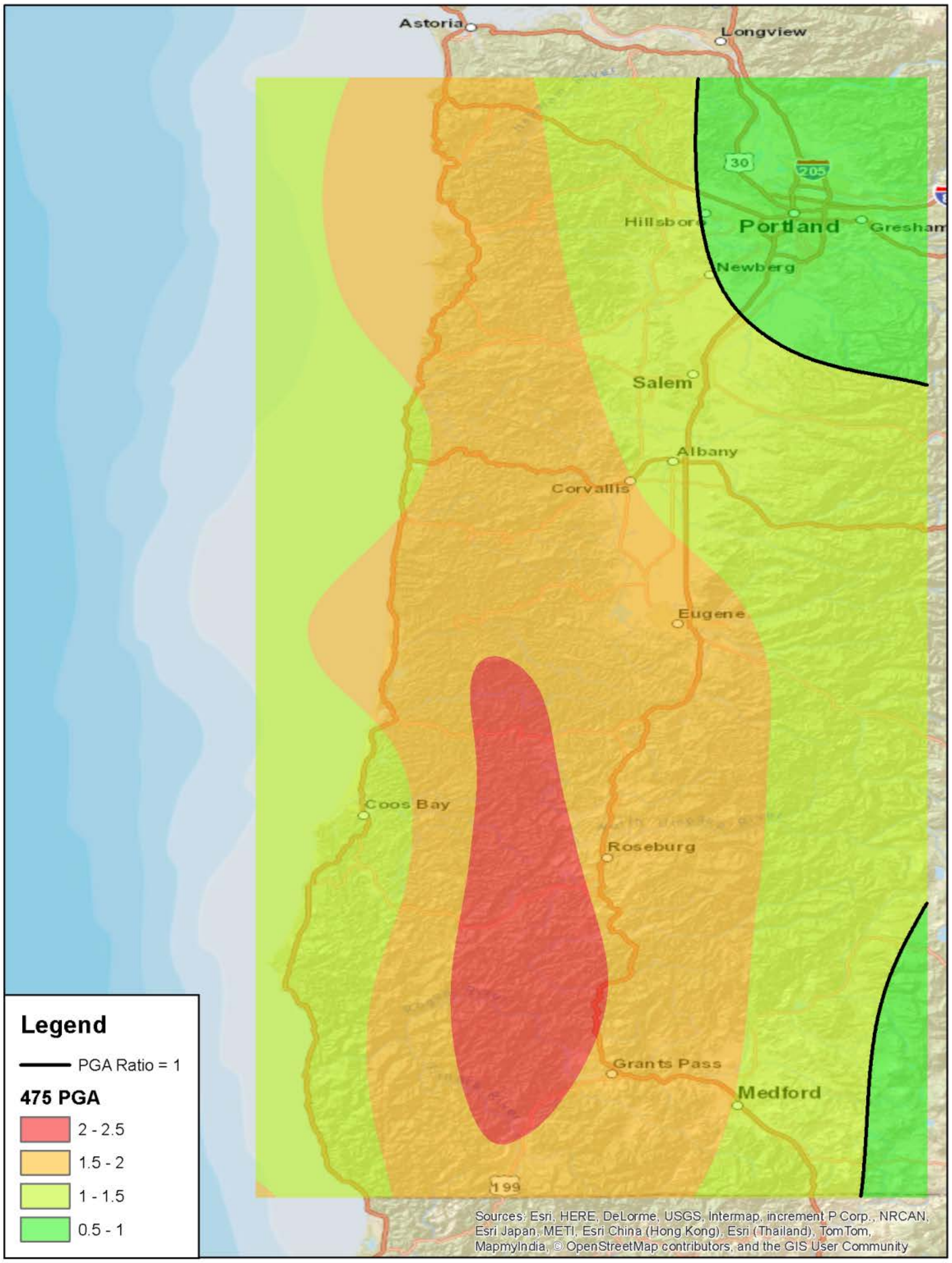

Sources: Esri, HERE, DeLorme, USGS, Intermap, increment P Corp., NRCAN, Esri Japan, METI, Esri China (Hong Kong), Esri (Thailand), TomTom, MapmyIndia, © OpenStreetMap contributors, and the GIS User Community

Figure A- 4: Ratio of 2002 D-DSHA and the 2002 UHS Maps for the peak ground acceleration and 475 year return period

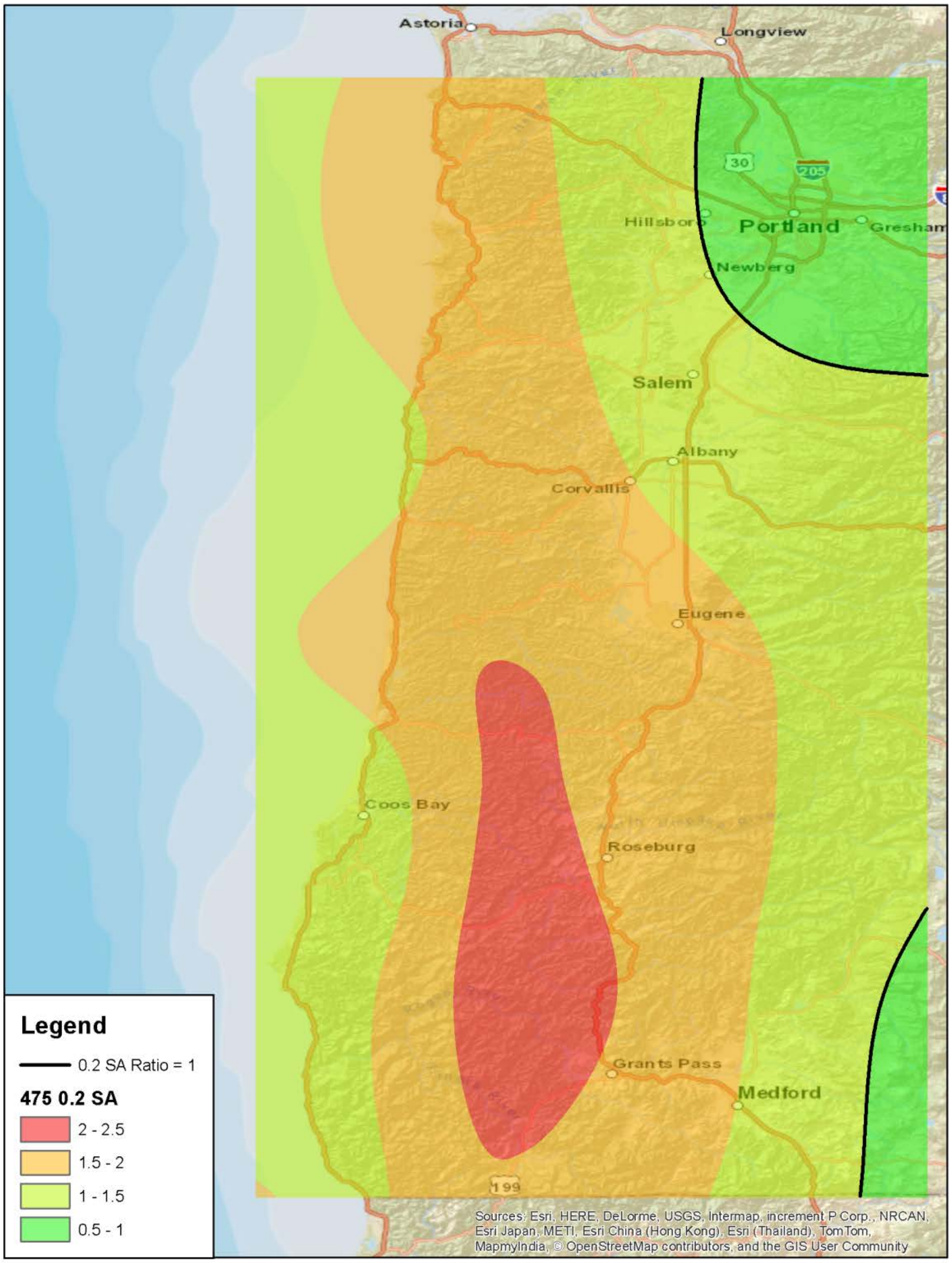

Sources: Esri, HERE, DeLorme, USGS, Intermap, increment P Corp., NRCAN, Esri Japan, METI, Esri China (Hong Kong), Esri (Thailand), TomTom, MapmyIndia, © OpenStreetMap contributors, and the GIS User Community

Figure A- 5: Ratio of 2002 D-DSHA and the 2002 UHS Maps for the 0.2 second spectral acceleration and 475 year return period

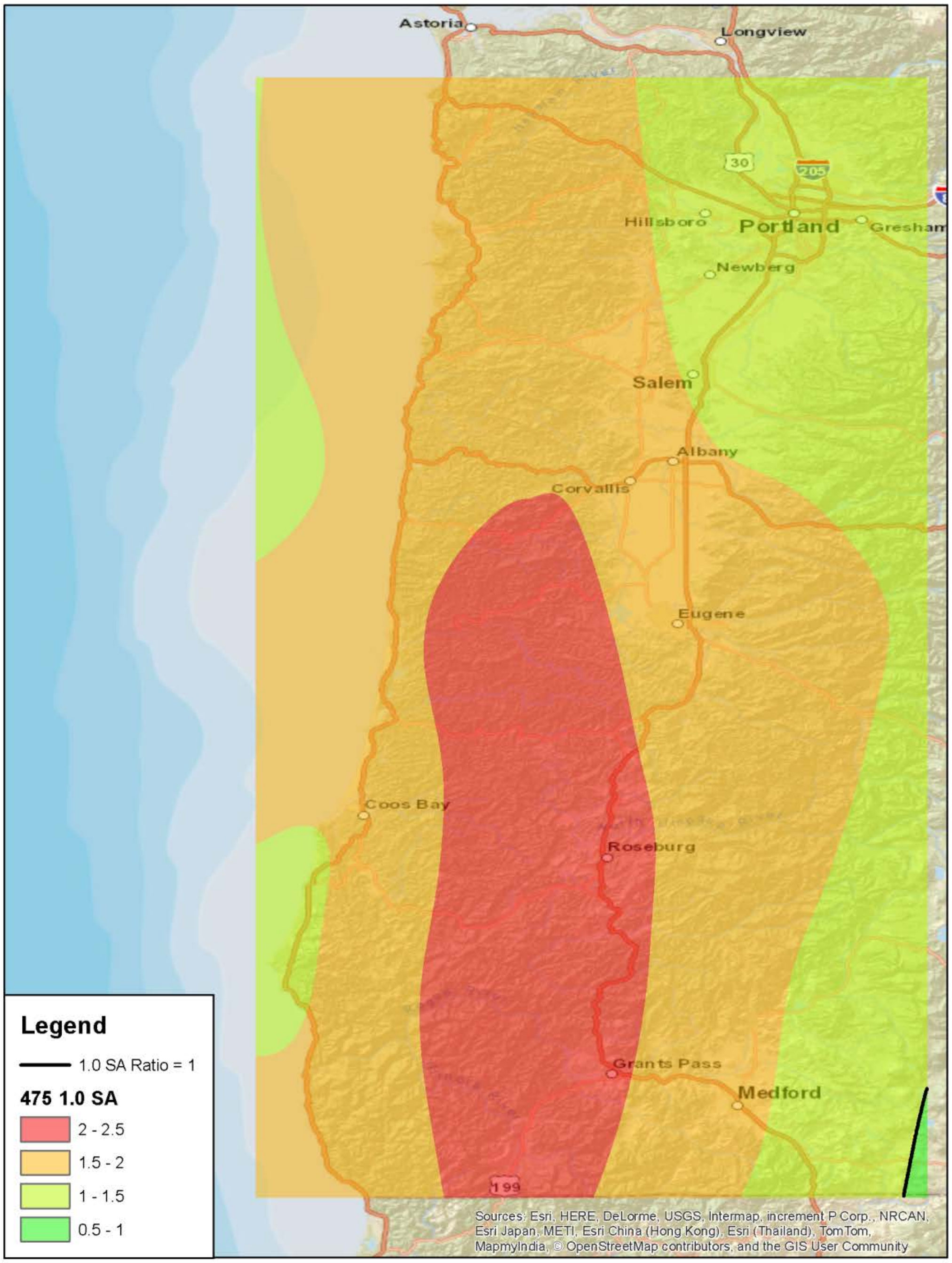

Sources: Esri, HERE, DeLorme, USGS, Intermap, increment P Corp., NRCAN, Esri Japan, METI, Esri China (Hong Kong), Esri (Thailand), TomTom, MapmyIndia, © OpenStreetMap contributors, and the GIS User Community

Figure A- 6: Ratio of 2002 D-DSHA and the 2002 UHS Maps for the 1.0 second spectral acceleration and 475 year return period

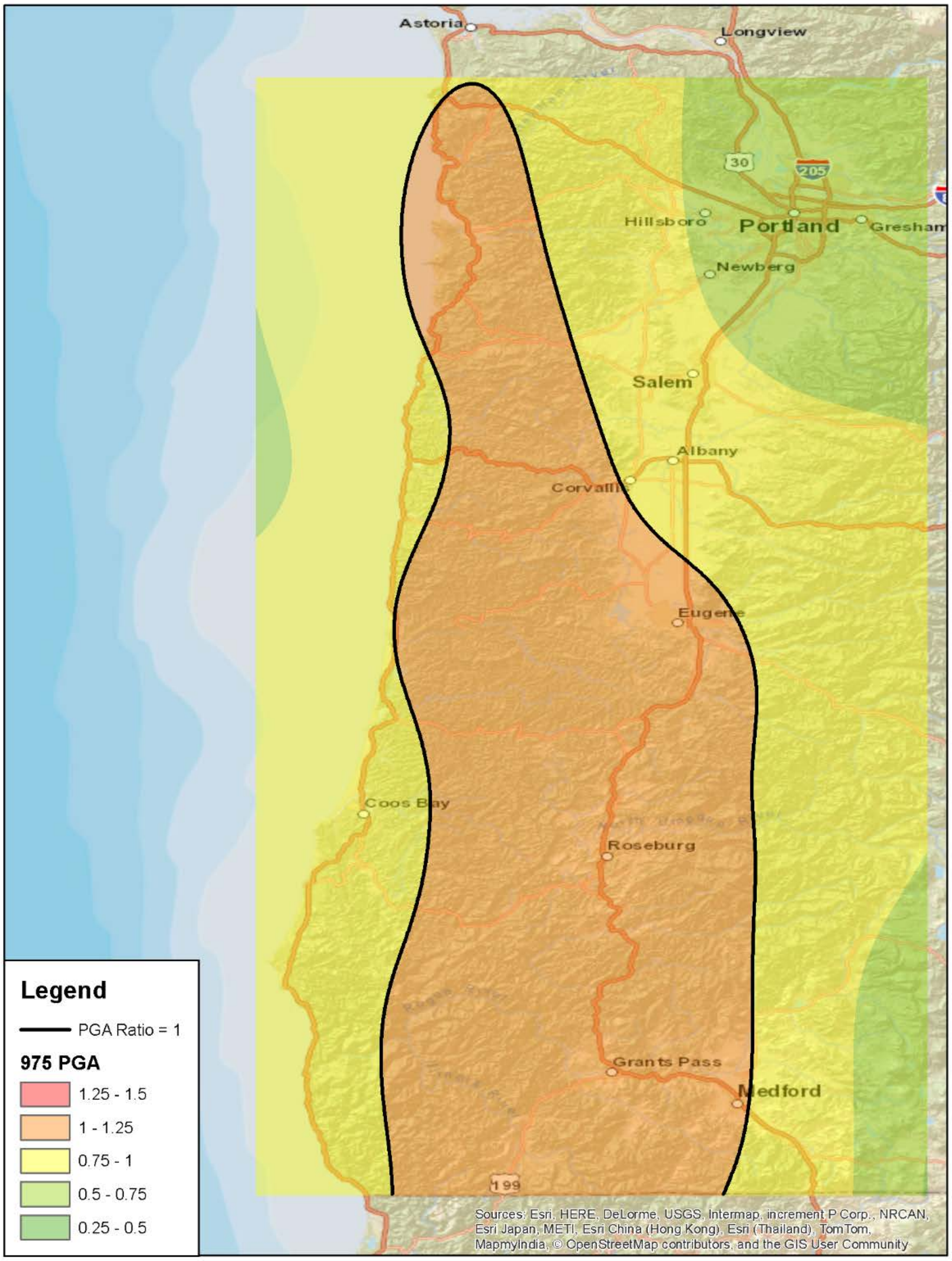

Sources: Esri, HERE, DeLorme, USGS, Intermap, increment P Corp., NRCAN, Esri Japan, METI, Esri China (Hong Kong), Esri (Thailand), TomTom, MapmyIndia, © OpenStreetMap contributors, and the GIS User Community

Figure A- 7: Ratio of 2002 D-DSHA and the 2002 UHS Maps for the peak ground acceleration and 975 year return period

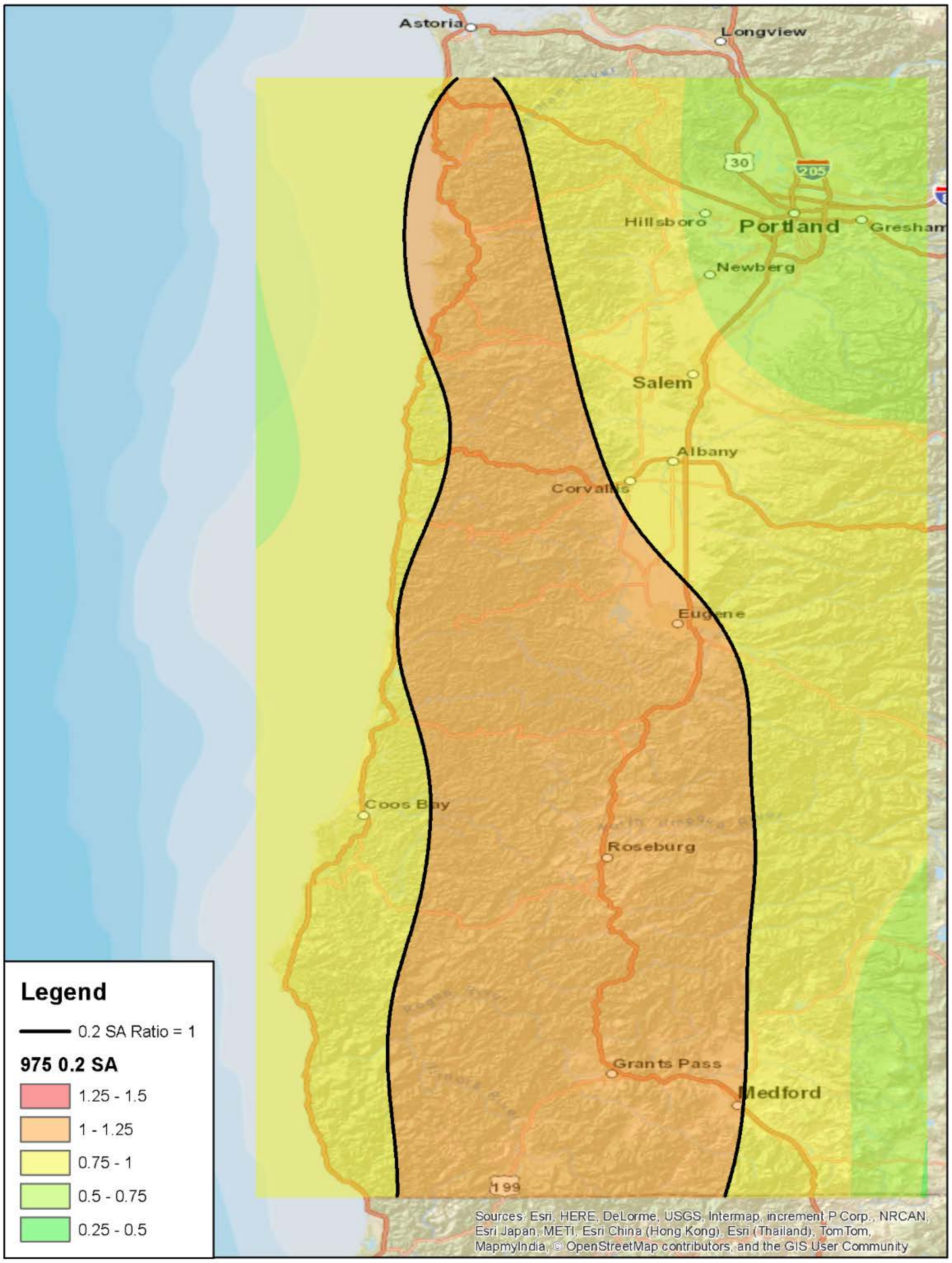

Sources: Esri, HERE, DeLorme, USGS, Intermap, increment P Corp., NRCAN, Esri Japan, METI, Esri China (Hong Kong), Esri (Thailand), TomTom, MapmyIndia, © OpenStreetMap contributors, and the GIS User Community

Figure A- 8: Ratio of 2002 D-DSHA and the 2002 UHS Maps for the 0.2 second spectral acceleration and 975 year return period

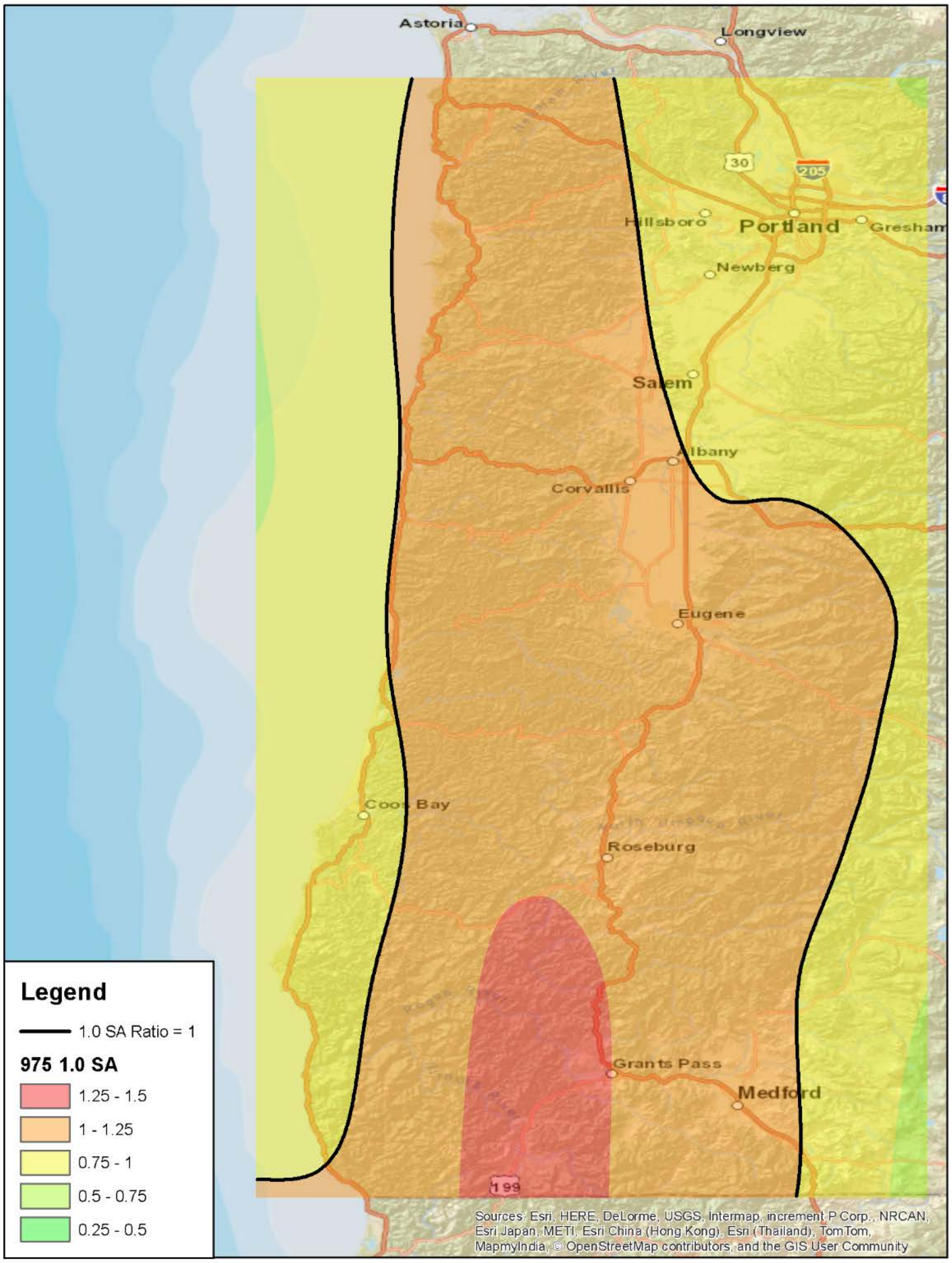

Figure A- 9: Ratio of 2002 D-DSHA and the 2002 UHS Maps for the 1.0 second spectral acceleration and 975 year return period

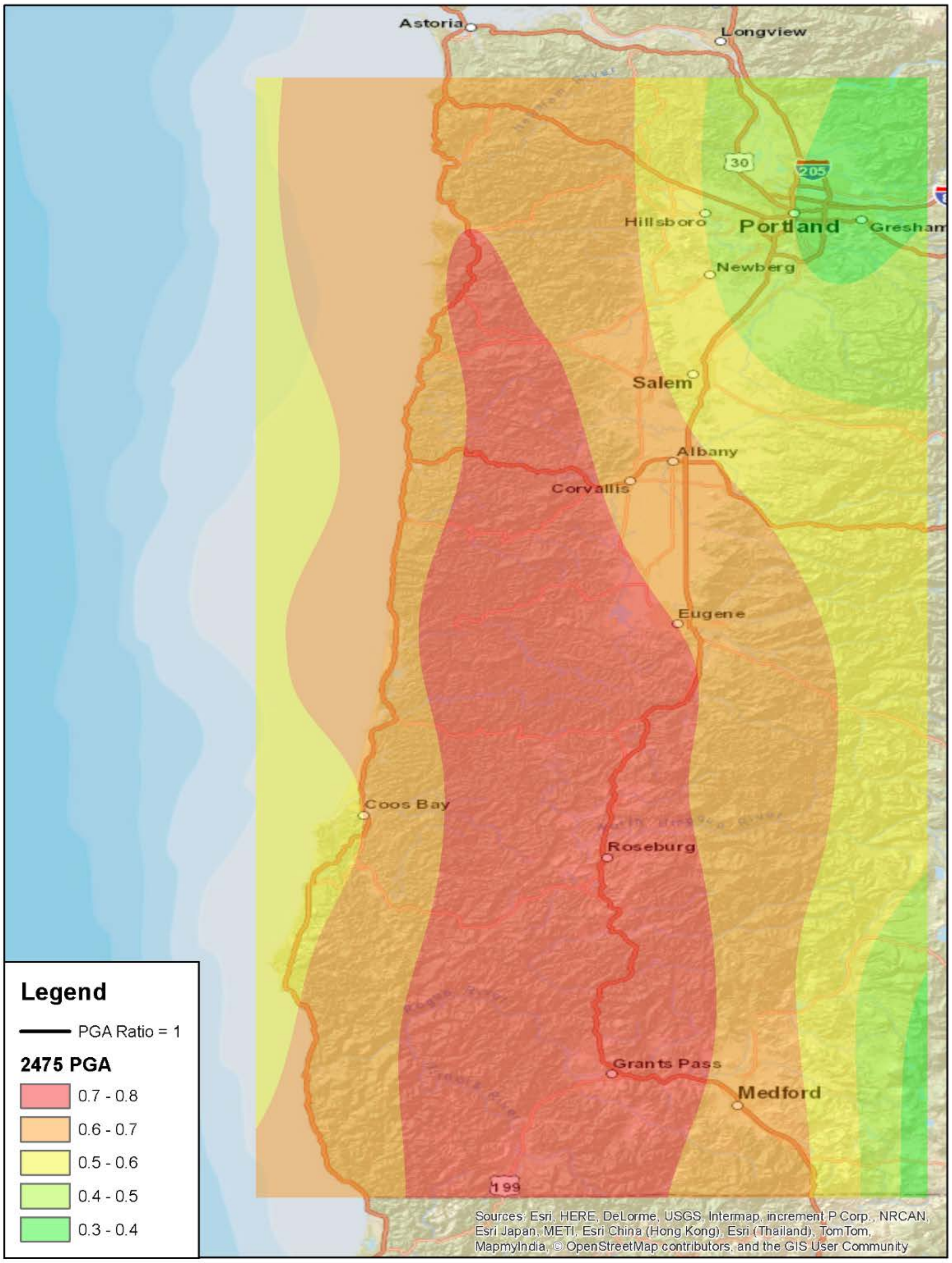

Sources: Esri, HERE, DeLorme, USGS, Intermap, increment P Corp., NRCAN, Esri Japan, METI, Esri China (Hong Kong), Esri (Thailand), TomTom, MapmyIndia, © OpenStreetMap contributors, and the GIS User Community

Figure A- 10: Ratio of 2002 D-DSHA and the 2002 UHS Maps for the peak ground acceleration and 2475 year return period

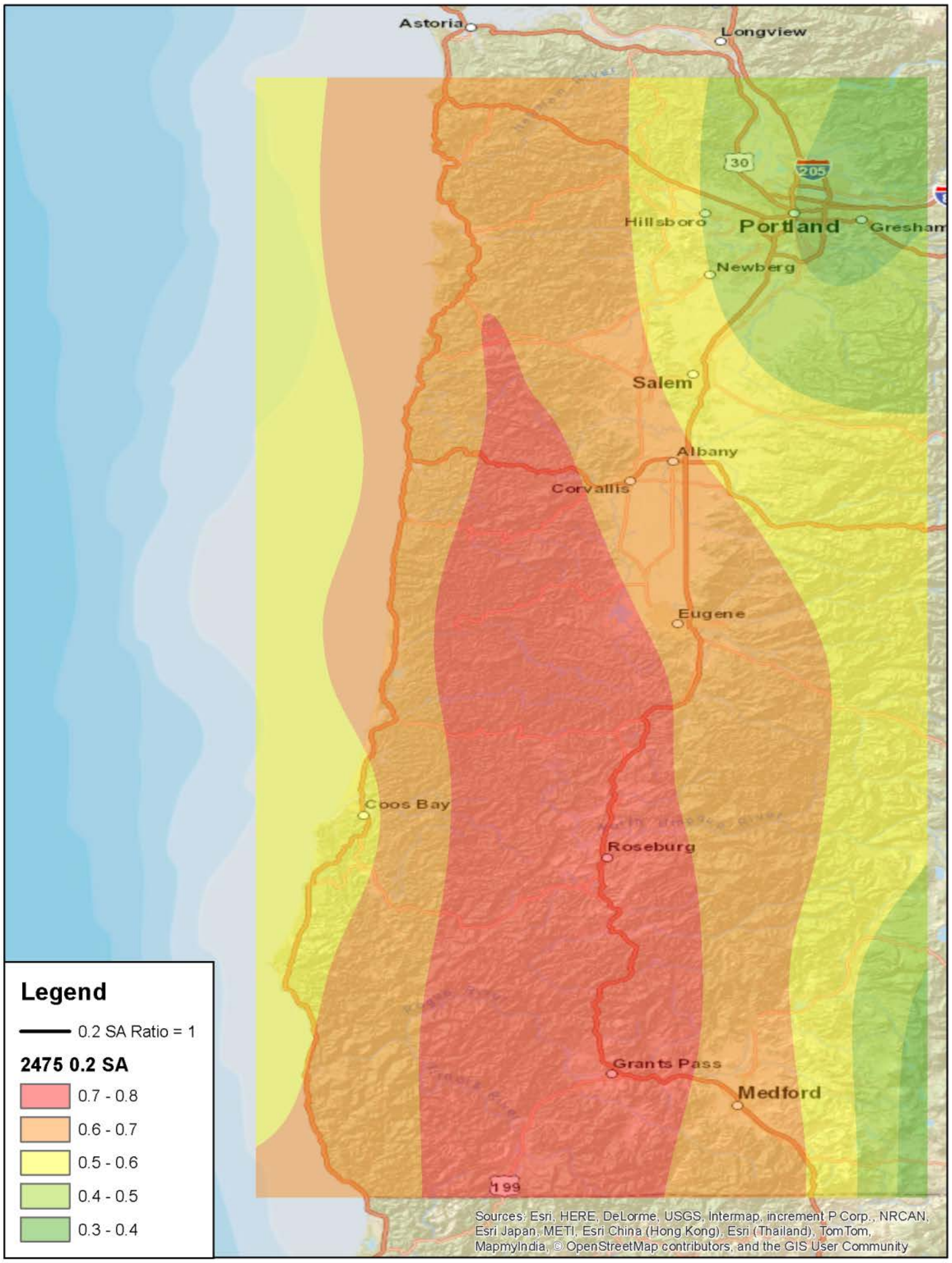

Figure A- 11: Ratio of 2002 D-DSHA and the 2002 UHS Maps for the 0.2 second spectral acceleration and 2475 year return period

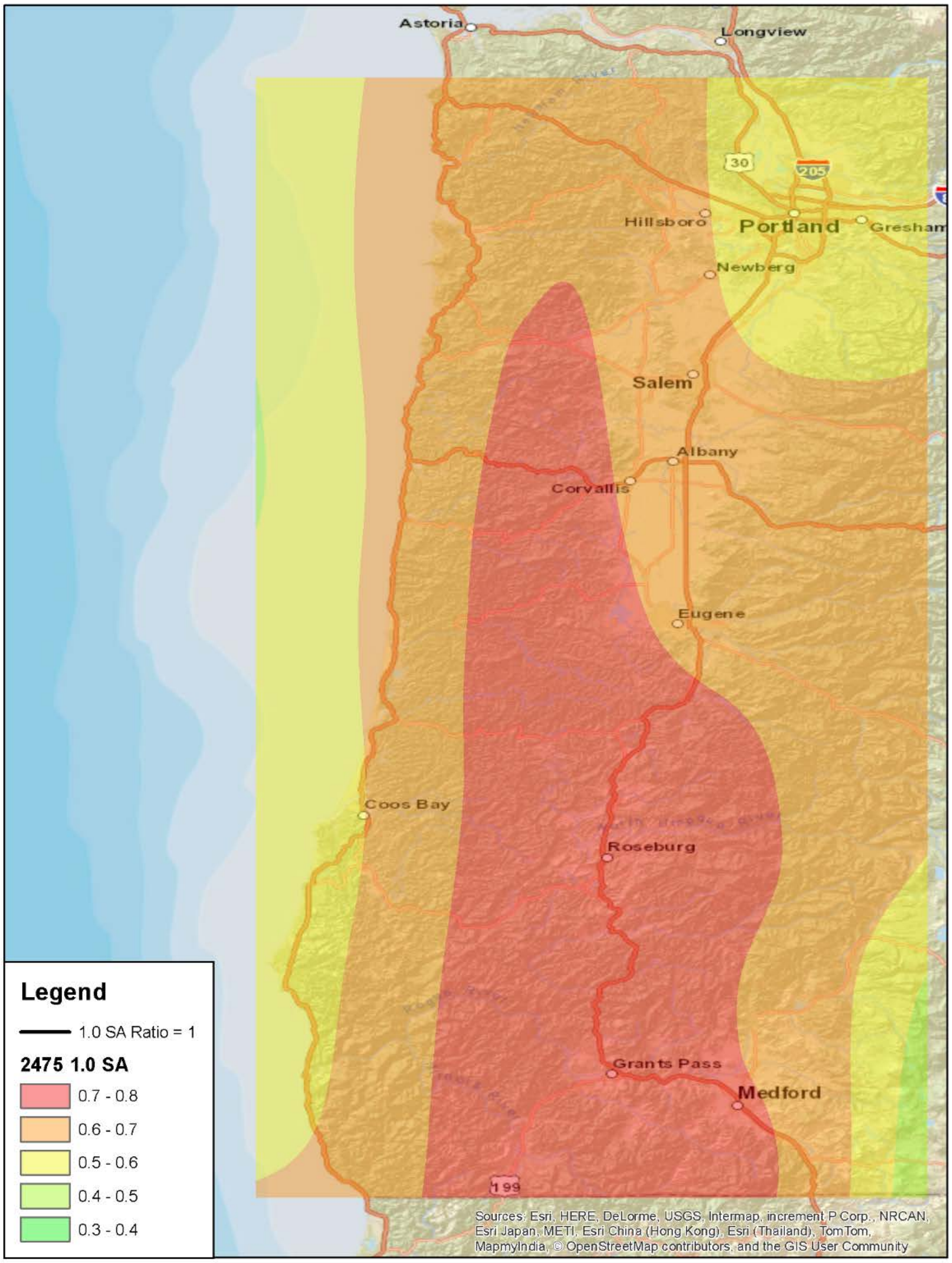

Sources: Esri, HERE, DeLorme, USGS, Intermap, increment P Corp., NRCAN, Esri Japan, METI, Esri China (Hong Kong), Esri (Thailand), TomTom, MapmyIndia, © OpenStreetMap contributors, and the GIS User Community

Figure A- 12: Ratio of 2002 D-DSHA and the 2002 UHS Maps for the 1.0 second spectral acceleration and 2475 year return period

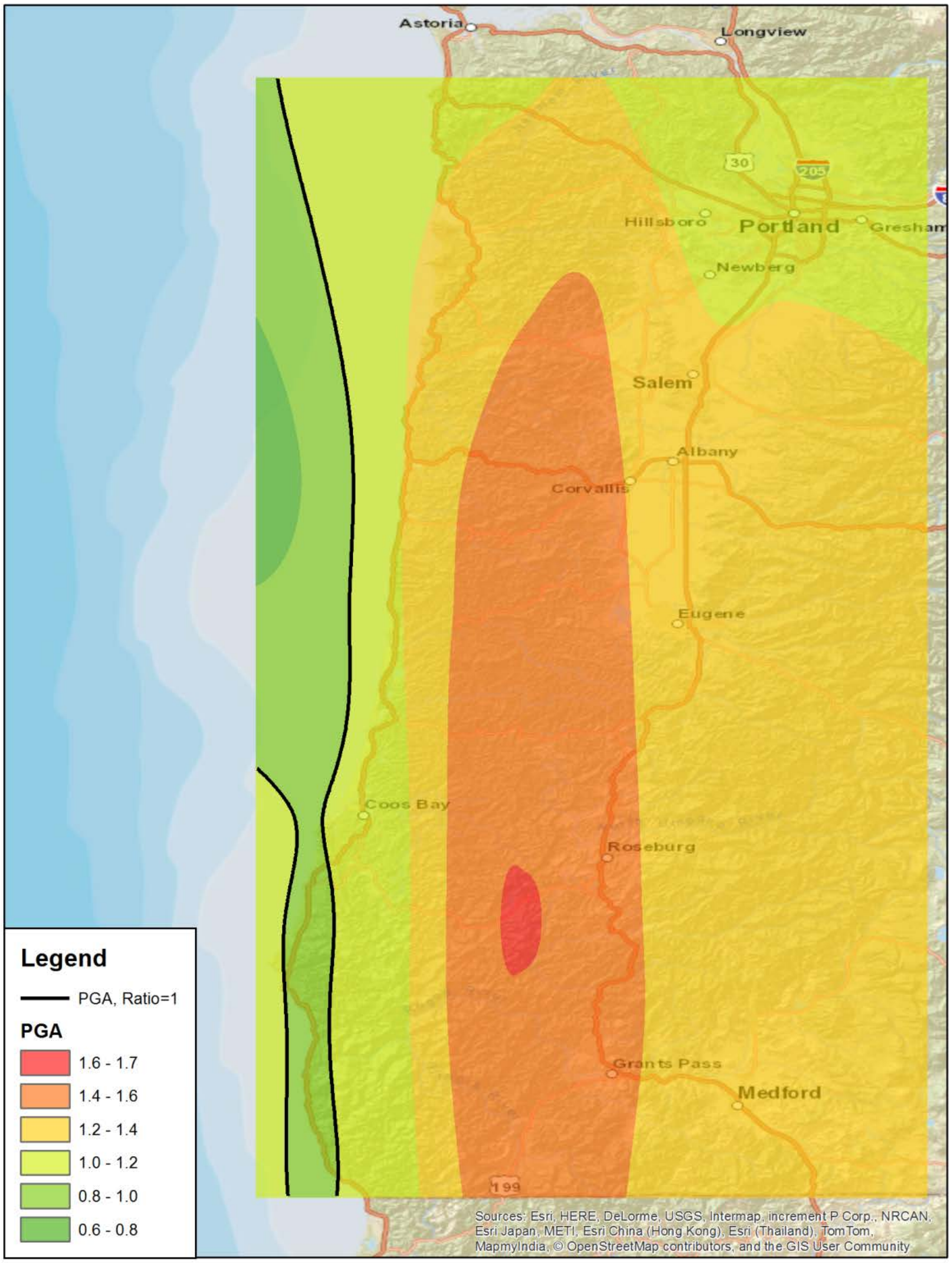

Figure A- 13: Ratio of 2002 D-DSHA accelerations to values from 2002 S-DSHA for PGA

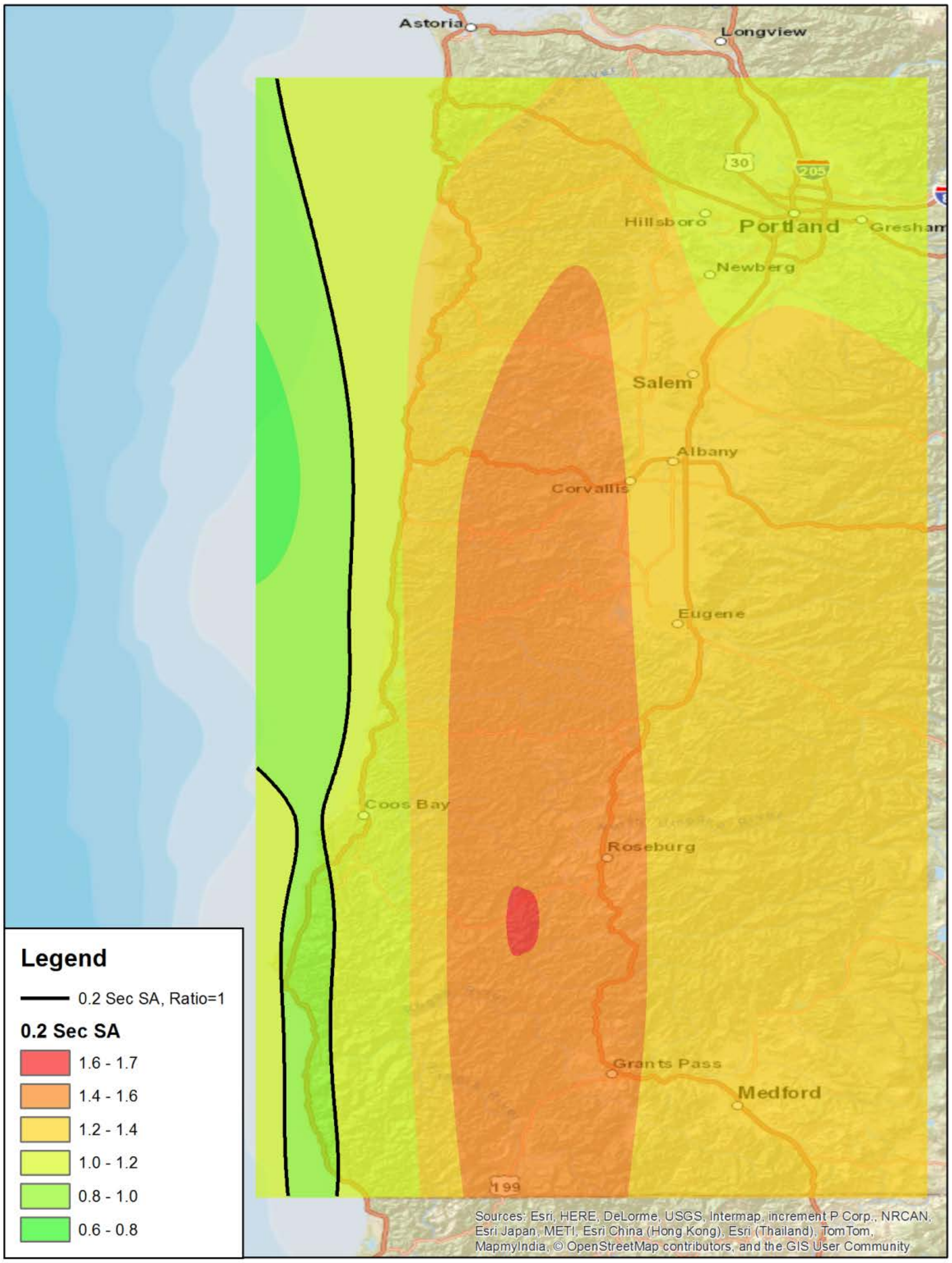

Sources: Esri, HERE, DeLorme, USGS, Intermap, increment P Corp., NRCAN, Esri Japan, METI, Esri China (Hong Kong), Esri (Thailand), TomTom, MapmyIndia, © OpenStreetMap contributors, and the GIS User Community

Figure A- 14: Ratio of 2002 D-DSHA accelerations to values from 2002 S-DSHA for 0.2 second spectral acceleration

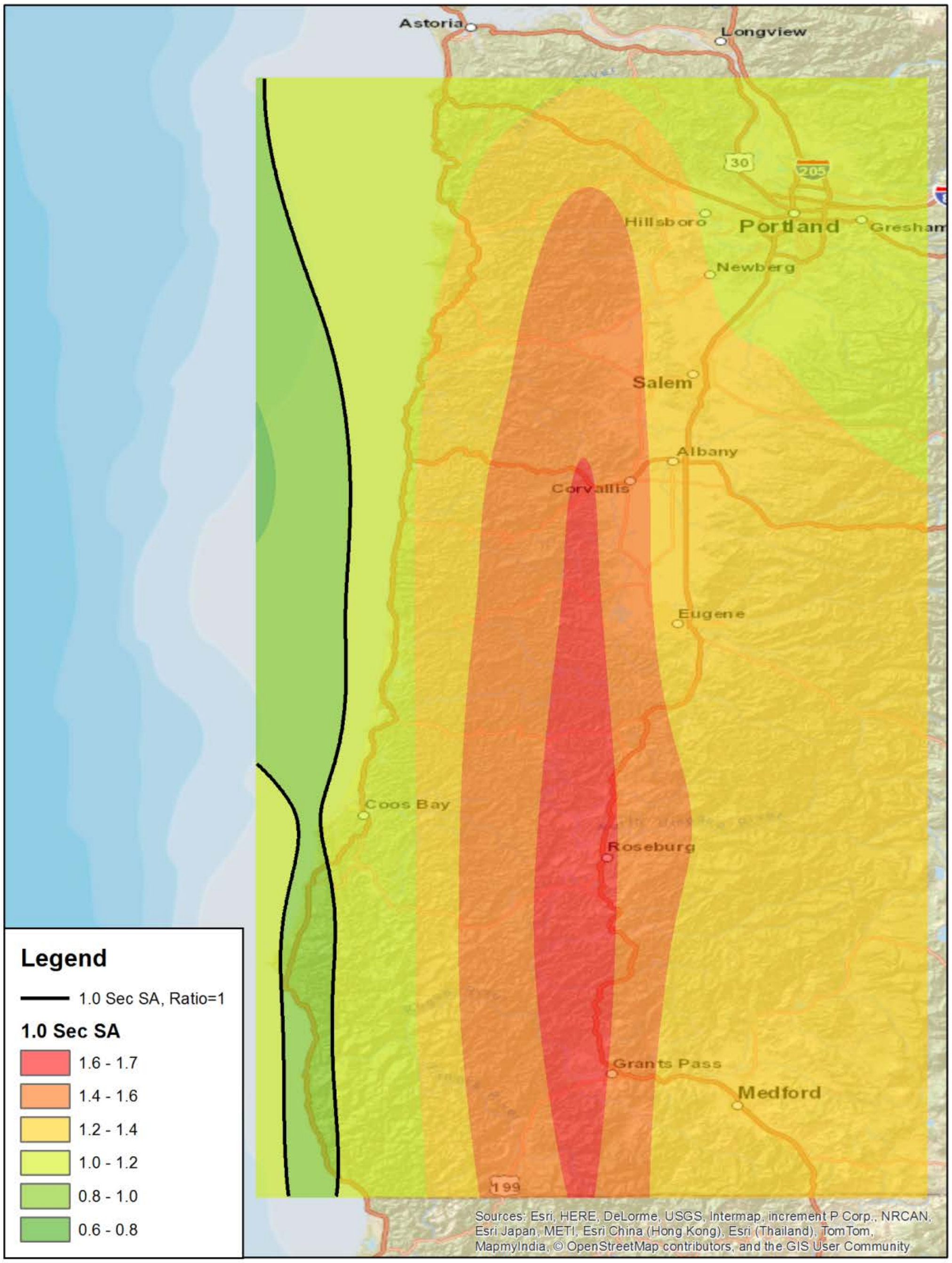

Figure A- 15: Ratio of 2002 D-DSHA accelerations to values from 2002 S-DSHA for 1.0 second spectral acceleration

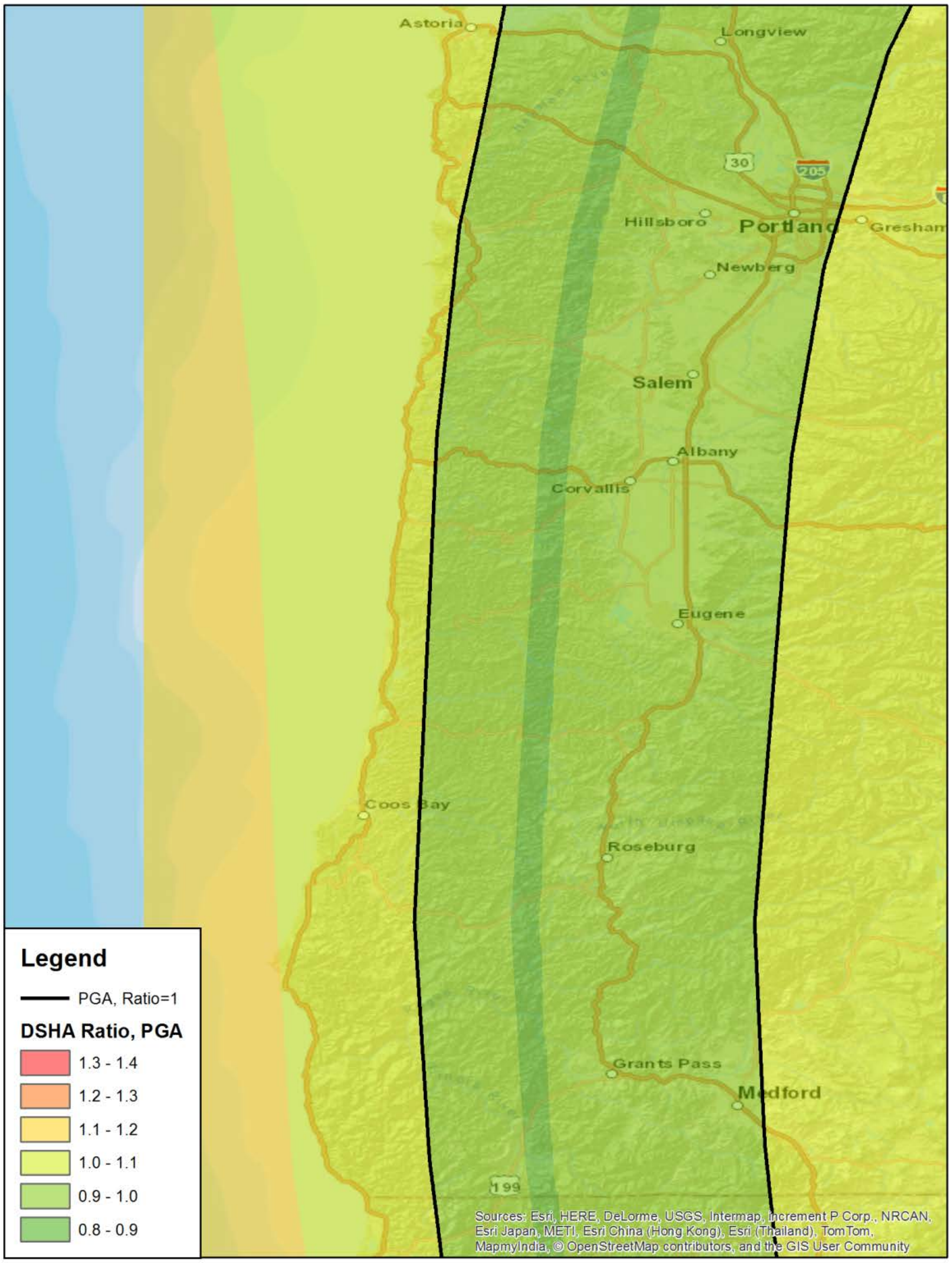

Figure A- 16: Ratio of 2002 S-DSHA to 2008 S-DSHA for CSZ, for PGA spectral acceleration

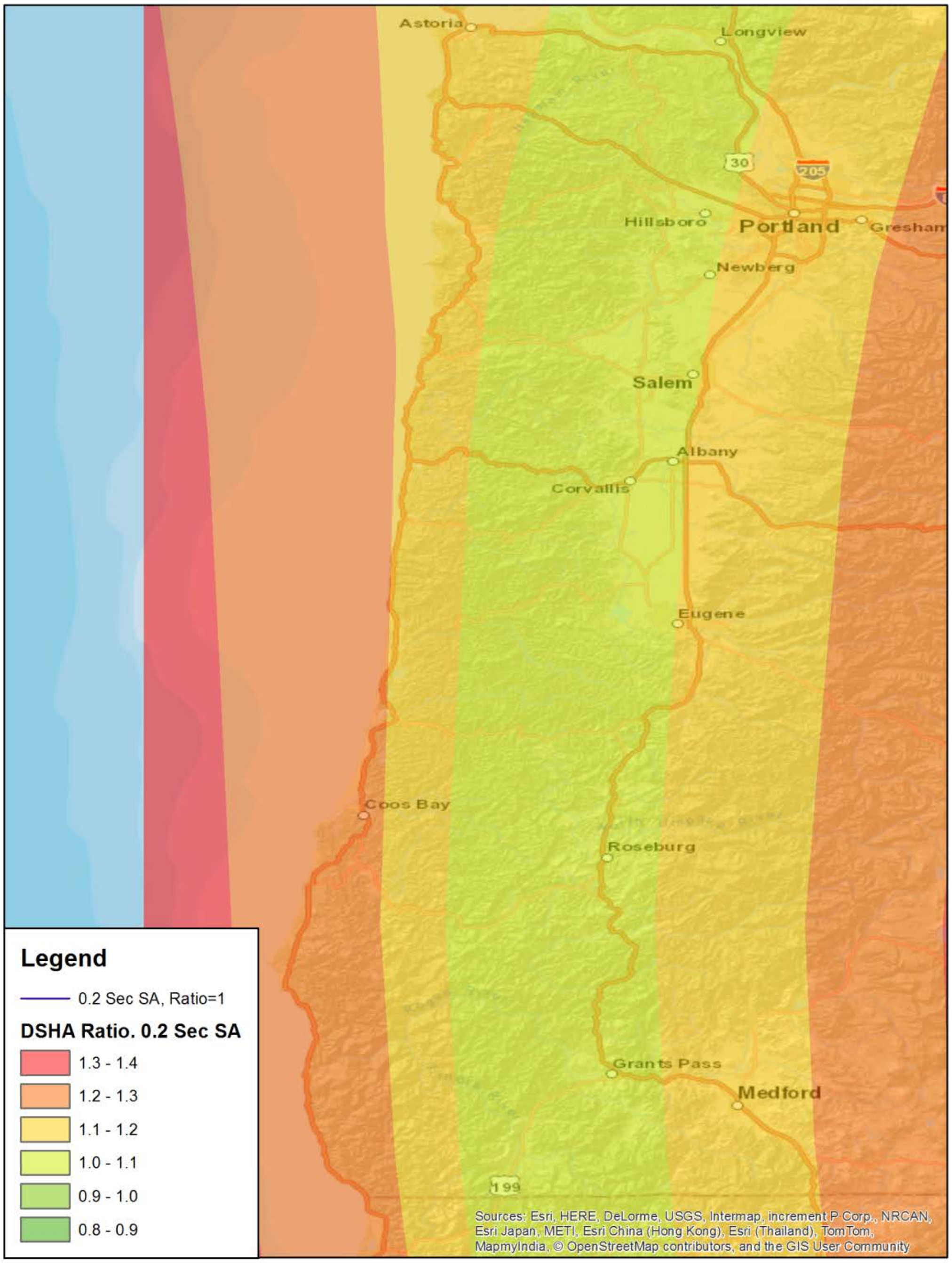

Figure A- 17: Ratio of 2002 S-DSHA to 2008 S-DSHA for CSZ, for 0.2 second spectral acceleration

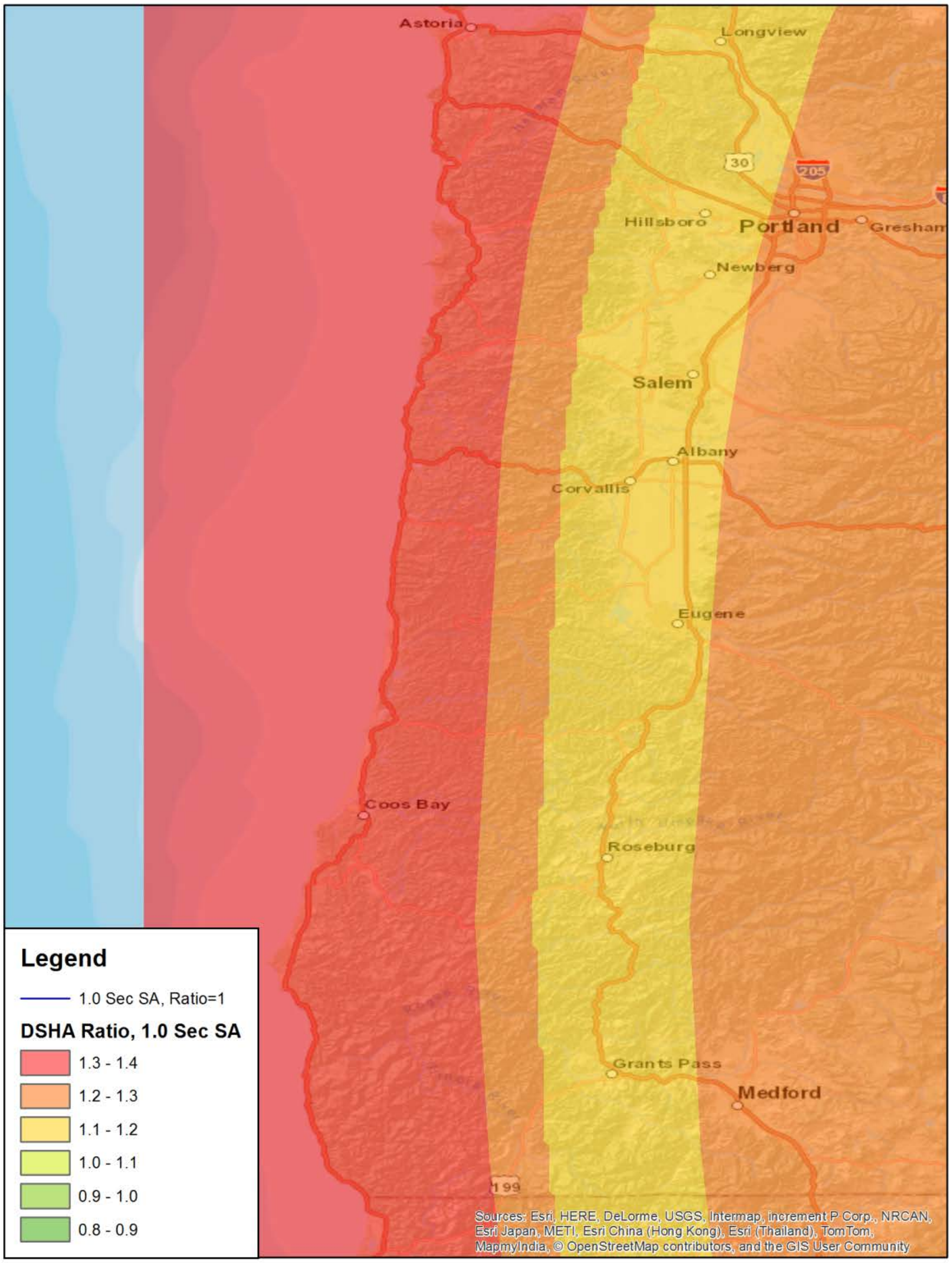

Figure A- 18: Ratio of 2002 S-DSHA to 2008 S-DSHA for CSZ, for 1.0 second spectral acceleration

APPENDIX B

ATTENUATION EQUATIONS USED IN CHAPTER 3

APPENDIX B

ATTENUATION EQUATIONS USED IN CHAPTER 3

Four interface attenuation models were used in this study: Atkinson and Boore (2003) global model, Zhao et al. (2006), Atkinson and Macias (2009), and BC Hydro (Addo, Abrahamson, & Youngs, 2012). The 2014 ground motion models for subduction interface earthquakes and their respective weights are given in Table 1.

Table B- 1: Subduction interface ground motion models and their corresponding weight

Interface Ground Motion Model	**Weight**
Atkinson and Boore (2003) global model	0.1
Zhao and others (2006)	0.3
Atkinson and Macias (2009)	0.3
BC Hydro (Addo and others, 2012)	0.3

Atkinson and Boore Attenuation Model (2003)

The attenuation equation by Atkinson and Boore was developed to predict the peak ground motion acceleration for subduction zone interface and in-slab earthquakes of magnitudes equal to or greater than 8Mw. The Atkinson and Boore equation was based on a maximum likelihood regression analysis of a response spectra database from thousands of strong-motion recordings from events of moment magnitude 5 – 8.3 occurring in subduction zones around the world. This included both interface and in-slab events (Atkinson and Boore, 2003). The 5% damped pseudo acceleration was given as a function of the moment magnitude, the focal depth, the closest source-to-site distance, geometric spreading, rock/soil response, and several regression coefficients that were each a function of a given frequency.

$$\log(y) = fn(M) + c_3 h + c_4 R - g\ log(R) + c_5\ sl\ S_C + c_6\ sl\ S_D + c_7\ sl\ S_E$$

$$fn(M) = c_1 + c_2\ M$$

$$R = \sqrt{{D_{fault}}^2 + \Delta^2}$$

$$\Delta = 0.00724\ x\ 10^{0.507M}$$

Y = 5% damped spectral acceleration in cm/sec^2
M = Moment magnitude
H = Focal depth in km
D_{fault} = Closest distance to fault surface in km
g = $10^{(1.2 - 0.18M)}$ for interface events, = $10^{(0.301 - 0.01M)}$ for in-slab events (geometrical spreading coefficient)

S_C = 1 for NEHRP C soils ($360 < \beta \leq 760$ m/sec), = 0 otherwise

S_D = 1 for NEHRP D soils ($180 \leq \beta \leq 360$ m/sec), = 0 otherwise
S_E = 1 for NEHRP E soils ($\beta < 180$ m/sec), = 0 otherwise

sl = 1. For $PGA_{rx} \leq 100$ cm/sec^2 or frequencies ≤ 1 Hz
sl = 1. – (f – 1) (PGA_{rx} – 100.)/400. For $100 < PGA_{rx} < 500$ cm/sec^2 (1 Hz <f < 2 Hz)
sl = 1. – (f – 1) for $PGA_{rx} \geq 500$ cm/sec^2 (1 Hz < f < 2 Hz)
sl = 1. – (PGA_{rx} – 100.)/400. For $100 < PGA_{rx} < 500$ cm/sec^2 (f ≥ 2 Hz and PGA)
sl = 0 for $PGA_{rx} \geq 500$ cm/sec^2 (f ≥ 2 Hz and PGA);
PGA_{rx} is predicted PGA on rock (NEHRP B) in cm/sec^2

When this attenuation equation was used in the study, two noteworthy assumptions were made in order to have a meaningful comparison to the USGS' data. First, an interface event was assumed, which meant choosing the appropriate geometrical spreading (g) formula. Second, the log average between the acceleration values for B and C site conditions was used as the final ground motion value.

Zhao et al. Attenuation Equation (2006)

The attenuation equation by Zhao et al. was developed to predict spectral accelerations for subduction zone crustal, interface, and in-slab earthquakes. The Zhao et al. equation was based on a regression analysis of strong-motion data collected from thousands of recordings from subduction zones located in Japan, Iran, and the western United States. The Zhao et al. attenuation model related the 5% damped acceleration response as a function of the moment magnitude, focal depth, source distance, faulting mechanism, tectonic source type, site class, and several regression coefficients that are each a function of a given period.

$$log_e(y_{i,j}) = aM_{wi} + bx_{i,j} - log_e(r_{i,j}) + e(h - h_c)\delta_h + F_R + S_I + S_S + S_{SL}log_e(x_{i,j}) + C_k$$

$$r_{i,j} = x_{i,j} + c\ exp^{(dM_{wi})}$$

Y = 5% damped spectral acceleration in cm/sec^2
M_w = Moment magnitude
x = Source distance in km
h = Focal depth in km
C_k = the site-class term for a given site class
F_R = Reverse-fault parameter (only applies to crustal events with a reverse-faulting mechanism and is zero for all other events)
S_I = the tectonic source type parameter (only applies to interface events and is zero for all other type events)
S_S = the tectonic source type parameter (only applies to subduction slab events only and is zero for all other type events)
S_{SL} = a magnitude-independent path modification term for slab events to account for the complex seismic wave travel path for slab events

h_c = depth constant (when h is larger than h_c, the depth term $e(h - h_c)$ takes effect, with δ_h being a dummy variable that equals 0 for $h<h_c$ and 1 for $h \geq h_c$. When h is larger than 125 km, h = 125 km is selected so that a constant factor is used for deeper earthquakes - i.e., depth is capped at 125 km.

Three assumptions were made in the use of this equation, which were worth noting. First, an interface event was assumed which meant that the reverse-fault parameter, tectonic source type parameter, and magnitude path modification term were set to zero. Second, two terms of the attenuation model were neglected for this study: the intra-event error ($\xi_{i,j}$) and the interevent error (η_i). Both terms were used for a regression analysis of the coefficients that was used to develop the attenuation model. Regression analysis was not relevant to the study, thus, the terms were not included when using this attenuation equation. Finally, a shear wave velocity of 760 m/s was assumed given its uniform application for the USGS hazard maps.

Atkinson and Macias Attenuation Equation (2009)

The attenuation equation by Atkinson and Macias was developed to predict spectral accelerations for subduction zone interface earthquakes in the Cascadia subduction zone. This attenuation model was based off simulation results of a stochastic finite-fault model developed by Motazedian and Atkinson (2005). The Atkinson and Macias attenuation model related the 5% damped acceleration response as a function of moment magnitude, the closest distance to the fault, and several coefficients that were each a function of a given frequency.

$$log\, Y = \sum C_i E_i + C_1 log(R) + C_2 R$$

$$C_i = C_0 + C_3(M - 8) + C_4(M - 8)^2$$

$$R = \sqrt{(R^2{}_{cd} + h^2)}$$

$$h = M^2 - 3.1M - 14.55$$

Y = 5% damped spectral acceleration in cm/sec^2
E_i = Dummy variable that has the value of 1 for earthquake i or 0 otherwise
R_{cd} = Closest distance to fault
h = Near-source saturation term determined to provide the best fit to the shape for locations close to the fault plane

BC Hydro Attenuation Equation **(2012)**

The attenuation equation by BC Hydro was developed to predict peak spectral accelerations for subduction zone interface and in-slab earthquakes. The BC Hydro equation was based on a regression analysis of a global dataset of empirical strong motion data from previous and more recent subduction zone earthquakes. The 5% damped pseudo acceleration was given as a function of moment magnitude, hypocentral depth, rupture distance, site type, median PGA, and several regression coefficients that were each a function of a given period.

$$\begin{aligned}\ln(Sa) = \theta_1 + \theta_2 * \Delta C_1 + \left(\theta_2 + \theta_{14} * F_{event} + \theta_3 * (M - 7.8)\right) \\ * \ln(R + C_4 * \exp[(M - 6) * \theta_9]) + \theta_6 * R + \theta_{10} * F_{event} + f_{Mag}(M) \\ + f_{depth}(Z_h) + f_{FABA}(R) + f_{site}(PGA_{1000}, V_{S30})\end{aligned}$$

Where:

M = Moment magnitude
Z_h = Hypocentral depth in km

$$R = \begin{cases} Rupture\ Distance & for\ Interface\ Events \\ Hypocentral\ Distance & for\ Instralab\ Events \end{cases}$$

$$F_{event} = \begin{cases} 0 & Interface\ Events \\ 1 & Instralab\ Events \end{cases}$$

$$F_{FABA} = \begin{cases} 0 & Forearc\ or\ Unknown\ Sites \\ 1 & Backarc\ Sites \end{cases}$$

Base Model for Magnitude Scaling:

$$f_{Mag}(M) = \begin{cases} \theta_4 * \left(M - (C_1 + \Delta C_1)\right) + \theta_{13} * (10 - M)^2 & for\ M \leq\ C_1 + \Delta C_1 \\ \theta_5 * \left(M - (C_1 + \Delta C_1)\right) + \theta_{13} * (10 - M)^2 & for\ M >\ C_1 + \Delta C_1 \end{cases}$$

Where:

C_1 = 7.8. Values of ΔC_1 capture the epistemic uncertainty in the break in the magnitude scaling.

Base Model for Depth Scaling:

$$f_{depth}(Z_h) = \theta_{11} * (Z_h - 60) * F_{event}$$

Base Model for Forearc/Backarc Scaling:

$$f_{FABA}(R) = \begin{cases} \left[\theta_7 + \theta_8 * Ln\left(\frac{max\left[R_{hypo}, 85\right]}{40}\right)\right] * F_{FABA} & for\ F_{event} = 1 \\ \left[\theta_{15} + \theta_{16} * Ln\left(\frac{max\left[R_{rup}, 100\right]}{40}\right)\right] * F_{FABA} & for\ F_{event} = 0 \end{cases}$$

Base Model for Site Response:

$$f_{site}(PGA_{1000}, V_{S30m}) = \begin{cases} \theta_{12} * Ln\left(\frac{V_S^*}{V_{lin}}\right) - b * Ln(PGA_{1000} + c) + & \\ b * Ln\left(PGA_{1000} + c * \left(\frac{V_S^*}{V_{lin}}\right)^n\right) & for\ V_{S30} < V_{lin} \\ \theta_{12} * Ln\left(\frac{V_S^*}{V_{lin}}\right) + b * n * Ln\left(\frac{V_S^*}{V_{lin}}\right) & for\ V_{S30} \geq V_{lin} \end{cases}$$

Where:

PGA_{1000} = Median PGA value for V_{S30} = 1,000 m/sec and,

$$V_S^* = \begin{cases} 1000.0 & for\ V_{S30} > 1000 \\ V_{S30} & for\ V_{S30} \leq 1000 \end{cases}$$

When this attenuation equation was used for this study, three assumptions were made which were worth noting. First, an interface event was assumed which influenced scaling factors for the attenuation equation. Second, every rupture distance was considered unknown. This assumption was made because no information was provided in BC Hydro's report regarding forearc/backarc distances for the Pacific Northwest. Finally, a shear wave velocity of 760 m/s was assumed after using a shear velocity of 1000 m/s to find the median PGA (PGA_{1000}). This velocity was assumed given its uniform application for the USGS hazard maps.

APPENDIX C

DISTANCE CALCULATIONS FOR THE 14CSZ MODEL

APPENDIX C

DISTANCE CALCULATIONS FOR THE 14CSZ MODEL

In order to calculate the distance from any of the 18,511 longitude-latitude points in the rectangular grid that defines the state of Oregon, a MATLAB script was developed. This MATLAB script can be divided in four main parts, and each part is explained below.

The first part of the script was written with the aim of creating the grids that define each fault rupture surface. This was accomplished by converting the latitude and longitude coordinates of the up-dip edge and the three down-dip edges of the fault zones into an X-Y UTM system of coordinates. Then, each fault rupture zone, which is defined by the up-dip edge and one down-dip edge, was characterized by creating further lines between edges and then dividing such lines to create a fine grid of the fault surface.

The second part of the script had the objective of performing a Delaunay triangulation of the entire grid. This triangulation was performed using a built-in function in MATLAB.

The third part was performed similarly to the first part with the aim of converting the previously defined grid points (18,511 point) to an X-Y system of coordinates.

The final part of the code performed the distance calculation itself by taking advantage of the built-in function “Nearest Neighbor”, which is commonly used in spatial searching (MATLAB 8.5 2015).

APPENDIX D

RESULTS FROM 14CSZ MODEL

APPENDIX D

RESULTS FROM 14CSZ MODEL

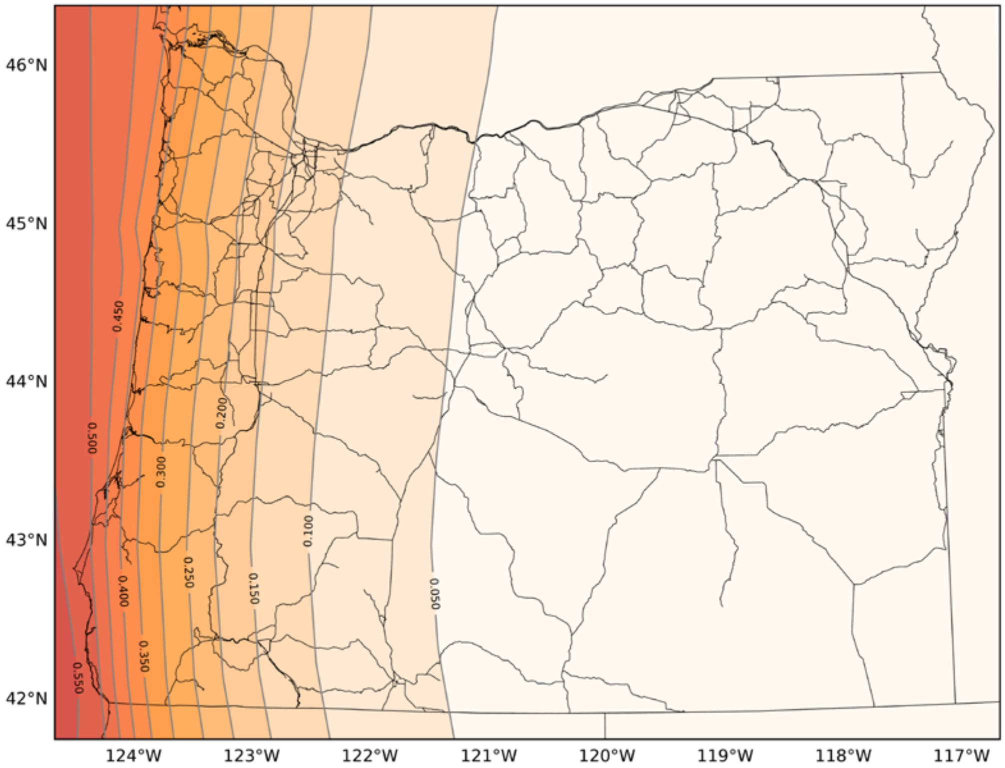

Figure D- 1: The 14CSZ PGA values

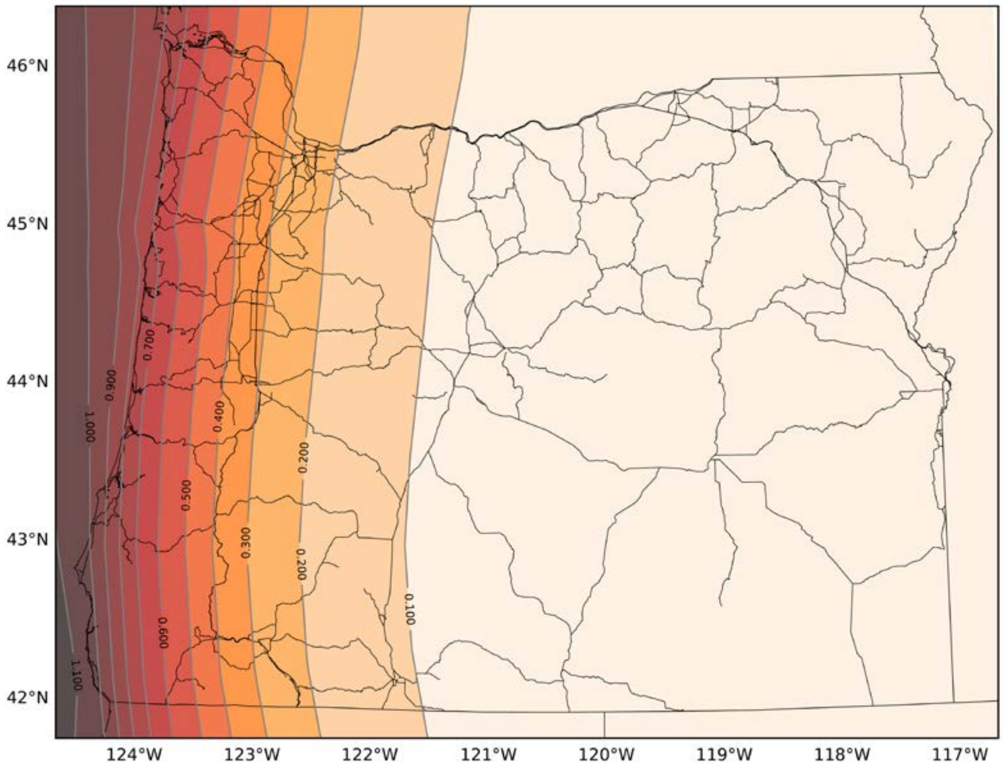

Figure D- 2: The 14CSZ 0.2 second values

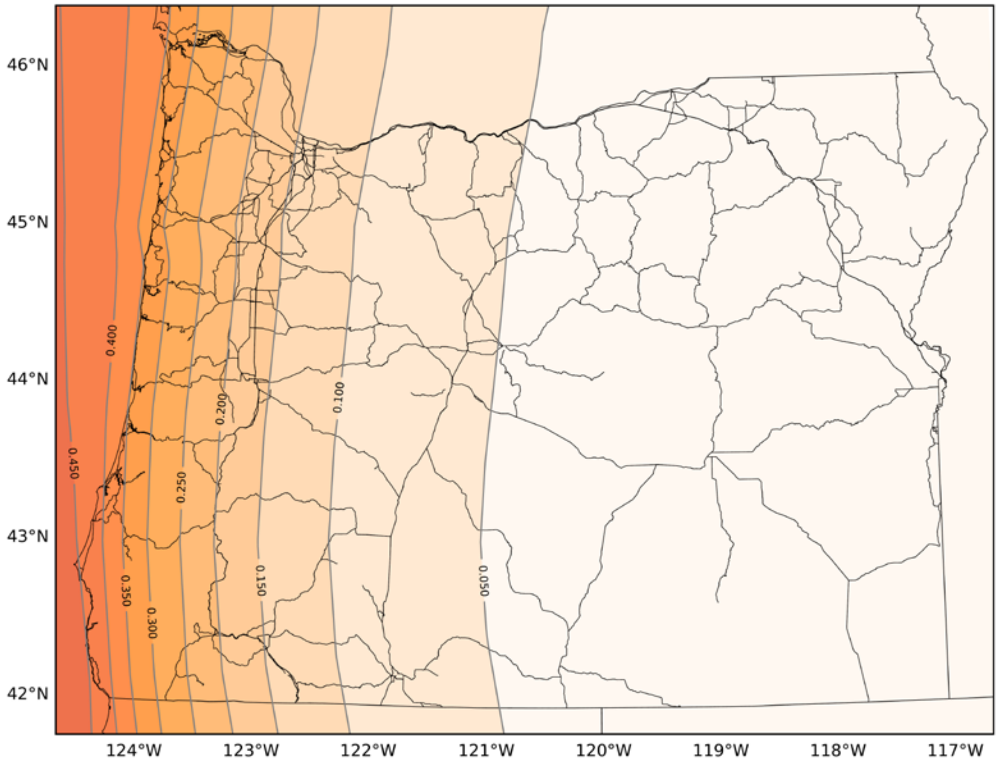

Figure D- 3: The 14CSZ 1.0 second values

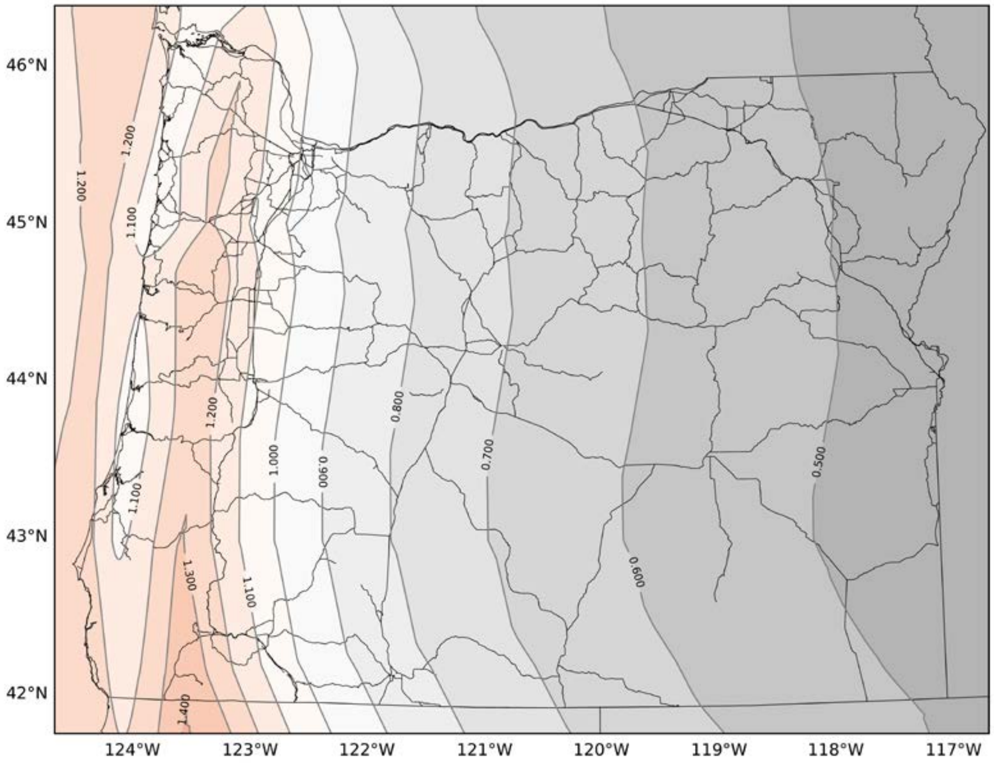

Figure D- 4: 14CSZ vs.02CSZ for PGA

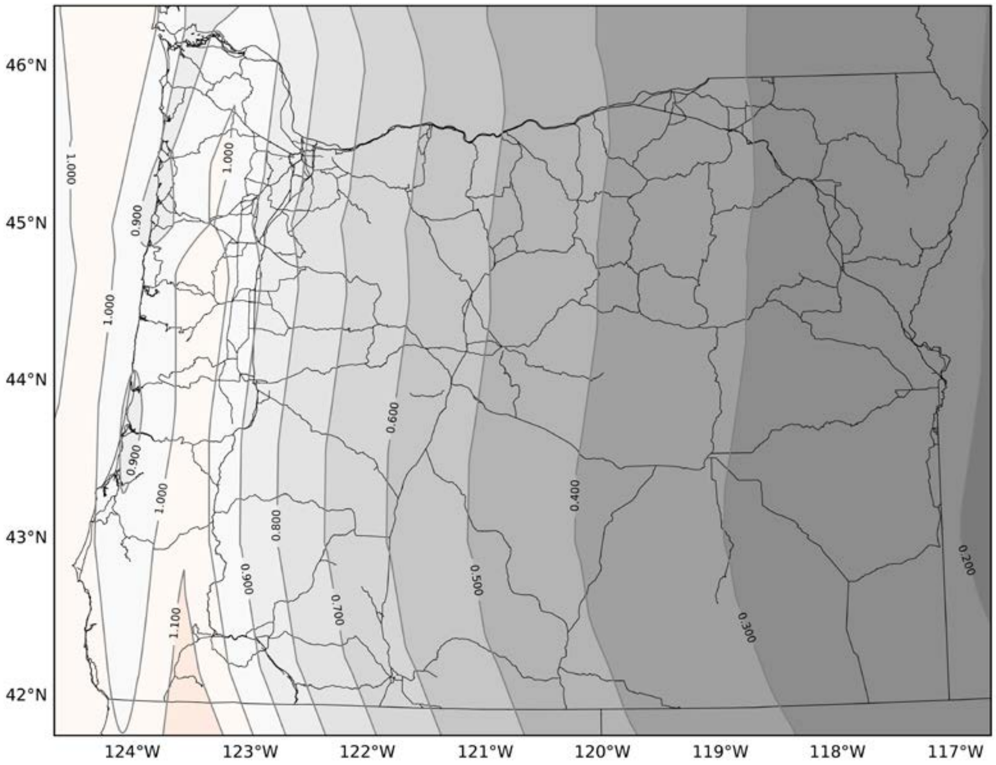

Figure D- 5: 14CSZ vs.02CSZ for 0.2 second

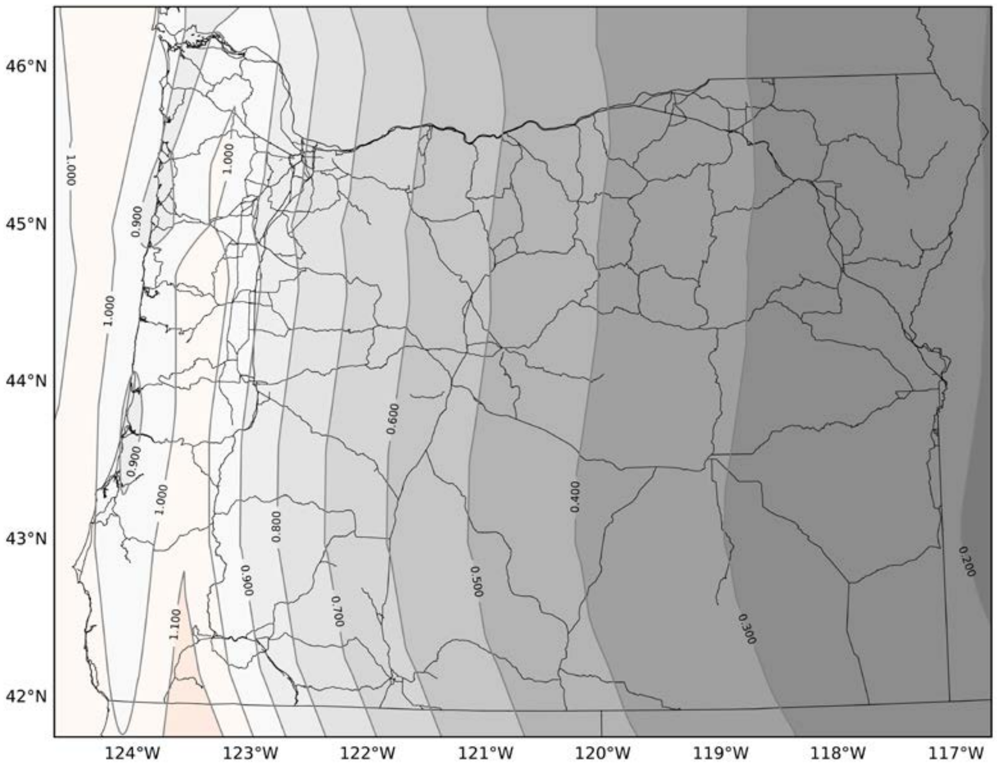

Figure D- 6: 14CSZ vs. 02CSZ for 1.0s

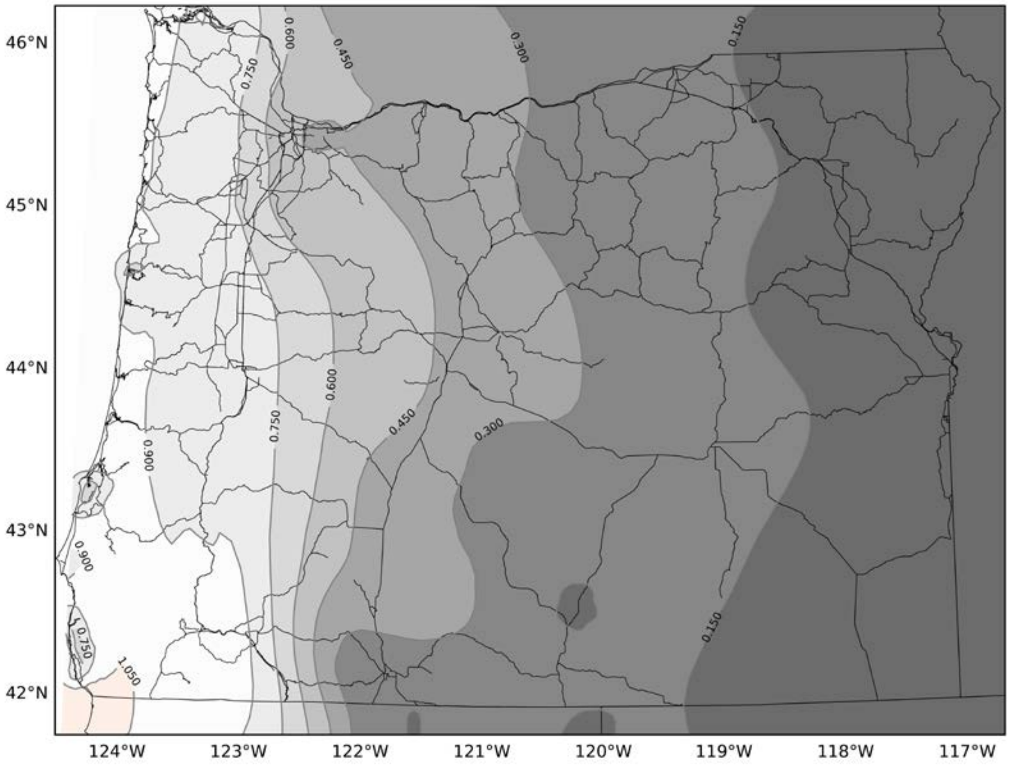

Figure D- 7: 14CSZ vs. 02PSH1000 for PGA

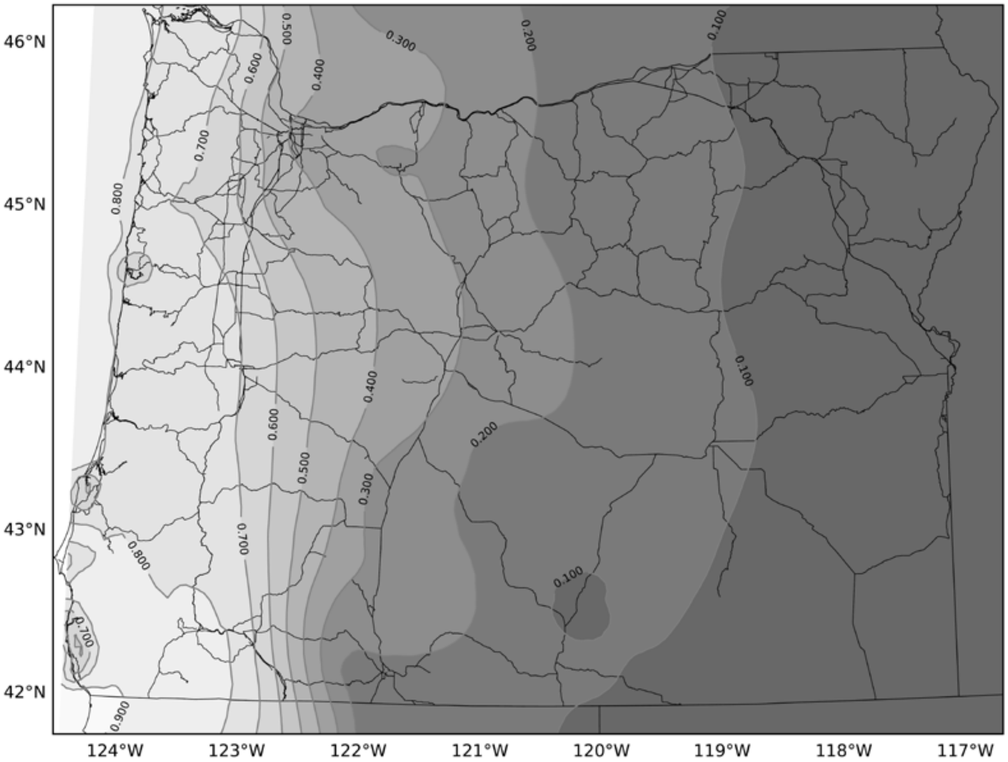

Figure D- 8: 14CSZ vs. 02PSH1000 for 0.2s

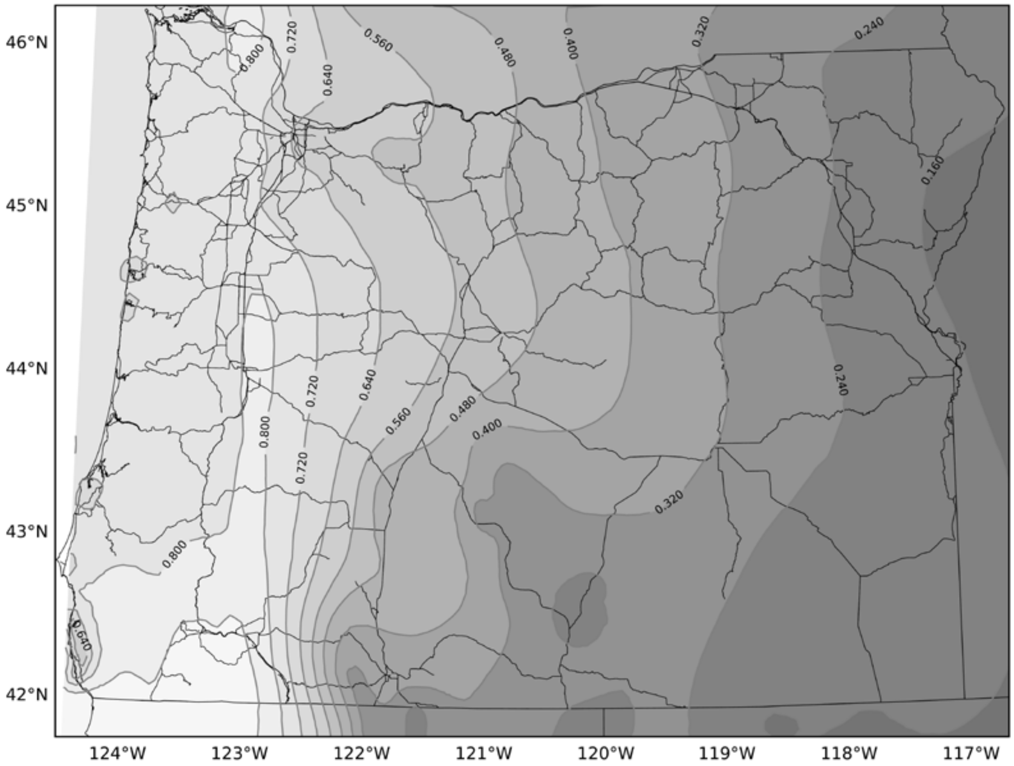

Figure D- 9: 14CSZ vs. 02PSH1000 for 1.0s

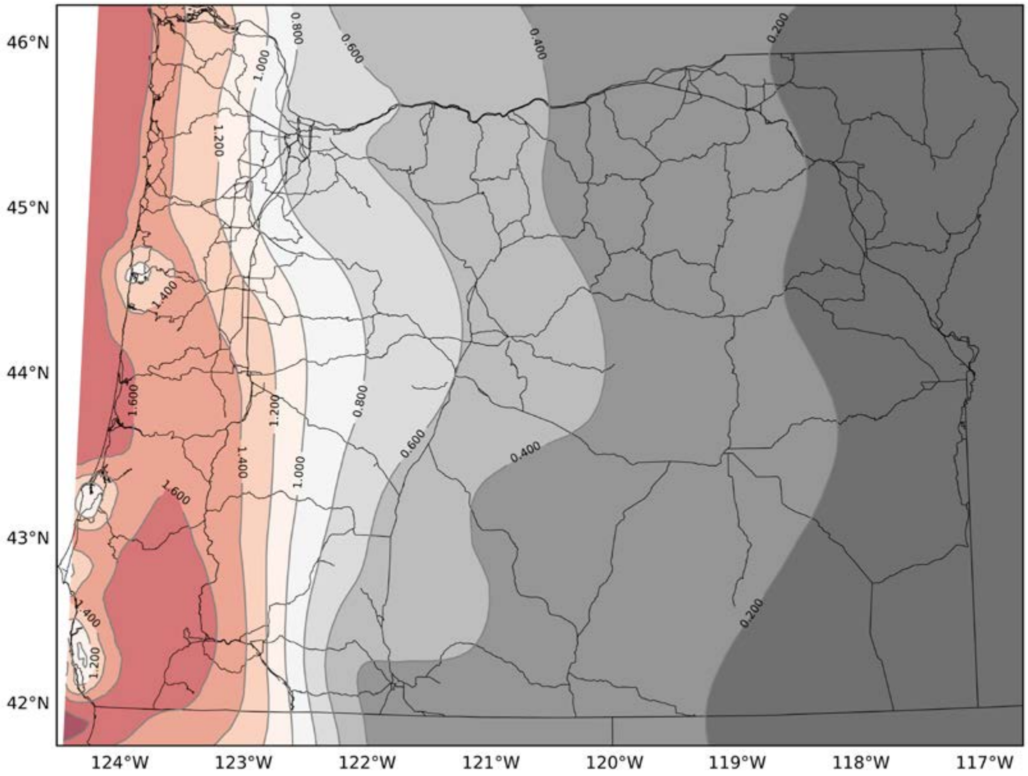

Figure D- 10: 14CSZ vs. 02PSH500 for PGA

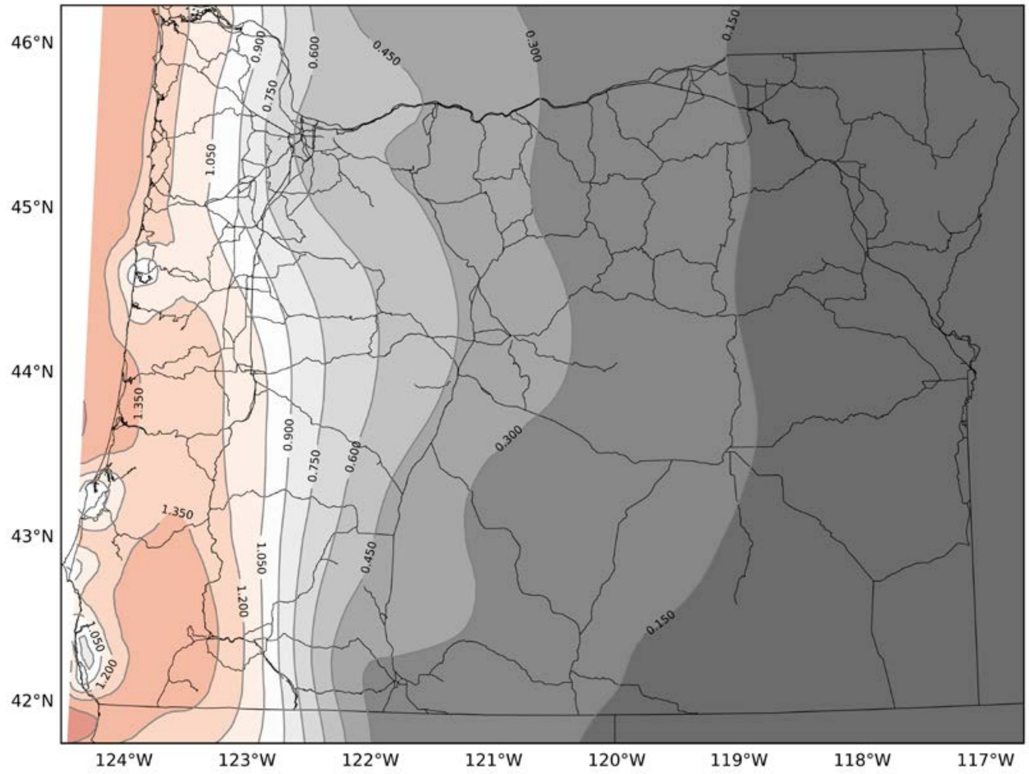

Figure D- 11: 14CSZ vs. 02PSH500 for 0.2s

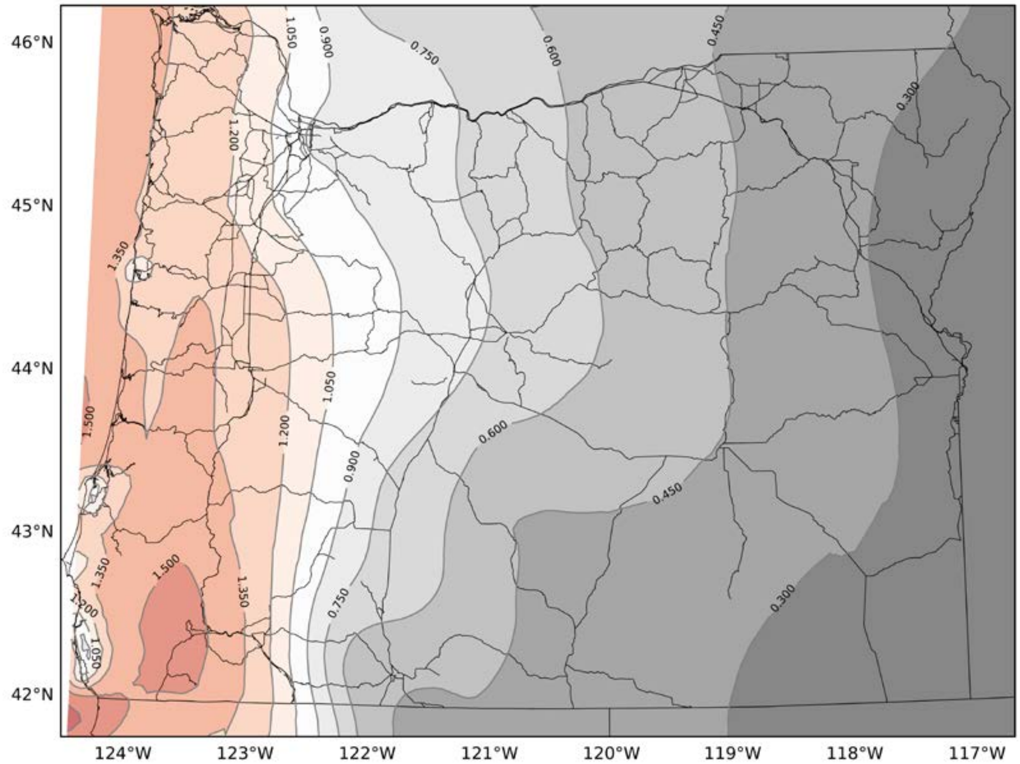

Figure D- 12: 14CSZ vs. 02PSH500 for 1.0s

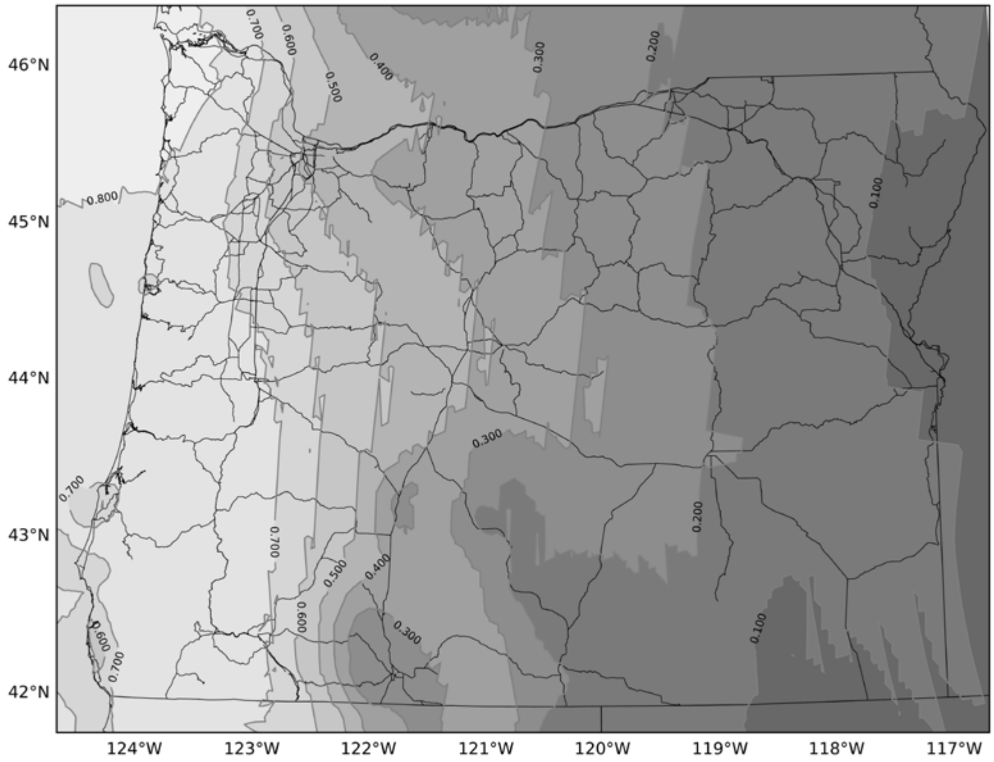

Figure D- 13: 14CSZ vs. 14PSH1000 for PGA

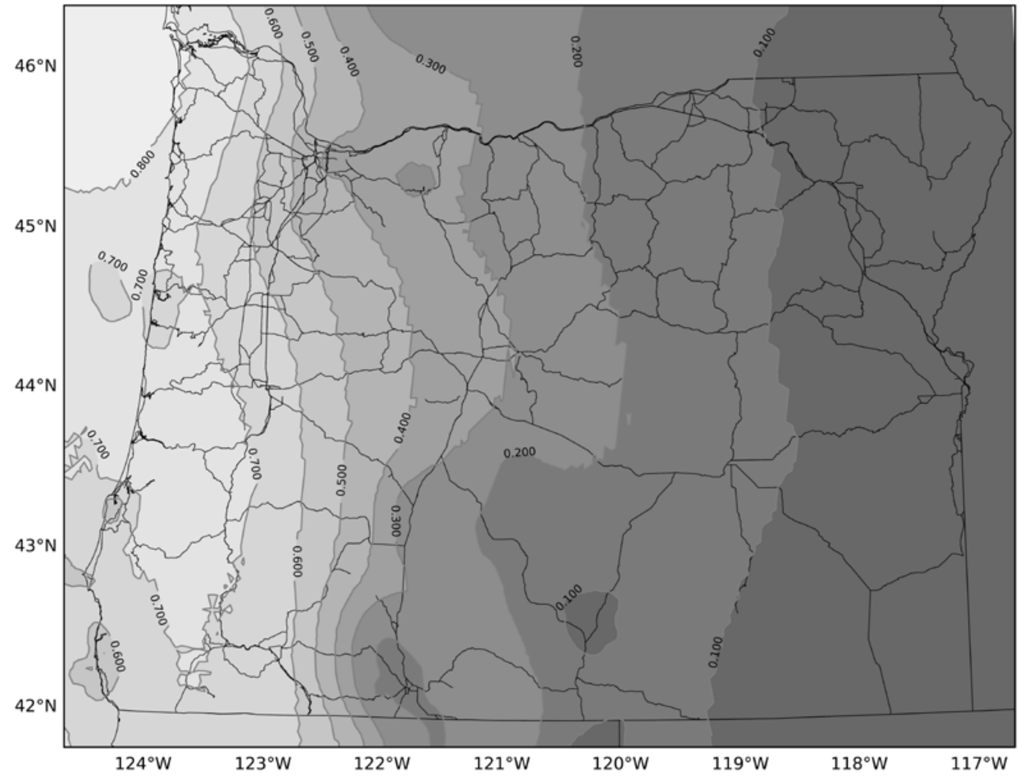

Figure D- 14: 14CSZ vs. 14PSH1000 for 0.2s

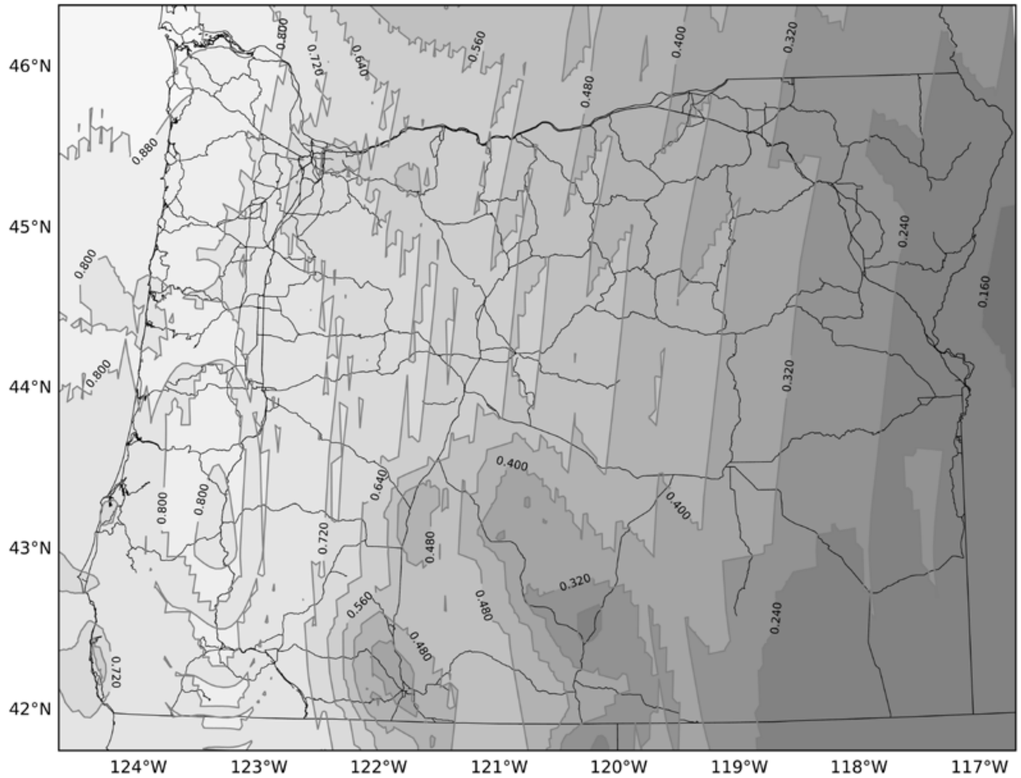

Figure D- 15: 14CSZ vs. 14PSH1000 for 1.0s

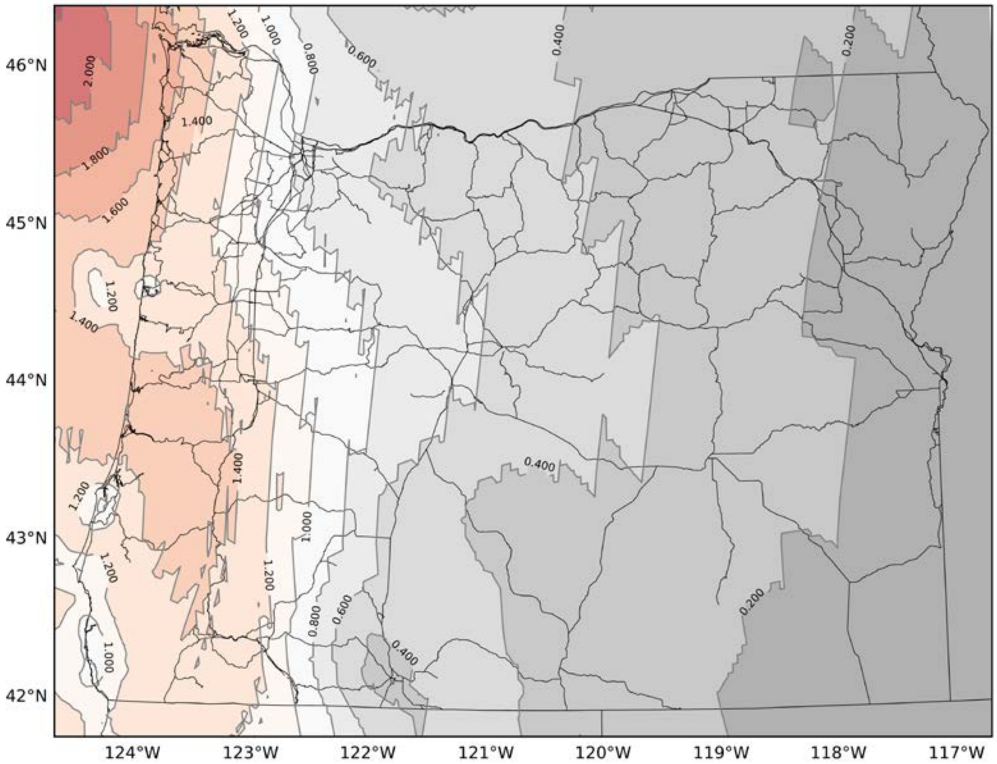

Figure D- 16: 14CSZ vs. 14PSH500 for PGA

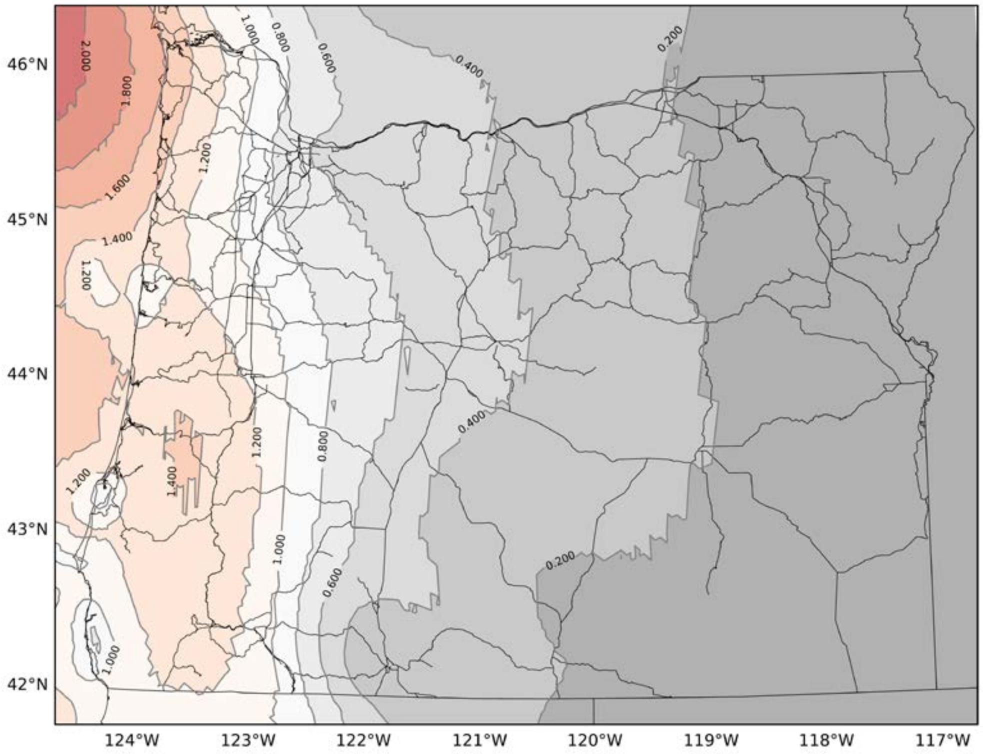

Figure D- 17: 14CSZ vs 14PSH500 for 0.2s

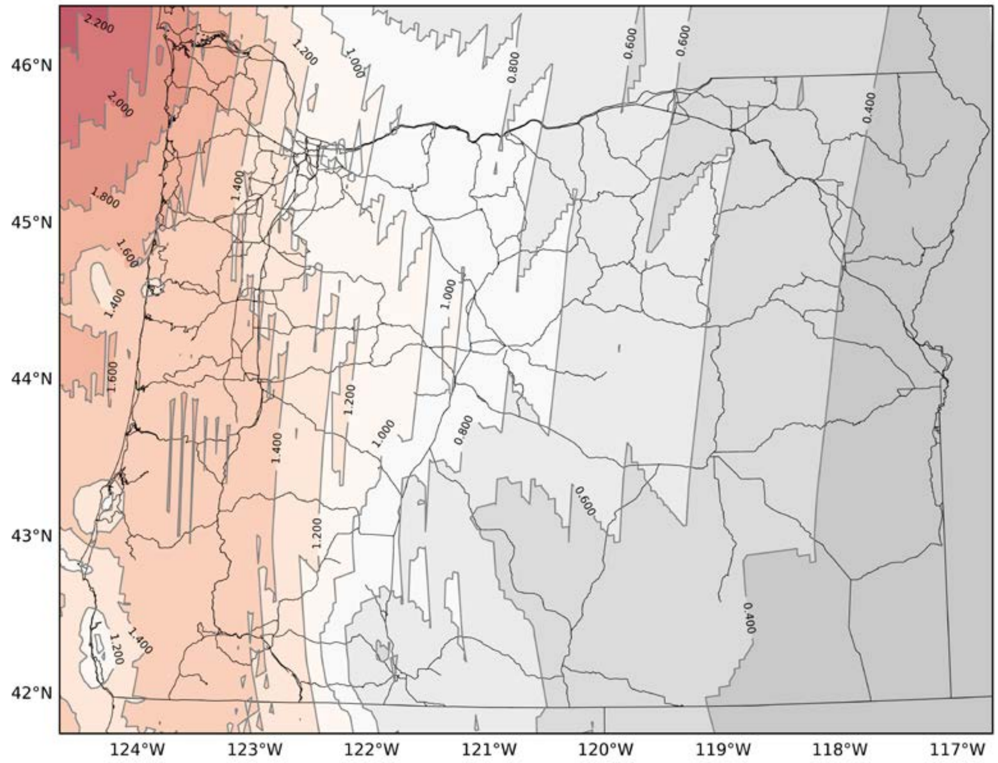

Figure D- 18: 14CSZ vs. 14PSH500 for 1.0s

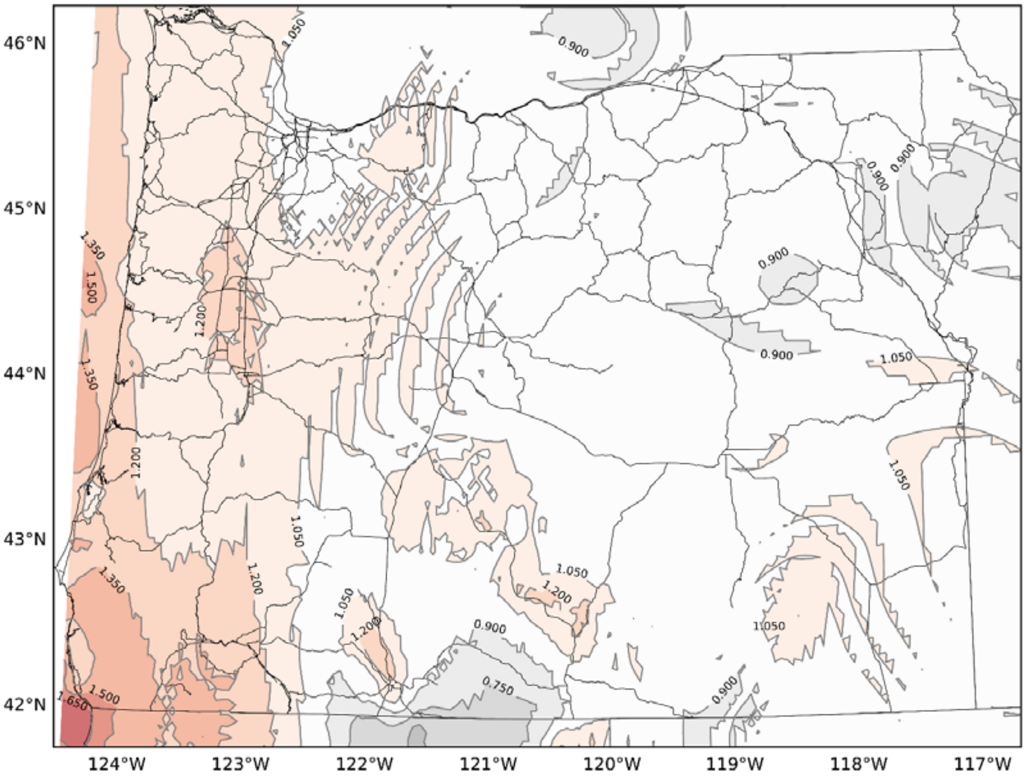

Figure D- 19: 14PSH1000 vs. 02PSH1000 for PGA

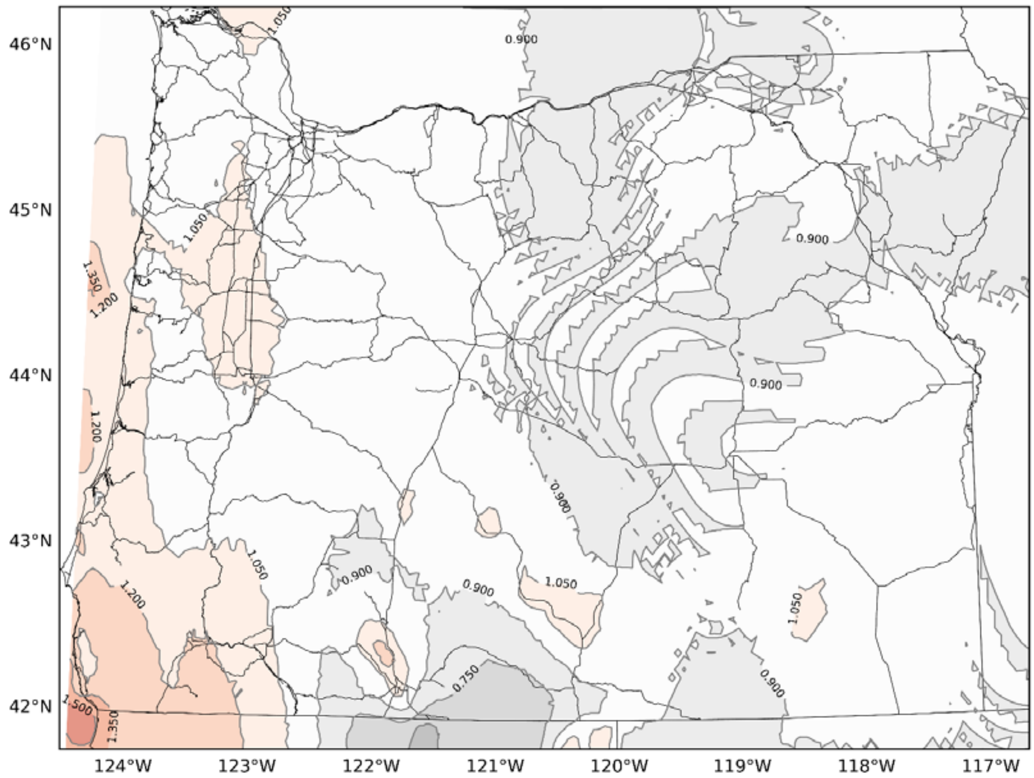

Figure D- 20: 14PSH1000 vs. 02PSH1000 for 0.2s

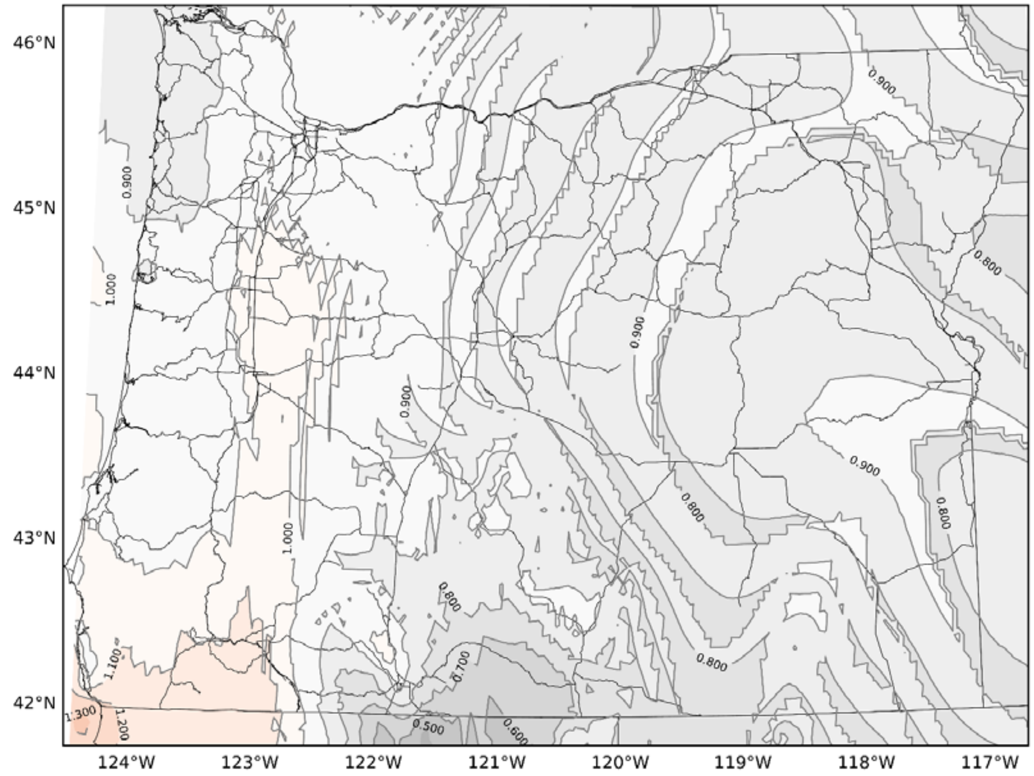

Figure D- 21: 14PSH1000 vs. 02PSH1000 for 1.0s

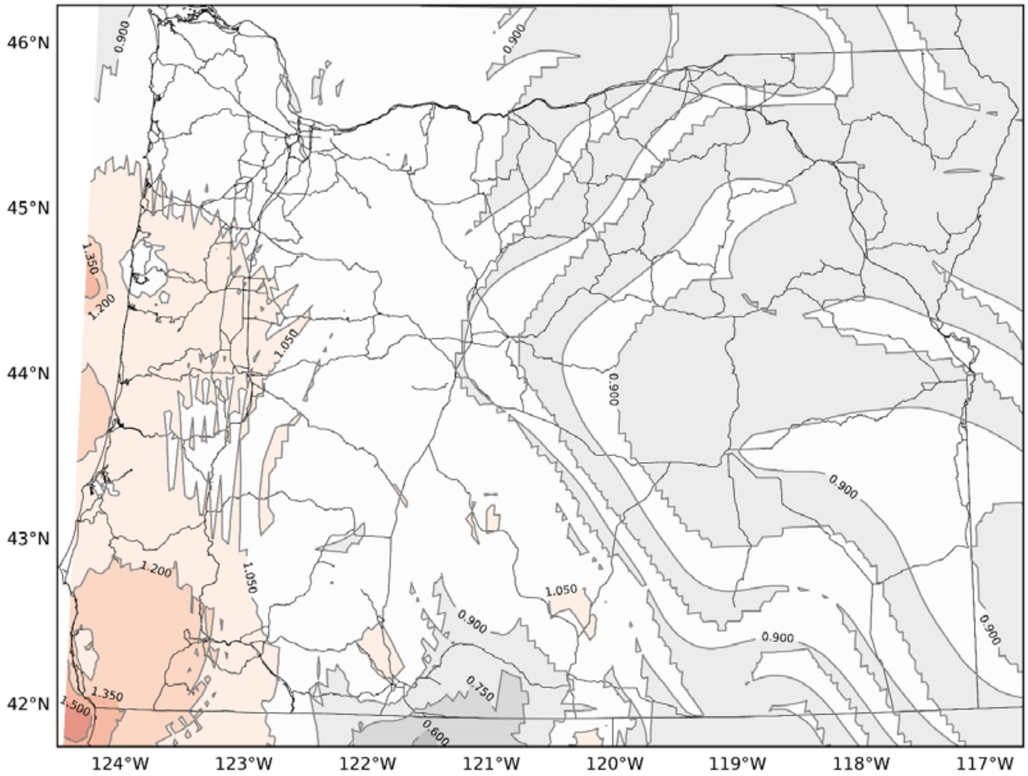

Figure D- 22: 14PSH500 vs. 02PSH500 for PGA

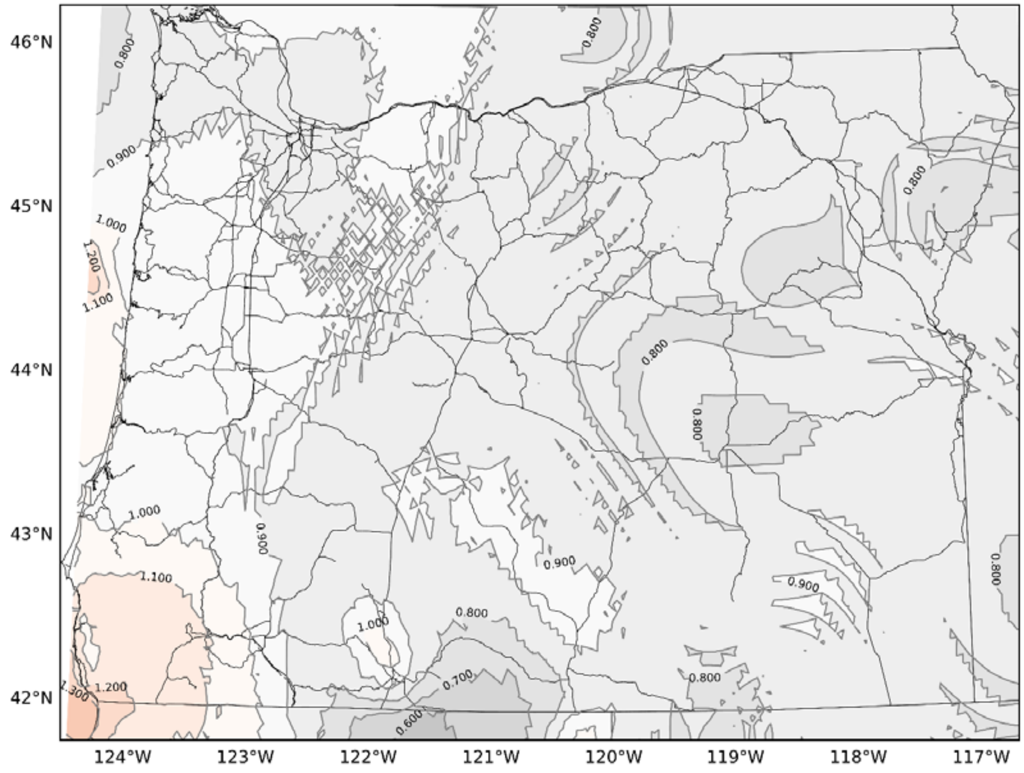

Figure D- 23: 14PSH500 vs. 02PSH500 for 0.2s

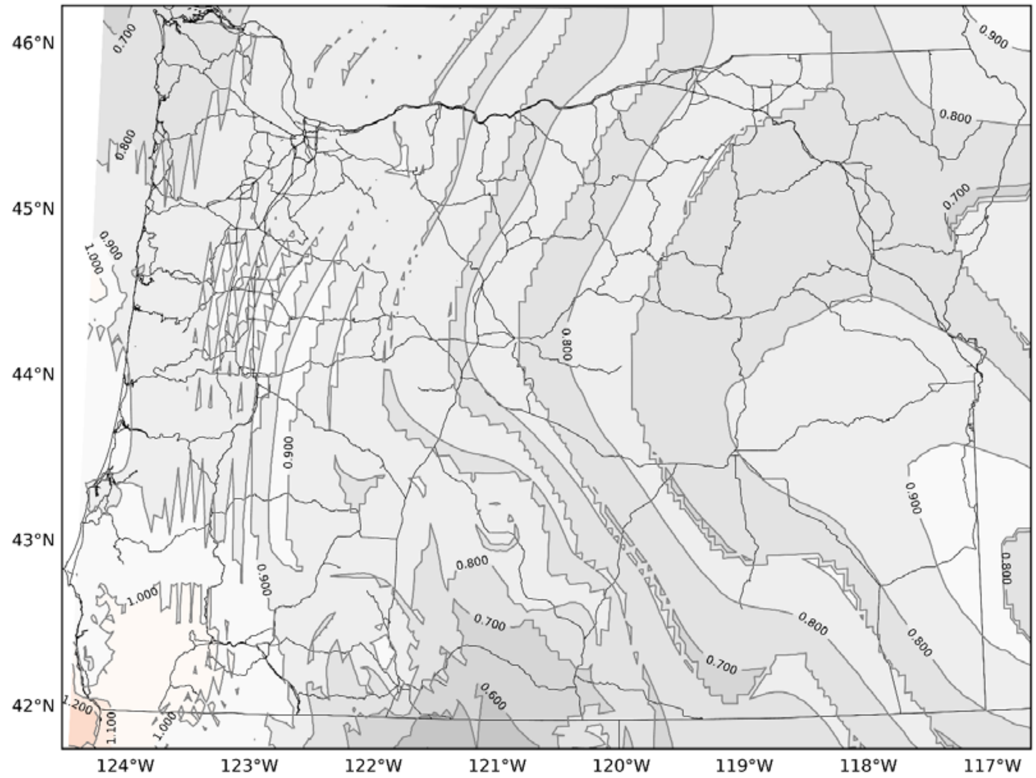

Figure D- 24: 14PSH500 vs. 02PSH500 for 1.0s

APPENDIX E

ADDITIONAL RESULTS FROM CHAPTER 4

APPENDIX E

ADDITIONAL RESULTS FROM CHAPTER 4

Table E- 1: Capitola X Shake Table Performance

Event	Motion SF	Target PGA [g]	Achieved PGA [g]	Target PGV [in/sec]	Achieved PGV [in/sec]	Target PGD [in]	Achieved PGD [in]
1	1.00	0.53	0.51	14.75	14.69	2.97	2.64
2	1.48	0.78	0.85	21.83	22.26	4.39	3.92
3	1.75	0.92	1.06	25.82	24.75	5.19	4.66

Table E- 2: Curico X Shake Table Performance

Event	Motion SF	Target PGA [g]	Achieved PGA [g]	Target PGV [in/sec]	Achieved PGV [in/sec]	Target PGD [in]	Achieved PGD [in]
1	1.57	0.65	0.77	20.01	18.70	3.73	3.25
2	1.68	0.69	0.83	21.41	20.27	4.00	3.48
3	1.74	0.72	0.86	22.17	21.07	4.14	3.62

Table E- 3: Iwaki Y Shake Table Performance

Event	Motion SF	Target PGA [g]	Achieved PGA [g]	Target PGV [in/sec]	Achieved PGV [in/sec]	Target PGD [in]	Achieved PGD [in]
1	1.77	0.67	0.75	17.71	21.00	4.26	3.39
2	1.92	0.73	0.83	19.21	23.10	4.62	3.68
3	2.04	0.78	0.91	20.41	24.14	4.91	3.84